Dissertation

Bergische Universität Wuppertal

Institut für Atmosphären- und Umweltforschung

Modeling and Diagnosis of the Stratospheric Circulation

December 14, 2021

Edward Joseph Charlesworth

The PhD thesis can be quoted as follows:

urn:nbn:de:hbz:468-20220324-121006-7
[http://nbn-resolving.de/urn/resolver.pl?urn=urn%3Anbn%3Ade%3Ahbz%3A468-20220324-121006-7]

DOI: 10.25926/1513-4h20
[https://doi.org/10.25926/1513-4h20]

The transport of chemical species in the stratosphere has major impacts on a variety of ecologically-relevant phenomena. Ozone distributions, for example, reduce incoming ultraviolet solar radiation and thereby increase the viability of life on the surface of the Earth, whereas water distributions are known to have impacts on the surface radiative balance. These (and other) chemical distributions are often interrelated, such as how water vapor provides the primary source of ozone-destroying hydrogen species in the stratosphere, whereas ozone and water vapor concentrations both play roles in the tropical tropopause radiative balance and thereby affect incoming water vapor mixing ratios. This complexity of interaction presents a challenge in the understanding and modeling of the stratosphere and the transport of chemicals within it. This dissertation presents work which is aimed towards improving both the understanding and modeling of stratospheric transport and is presented in three parts.

In the first part, passive tracer transport is used to assess the time scales of stratospheric transport in the absence of non-conserving chemical or other loss processes and in the context of climate model simulations. More particularly, transport time scale distributions are compared between two transport schemes – one Eulerian and the other Lagrangian – which are driven by the same model simulation. The results of this work show that the two transport schemes produce very different transport time scales around many key features of the stratosphere. The Lagrangian model shows slower transport in most of the stratosphere and shows evidence which suggests that it should produce stronger gradients in tracers, in comparison to the Eulerian model, in many locations where strong gradients are expected from observations for a variety of chemical species.

In the second part, the modeling experiments from the first part are extended to include water vapor transport. The results of this work show that the Lagrangian model transports much less water vapor into the stratosphere than the Eulerian transport model, particularly in the extratropical lowermost stratosphere. This region shows differences of a factor of two or more (up to five), which raises significant questions about the reliability of current model representations of water vapor in the upper-troposphere lower-stratosphere region and the radiative effects thereof. Furthermore, the water vapor distributions of both transport models were used to drive radiation calculations in two different simulations, for which differences of up to 10 Kelvin in the extratropical lowermost stratosphere were found.

The third part presents a novel quantity of observation-based constraint for stratospheric tropical upwelling. This method derives an effective upwelling velocity from ozone measurements. It is argued that the quantity can be used as a proxy for standard measurements of upwelling in a key location of the stratosphere, and results are presented derived from three ozone datasets. The three sets of effective upwelling estimates are found to vary somewhat depending on the observational methods used but largely agree in terms of the seasonal cycle of upwelling, which is also shown to be consistent with established reanalysis estimates. Furthermore, trends are calculated from the effective upwelling timeseries, again with considerable disagreement

depending on what kind of observations were used. Satellite observation-derived results show strong acceleration trends over the period 1984-2019, while radiosonde observation-derived results show no trend over the period 1998-2018.

Contents

List of Figures

List of Tables

Acknowledgements

There are a lot of people in my life without whom this thesis would not have become the work that it is. Their impact in my life hangs on every page, even though most of them have never personally touched the work. Most of all, I want to thank my brother, Al, my mother, Rita, my father, Alan, and all my mentors, Felix, Thomas, John, and Katie.

My thanks also extend to several colleagues whose thoughts and time were critical to this work's development, most of all Nicole Thomas, Patrick Jöckel, Jens-Uwe Grooß, Paul Konopka, Rolf Müller, Martin Riese, Moha Diallo, Hella Garny, and Marius Hauck. Lastly, I want to thank my dear friends, both those from Cascadia and Colorado, as well as all my friends in Germany, especially all of the Widdersdorfers. A special thanks goes out to Luca Iampieri, whose advice made the work of Chapter 5 possible.

1. Introduction

Climate change is one of the dominating problems of the twenty-first century. Its potential effects include the extinction of countless species of flora and fauna, the end of entire ecosystems, the need for mass human resettlement, and – in some wealthy nations – concerns about the quality of wine vintages. As industrialized nations show little sign of addressing the issues of greenhouse gas emissions and human-caused ecosystem damage which are the core causes of climate change, research to estimate the effects thereof are necessary.

The stratosphere is expected to be affected by and contribute to climate change in ways that are often not considered in broad-stroke summaries of the topic. For example, changes in stratospheric chemical distributions are expected to cause major radiative changes in both the stratosphere (e.g., Manabe and Wetherald, 1967) and the troposphere (e.g., Solomon, K. Rosenlof, et al., 2010). Increases in tropospheric temperatures are also expected to cause accelerations in the stratospheric circulation (Morgenstern et al., 2010; Oberländer-Hayn et al., 2016), which would consequently have have impacts on stratospheric chemical distributions, forming a feedback on tropospheric temperatures. Among the chemicals which are expected to be affected are water and ozone. Climate model simulations robustly suggest increases in both of these species (with the exception of ozone near the tropical tropopause, which is expected to decrease) (see Keeble et al. (2020) for a recent overview).

Stratospheric water vapor increases are thought to have radiative feedbacks on tropospheric temperatures (e.g., Solomon, K. Rosenlof, et al., 2010). A region which has a particularly strong control on this feedback is the extratropical lowermost stratosphere, in part due to the robust and large positive water vapor trends in the region (Banerjee et al., 2019). However, this region is also associated with wet biases in contemporary global climate models which are just as robust as the expected water vapor trends (Keeble et al., 2020). Especially considering that observations have not shown evidence of these changes, understanding the reasons for these wet biases is an important task for research (Hegglin et al., 2014).

One possible reason for these wet biases lies with model transport schemes. All transport schemes used in the climate model intercomparison projects – both modern and earlier – use Eulerian discretizations, and as a consequence are all associated with some level of numerical diffusion (Gupta, Gerber, and Lauritzen, 2020). The extratropical lowermost stratosphere is known to lie next to strong gradients in water vapor mixing ratios. Strong gradients like these are known to be particularly affected by numerical diffusion, which can cause spurious, unphysical transport across gradients, and in this case would be expected to moisten the extratropical lowermost stratosphere. The effects of numerical diffusion associated with transport schemes is

therefore of considerable interest in understanding tracer distributions in this region, as well as other areas of known strong tracer gradients in the stratosphere.

Furthermore, the relative strength of different transport pathways (deep versus shallow branches and isentropic mixing) in that region may differ between models, providing another possible cause of model tracer distribution biases. Part of the challenge in reducing the inter-model circulation strength spread is the dearth of observation-based estimates of circulation strengths. Although some methods have been applied to estimate this in the long-term mean (e.g., Fu, Hu, and Yang, 2007) or seasonal cycle (Glanville and T. Birner, 2017, e.g,), no quantitative estimates of inter-annual variability have yet been presented. Quantitative estimates of inter-annual variability of stratospheric tropical upwelling thereby have the potential to be a significant boon to understanding of the stratosphere.

The investigations described in this work address two research directions related to these two problems. The first is the effects of model transport schemes on the distribution of tracers in the stratosphere, using the EMAC climate model with two transport schemes. The first transport scheme is the standard flux-form semi-Lagrangian (FFSL) scheme of EMAC, while the second is the fully-Lagrangian transport scheme of EMAC-CLaMS. This invesigation is made of two parts, the first of which involves the application of passive tracers to calculate the stratospheric age spectrum distribution, where large schemal differences are found in transport time scales in and around critical locations of the stratosphere. This is described in Chapter 3 and is based on the published paper Charlesworth, Dugstad, et al. (2020). The main points of this chapter are:

- EMAC-CLaMS shows transport which is in general slower than EMAC-FFSL.
- Differences in transport time scales between EMAC-FFSL and EMAC-CLaMS are strongest around transport barriers.
- Very short transport time scales show the greatest differences, particularly in locations such as the southern stratospheric polar vortex and lowermost stratosphere.

The second part extends this work towards the transport of water vapor and includes the radiative impacts of water, showing very large schemal differences in water vapor in the extratropical lowermost stratosphere along with large temperature differences in the same region between coupled and uncoupled simulations. This is described in Chapter 4. The main points of this chapter are:

- EMAC-CLaMS produces water vapor distributions which are much drier than EMAC-FFSL (up to 80% less water) in the lowermost stratosphere.
- Radiative application of the EMAC-CLaMS water vapor distribution produces temperature differences of up to 10 Kelvin.

The second direction of research is estimating the variability – both seasonally and inter-annually – of tropical stratospheric upwelling using observations of ozone. This is described in Chapter 3. The main points of this chapter are:

- Introduction of an "effective" upwelling velocity derived from observations of ozone.
- The use of this effective velocity as a proxy for standard upwelling velocity anomalies at 70 hPa in the southern tropics is valid.
- The seasonal cycle of effective upwelling is similar to that of existing standard upwelling datasets.
- Two ozone datasets produce upwelling with long-term accelerating trends while a third dataset shows a near-zero long-term trend.

Finally, Chapter 6 provides some closing commentary on the work as a whole.

The author also wishes to note the following peer-reviewed publications, to which the work of this thesis contributed (the first are published while the latter two are in review or preparation):

- Plöger, F., Legras, B., Charlesworth, E., Yan, X., Diallo, M., Konopka, P., Birner, T., Tao, M., Engel, A., Riese, M.: *How robust are stratospheric age of air trends from different reanalyses?*, Atmospheric Chemistry and Physics, 19, 9, https://doi.org/10.5194/acp-19-6085-2019, 2019.
- Charlesworth, E. J., Dugstad, A., Fritsch, F., Jöckel, P., Plöger, F.: *Impact of Lagrangian transport on lower-stratospheric transport timescales in a climate model*, Atmospheric Chemistry and Physics, 20, 23, https://doi.org/10.5194/acp-20-15227-2020, 2020.
- Plöger, Diallo, M., F., Charlesworth, E., Konopka, P., Legras, B., Laube, J. C., Grooß, J., Günther, G., Engel, A., Riese, M.: *The stratospheric Brewer-Dobson circulation inferred from age of air in the ERA5 reanalysis*, Atmospheric Chemistry and Physics, https://doi.org/10.5194/acp-2020-1253, *in review.*
- Charlesworth, E. J., Diallo, M., Plöger, F., Birner, T., Jöckel, P.: *A method for estimation of upwelling anomalies from ozone observations at the base of the tropical pipe, in preparation.*

2. Background

The content of this chapter provides material that is necessary to place the new research of this dissertation in the context of prior knowledge. It begins with Section 2.1, which discusses the processes of radiation involved in the stratosphere. The contemporary theory of stratospheric transport and its development is the topic of Section 2.2. Section 2.3 describes the chemistry in which ozone and water vapor are involved as well as the passive tracers used in age of air calculations, which is a diagnostic tool used in this work. Finally, Section 2.4 lays out the expected future trends in a variety of stratospheric phenomena.

2.1. Radiation

All wind and stillness, all rain, snow, and drought, all hot, cold, and mild temperatures, all tornados, blizzards, and hurricanes, and all other characteristics of weather and climate begin with the interaction of radiation with the atmosphere and with the Earth's surface. This interaction causes heating and cooling over the atmosphere, thereby forming uneven distributions of energy which give rise to the flow of the atmosphere as a result[1]. The radiation which is relevant to the earth system's energy balance may be conceptually divided between terrestrial and solar radiation. Terrestrial radiation originates from the emission of radiation by the molecules of the atmosphere, oceans, and everything forming the surface of the earth (rocks, soil, sand, flora, and even fauna). These photons might be emitted towards the earth's surface (if emitted by the atmosphere) or towards space, and in both cases are often absorbed by the atmosphere before reaching either destination. Meanwhile solar radiation is emitted by the sun and reaches the Earth after either an 8.3 minute journey through space or a slightly (1.3 second) longer trip after a quick detour to the moon, from which it may be reflected onto the earth. On its path through the atmosphere, solar photons might be reflected, scattered[2], or absorbed by the atmosphere or the Earth's surface. The difference between the global-mean, long-term (e.g., over the course of

[1] Geothermal processes such as volcanoes or hot springs may also induce direct changes in the atmospheric energy balance, producing uneven energy distributions. However, these changes are local, while the effects of solar and terrestrial radiation impact the entire global atmosphere.

[2] The reader may have the fortune to see blue skies when looking outside at the moment. The reason why this color is often seen during the day is the effect of the selective scattering of solar photons by the atmosphere. More precisely, short-wavelength photons are more likely to be scattered than long-wavelength photons, such that blue and violet photons are preferentially scattered to photons associated with other colors. Human eyes are more sensitive to blue light, so the sky appears predominately blue. This process is called Rayleigh scattering.

a year) total energy of absorbed solar radiation and escaping (or outgoing) terrestrial radiation is nearly in balance. The small differences between these two values might have many causes, but the effect of climate change is the most interesting of these causes.

From an interplanetary prespective, both the sun and earth are, to a rough and non-robust approximation, black bodies. The concept of black bodies is an idealization of the interaction of radiation with physical objects which states that black bodies are objects which absorb all incoming radiation. The emission of radiation by black bodies follows Planck's law, which relates the quantity of emission of radiation at a particular wavelength to the temperature of the emitting body. Under this law, warmer bodies emit more radiation than colder bodies and warmer bodies emit a greater portion of their radiation at shorter wavelengths than colder bodies do. As black bodies, the sun emits at a temperature of approximately 5800 K while the Earth emits at a temperature of approximately 250 K. This difference in the emission temperatures of the two bodies means that the emission spectra of the two bodies are well-separated, allowing the separation of their radiation into terrestrial (longwave) and solar (shortwave), with only a very small amount of overlap between the two distributions in terms of total emitted energy.

Although the black body assumption is, under certain circumstances, approximately true, only highly idealized contexts allow the application of Planck's law to models (numerical or conceptual) of earth's climate or weather. This is because the black body model neglects the effects of photon reflection and scattering and assumes that all incoming radiation is treated evenly (i.e. entirely absorbed) by the atmosphere and Earth's surface. The processes of reflection, scattering, and absorption are of course much more nuanced and complex than this model. Scattering, for example, is often performed by aerosols in the atmosphere (in addition to the scatter performed by gaseous molecules), while the reflection of photons is an important process with regards to clouds and the Earth's surface, which can have a wide range of albedo – reflectiveness – depending on the surface material (e.g., sea ice is highly reflective, whereas sea water is much less reflective).

The process of absorption is also not consistent over spectral wavelength and in many cases depends strongly on the composition of the intercepting molecules. The most discussed of these chemicals are greenhouse gases (GHG's), which are strongly absorbent in the longwave spectrum. These gases include water, chlorofluorocarbons (CFC's), and – most notoriously – carbon dioxide and methane, among others. GHG's can intercept outgoing longwave photons before they exit the atmosphere, and then emit the energy (also as a longwave photon) in a random direction. Explained very plainly, one could say that GHG's give intercepted photons a chance to change their direction, such that outgoing photons may return to Earth. Owing to their high absorptivity in the longwave, GHG's are particularly potent in this behavior, and maintain surface temperatures roughly 40 K above those that would exist in their absence (e.g., under a black body-like atmosphere).

GHG's, in a lesser known effect, also cool the upper atmosphere. From the standpoint of energy conservation, this must be the case, as GHG's only change the distri-

bution of energy within the atmosphere, not the total amount. The plain explanation of this behavior is also similar: longwave photons aiming towards the Earth may be intercepted by a GHG molecule and given a chance of exiting the atmosphere again. The precise altitudes which divide these two regions (where the effect of GHG's is cooling/warming) are dependent on the vertical distribution of longwave emission.

Aside from GHG's, the most important chemical with regards to the distribution of temperature in the atmosphere is ozone[3]. Ozone's most important radiative effect is the absorption of solar radiation, and, in particular, that of ultraviolet radiation. Ultraviolet radiation is defined as radiation in the wavelengths between 10 and 400 nm, and can be harmful to the health of fauna, by, for example, causing skin cancer, or more tamely by souring a day at the beach via sunburn. Ozone is much more efficient in this role compared to other atmospheric chemical species, making ozone a critical chemical for the viability of life on earth. Ozone is also created by the absorption of ultraviolet radiation by diatomic oxygen (see Section 2.3.2.1 for details), such that ozone is abundant in the higher atmosphere, above which little material exists to absorb ultraviolet radiation. The region where ozone is most abundant is called the ozone layer, and this region is contained within the stratosphere. The absorption of UV radiation within this region (by ozone or diatomic oxygen) also acts as a local source of warming, such that temperatures in the stratosphere are much warmer than would be expected in an atmosphere without any oxygen[4].

Moreso, the vertical structure of the atmospheric temperature distribution is qualitatively different than would be expected without any oxygen. In particular, temperatures in an atmosphere without oxygen would be expected to monotonically decrease with increasing altitude[5], whereas temperatures increase with altitude within the stratosphere[6] (see Figure 2.1). This structure also motivates the clear definition of the tropopause – the boundary between the troposphere and stratosphere – as the location where temperatures are coldest[7].

2.2. Stratospheric Transport

2.2.1. Early Theory Development

The first conception of a global poleward-propagating stratospheric circulation was suggested in the middle of the 20th century by Gordon Dobson and Alan Brewer, both on the basis of observations of stratospheric chemical distributions. Dobson, Harrison, and Lindemann (1926), on the basis of total column ozone measurements,

[3] Ozone is also a GHG, but for the purposes of this work the greenhouse effects of ozone are not relevant in comparison to its other radiative effects.

[4] An atmosphere without oxygen, of course, would also mean an atmosphere without ozone.

[5] With the exception of small-scale, transient features such as near-surface inversion layers.

[6] In an atmosphere without oxygen, temperatures would increase with altitude at extremely high altitudes, where the absorption of solar radiation by other species maintains high temperatures.

[7] Other definitions of the tropopause do exist, and are often more consistent and effective, but this definition is the simplest, and is sufficient for the present work.

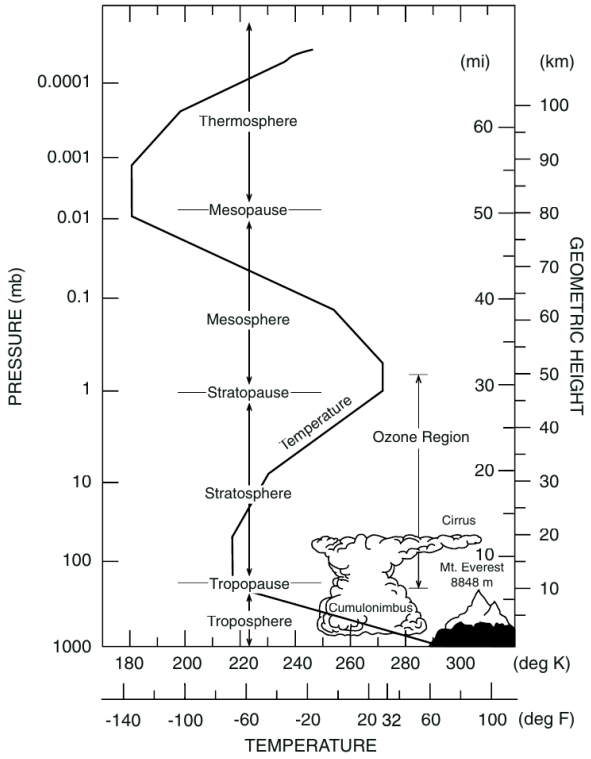

Figure 2.1.: Approximate vertical temperature profile of the atmosphere in midlatitudes from the surface to beyond the Kármán line. From Brasseur and Solomon (2005) (their Figure 3.1).

reasoned that ozone must be transported out of the tropics to high latitudes by a global meridional circulation. This conclusion was based on their assumption that ozone was created by sunlight, therefore having greater production near the equator, and their results showing that total column ozone is higher in high latitudes than the tropics. However, the authors also noted their concern that such a circulation would violate the conservation of angular momentum.

Brewer (1949) – informed by the work of Dobson, Harrison, and Lindemann (1926) – used vertically-resolved column water vapor and helium measurements to infer not only the existence of a global meridional stratospheric circulation, but that the circulation must begin at the tropical tropopause, as depicted in Figure 2.2. This latter inference was based on the low water vapor mixing ratios Brewer had measured, which were consistent with a saturation water vapor mixing ratio of temperatures equivalent to the tropical tropopause temperature.

Although both Dobson and Brewer correctly inferred the existence of the stratospheric circulation, neither provided a theoretical explanation for the phenomenon. Not unaware of this open topic, Alan Brewer concluded his paper with “The dynamic consequences of the circulation have not been discussed. There are considerable difficulties in this respect." Despite the concerns of Dobson, Harrison, and Lindemann

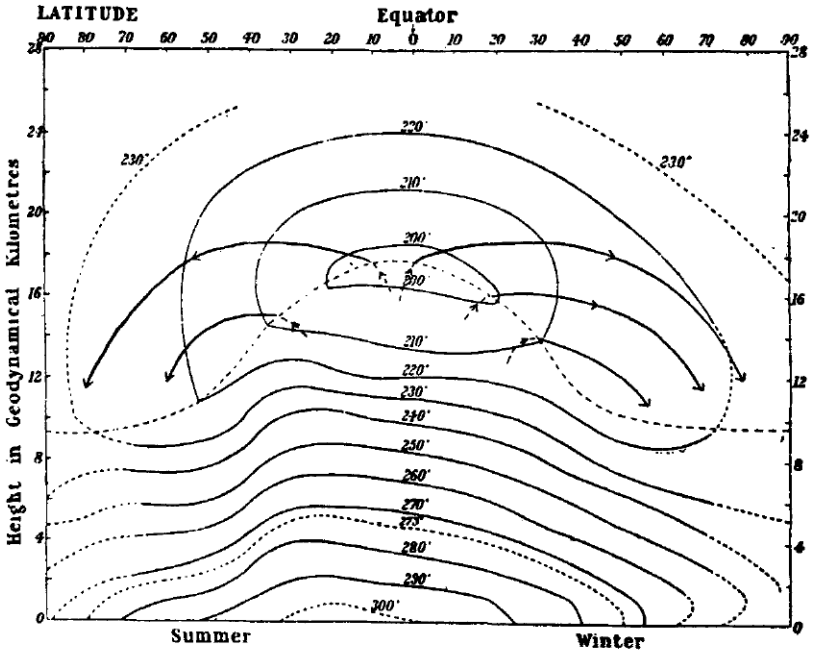

FIG. 5. A supply of dry air is maintained by a slow mean circulation from the equatorial tropopause.

Figure 2.2.: An idealized diagram of the stratospheric circulation as conceived from Brewer (1949).

(1926) and Brewer (1949), the notion of a global stratospheric circulation was soldified by Dobson and Massey (1956), who unified the use of ozone and water vapor measurments in their investigation. Murgatroyd and Singleton (1961) later used calculations of diabatic heating rates and parcel trajectories based on those calculations to provide a broader description of the stratospheric circulation (as well as the mesospheric meridional circulation). However, these calculations as well as later ones (Vincent, 1968) showed conflicts between Eulerian-mean and mass transport calculations. For a more thorough review of these topics, Butchart (2014) is an excellent source.

2.2.2. The Residual Circulation

This conflict was not resolved until the pioneering theoretical work of (D. G. Andrews and McIntyre, 1976; D. G. Andrews and M. E. Mcintyre, 1978a; D. G. Andrews and M. E. Mcintyre, 1978b; D. Andrews and M. Mcintyre, 1978) who introduced both a generalized Lagrangian mean and their novel transformed Eulerian-mean (TEM), which was applied by Dunkerton (1978) to show a comprehensive description of the stratospheric circulation.

$$\overline{v}^* = \overline{v} - \rho_0^{-1} \left(\rho_0 \overline{\theta}_z^{-1} \overline{v'\theta'} \right)_z \tag{2.1}$$

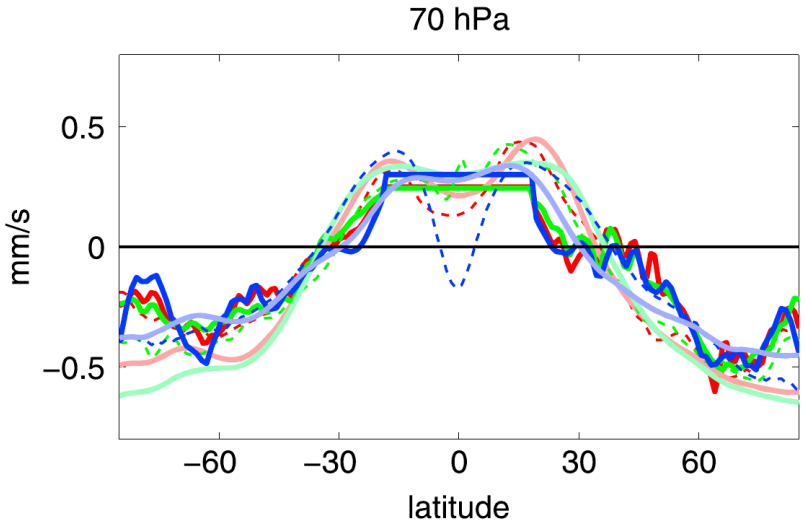

Figure 2.3.: Upwelling velocities computed from three frameworks (mass balance in solid lines, standard residual Equations 2.1 and 2.2 in dashed lines, and thermodynamic in pale solid lines) and three reanalysis datasets (ERA-interm in red, JRA55 in green, and MERRA in blue) meridionally-resolved at 70 hPa. From Abalos, Legras, Ploeger, et al. (2015) (their Figure 3).

$$\overline{w}^* = \overline{w} + (a\cos(\phi))^{-1}\left(\cos(\phi)\overline{\theta}_z^{-1}\overline{v'\theta'}\right)_\phi, \tag{2.2}$$

where $\overline{f}$ denotes the zonal mean of f, f' denotes the zonal anomaly of f, f^* denotes the "residual" of f, v and w are the meridional and vertical wind velocities, θ is potential temperature, a is the radius of the Earth, ϕ is latitude, and ρ_0 is basic density ($\rho_o = p_s \exp -z/H$ where p_s is surface pressure, z is altitude, and H is scale height, typically 7 kilometers). This perspective is called the *residual circulation*. The core process measured by these velocities is the eddy heat flux. That is, the flux of heat caused by stratospheric wave activity (of, for example, gravity or Rossby waves).

In addition to the standard definition given in Equations 2.1 and 2.2, some other frameworks are commonly used, namely that based on momentum balance and that based on the thermodynamic balance. Although the phenomenon described by these prespectives is in principle the same, the results are not necessarily in agreement. Abalos, Legras, Ploeger, et al. (2015) compared the velocities found by these frameworks, showing notable quantitative and some qualitative differences. One result of their work is shown in Figure 2.3, where upwelling from three reanalyses (MERRA, JRA55, ERAi) is shown as defined by the residual circulation, the thermodynamic balance, and momentum, at 70 hPa. These quantities all generally agree on the qualitative structure of upwelling with respect to latitude; upwelling occurs in the tropics and downwelling in the extratropics. The only exception to this is the residual circulation interpretation of MERRA results, where downwelling is found in a small

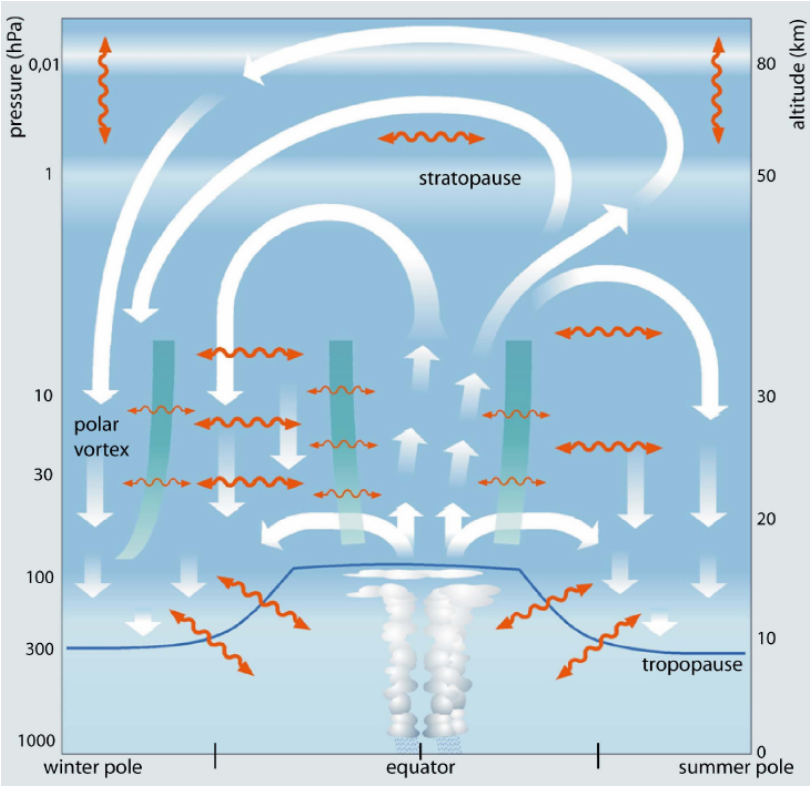

Figure 2.4.: A diagram of the circulation of the middle and upper atmosphere. White lines show advective transport, red lines show mixing, vertical blue-green barriers show locations of transport barriers, and the thin blue line shows the location of the tropopause. From Bönisch, Engel, Th. Birner, et al. (2011) (their Figure 1).

region around the equator. Another notable difference is the level of variability with latitude found in the different perspectives. In particular, the momentum prespective shows the greatest variability, while the thermodynamic balance shows rather smooth changes with latitude.

2.2.3. A Comprehensive Circulation

A more modern picture of the stratospheric circulation has been developed since the work of Dunkerton (1978). One example of this is shown in Figure 2.4, which is from Bönisch, Engel, Th. Birner, et al. (2011). This diagram shows the single-cell, summer-to-winter meridional circulation of the mesosphere (first found by Murgatroyd and Singleton (1961)), as well as the tropical upwelling suggested by Brewer (1949). In contrast to the suggestions of Dunkerton (1978) and preceding works, which suggested only a single flow from the tropics to higher latitudes, this depiction separates the circulation into shallow and deep branches, as suggested by Plumb (2002) and further

researched by T. Birner and Bönisch (2011). The shallow branch is characterized by air flowing poleward from the tropics directly after passing through the tropical tropopause, while the deep branch is characterized by air moving poleward only after reaching deeper into the stratosphere. The air which moves through the deeper branch first passes through the so-called tropical pipe, a region where air is relatively isolated from interaction with higher latitudes, which was first described by Plumb (1996). The shallow and deep branches are characterized by a large difference in transport time scales, with movement through the shallow branch being on the scale of months while movement through the deep branch is on the scale of years.

Furthermore, the role of mixing is acknowledged in this diagram. This mixing is primarily horizontal, but in contrast to Figure 2.4, this mixing has been found to chiefly happened along isentropes (Plumb, 2007), not pressure, and is related to Rossby wave activity. Mixing in the stratosphere is often referred to as "eddy mixing". Mixing was also found to be strongest in the so-called surf zones (M. Mcintyre and T. Palmer, 1983), the midlatitude regions outside of the edges of the tropical pipe. However, one of the most important areas for mixing is around transport barriers, where the one-way advection of air is relatively weak and mixing provides the dominant source of direct transport. Whether this mixing is a significant source of transport compared to advection around the transport barriers depends on both the tracer considered and the transport barrier. Not shown in this diagram is the importance of the subtropical jets as significant transport barriers.

2.2.4. Stratospheric Polar Vortices

The stratospheric polar vortices develop in the middle stratosphere (roughly between 400 and 600 K) over the polar regions each winter. These features are characterized by cold temperatures and anti-cyclonic winds. The southern polar vortex is colder than the northern polar vortex, due to stronger wave dissipation within the northern polar vortex, which is an effect of the greater amount of land surface in the northern hemisphere compared to the southern. These waves decelerate the circumpolar westerly flow when they break. Both polar vortices eventually dissipate in summer and are known to also occasionally break up during winter, under events known as sudden stratospheric warmings (Baldwin et al., 2021).

Figure 2.5 shows the course of such an event, with the polar vortex highlighted by potential vorticity. On February 1st, the vortex was over the polar region, somewhat offset towards the Atlantic Ocean. Seven days later, the vortex had elongated substantially and showed a relatively thin section over the north pole, foreshadowing the split to come. Two days after that, the polar vortex was nearly separated, with one large section over North America and another smaller section over Siberia, and on the day after that the sections were no longer connected.

These events happen much more often in the northern hemisphere (on average, once every two years) than in the southern hemisphere (where such events have only been observed twice, in 2002 and 2019). This difference means that the northern polar vortex is – over the long term – more dynamically variable than the southern

polar vortex.

2.3. Chemicals and Tracers

2.3.1. Water Vapor

Stratospheric water vapor has both *ex* and *in situ* origins. (Stratospheric water vapor originates both without and within the stratosphere.) The ex situ origin of stratospheric water vapor is primarily the passage of air upward through the tropical tropopause, outward from which the water vapor disperses into the stratosphere. As it passes through the tropical tropopause, air cools and the contained water vapor in it is reduced through "freeze-drying", a process suggested as early as Brewer (1949). The temperature of the tropical tropopause is thereby a first-order process in setting the stratospheric-entry mixing ratio value of water vapor. This phenomenon was more recently explored by the work of (Randel, F. Wu, Oltmans, et al., 2004; Randel, F. Wu, Vömel, et al., 2006).

The *in situ* origin of stratospheric water vapor is mainly the oxidization of methane (Brasseur and Solomon, 2005), which occurs through a number of reactions.

$$c_2: \quad CH_4 + OH \longrightarrow CH_3 + H_2O \tag{2.3}$$

$$c_{1a}: \quad CH_4 + O(^1D) \longrightarrow CH_3 + OH \tag{2.4}$$

$$c_{1b}: \quad CH_4 + O(^1D) \longrightarrow CH_2O + H_2 \tag{2.5}$$

$$c_{1c}: \quad CH_4 + O(^1D) \longrightarrow CH_3O \text{ (or } CH_2OH) + H \tag{2.6}$$

$$d_5: \quad CH_4 + Cl \longrightarrow CH_3 + HCl \tag{2.7}$$

Reaction 2.3 is the mechanism by which methane is oxidized to water in the stratosphere, providing a steady *in situ* source of water vapor. Due to this process, deeper stratospheric air generally has higher water vapor mixing ratios than air which is closer to the tropical tropopause.

This is shown in Figure 2.6. The water distribution in this figure also shows clearly the effect of the tropical pipe, wherein relatively isolated air from the tropical lower stratosphere rises and maintains comparatively low water vapor mixing ratios. The distribution in this figure also shows a relatively dry region around 100 hPa at the south pole, which is associated with the southern stratospheric polar vortex. Within this region, it is possible for temperatures to drop low enough during winter such that the saturation mixing ratio of water vapor reaches below the water vapor mixing ratios of incoming air, reducing water vapor content in another example of "freeze-drying".

One well-established feature of the stratospheric water vapor distribution is the so-called "tape-recorder" signal (Mote et al., 1996). This signal is seasonal, and is thereby not present in the climatological-mean water vapor distribution shown in Figure 2.6. However, the signal is present in sub-annual distributions. It is characterized by alternating wet and dry anomalies which propagate upwards through the tropical stratosphere (see Figure 2.7). This feature is caused by the seasonal cycle in tropical

tropopause temperatures. More precisely, the tropical tropopause is warmer during boreal summer and colder during boreal winter, causing relatively high and low entry water vapor mixing ratios, respectively. These signals slowly propagate vertically through the tropical pipe, remaining relatively isolated but eventually dispersing at high levels as they are mixed with the surrounding air.

One region wherein water vapor is of particularly high importance is the extratropical lowermost stratosphere (LMS). The LMS water balance is not quite so simple as that of the deeper stratosphere; tropopause-overshooting convection, isentropic mixing across the subtropical jets, and transport from the deeper stratosphere are all potential sources. Partially due to this challenge, the budget of water vapor in the LMS is poorly understood (Dessler et al., 2013). Likewise, models have their strongest biases in water vapor in this region (Keeble et al., 2020). It is also of some concern that LMS water vapor is known to have strong effects on the stratospheric radiative budget and suspected to have other effects on the surface radiative budget (Riese et al., 2012; Banerjee et al., 2019).

2.3.2. Ozone

2.3.2.1. Chapman Chemistry

The core of the modern model of stratospheric ozone chemistry was proposed by Sydney Chapman in 1930 (Chapman, 1930). In this model, only oxygen species are involved in the creation and destruction of ozone. Although this model is not complete (see later text for details), the model forms a basis for the more comprehensive modern model of stratospheric ozone chemistry. The relevant reactions of the Chapman chemistry scheme[8] are shown below.

$$k_2: \quad O_2 + O + M \longrightarrow O_3 + M \tag{2.8}$$
$$J_2: \quad O_2 + h\nu \ (\lambda < 242 \text{ nm}) \longrightarrow 2O \tag{2.9}$$
$$J_2^*: \quad O_2 + h\nu \ (\lambda < 175 \text{ nm}) \longrightarrow O + O^* \tag{2.10}$$
$$J_3: \quad O_3 + h\nu \ (\lambda < 1180 \text{ nm}) \longrightarrow O_2 + O \tag{2.11}$$
$$J_3^*: \quad O_3 + h\nu \ (\lambda < 441 \text{ nm}) \longrightarrow O_2 + O^* \tag{2.12}$$
$$k_4: \quad O^* + M \longrightarrow O + M \tag{2.13}$$
$$k_1: \quad O + O + M \longrightarrow O_2 + M \tag{2.14}$$
$$k_3: \quad O_3 + O \longrightarrow 2O_2 \tag{2.15}$$
$$k_4: \quad O + O^* \longrightarrow O_2 \tag{2.16}$$
$$k_5: \quad O^* + O_3 \longrightarrow 2O_2 \tag{2.17}$$

Reaction rate coefficients (k_2, for example) for the above reactions is provided by the Jet Propulsion Laboratory in Burkholder et al. (1993), where estimations are given

[8] The reaction rate coefficient labels are those of Brasseur and Solomon (2005), which provides an excellent discussion of stratospheric ozone chemistry.

based on a thorough review of experimental literature. Two of the species involved in the above reactions are single oxygen in ground (O) and excited (O^*) states. This description of excited oxygen neglects to differentiate the forms of excited-state single oxygen, that of $O(^1D)$ and $O(^3P)$. Although these different forms are relevant at high alitudes, they are neglected here for brevity of discussion. Likewise, diatomic oxygen has two excited forms, but this fact is also only relevant at altitudes higher than those for which ozone chemistry is involved in this work.

Transformations of ozone to single oxygen and vice-versa occur in several of the above reactions. Many of these reactions are very rapid, causing cycling between singlet and triplet (ozone) oxygen which is orders of magnitude faster than exchanges from either singlet or triplet oxygen. This wide range of time scales generates substantial problems for the application of numerical schemes used to calculating these reactions. This complication can be surmounted, however, by the assignment of the odd-oxygen chemical family. This family consists of all singlet and triplet oxygen species, and due to the rapid exchange between these species, the calculation of the odd-oxygen family composition among its particular members becomes a steady-state chemical problem, which is then relatively simple and computationally-inexpensive to solve. The problem of calculating changes in ozone mixing ratios therefore becomes a problem of calculating changes between odd-oxygen and any other oxygen species.

The photolysis of diatomic oxygen (Reactions 2.9 and 2.10) is the only known process through which odd-oxygen is created in the stratosphere (this topic is discussed in Appendix Chapter A). However, the Chapman system has several reactions which are sinks of odd-oxygen, specifically Reactions 2.14, 2.15, 2.16, and 2.17. In all these cases, diatomic oxygen is created from the consumed odd-oxygen species. Without the activity of any other chemical species, this system has been calculated to maintain ozone at mixing ratios roughly twice as strong as are observed, pointing to the incompleteness of destruction processes in the system.

2.3.2.2. Other Destruction

The missing destruction reactions involve primarily nitrogen, hydrogen, and chlorine species. These chemicals are all involved in catalytic odd-oxygen destruction cycles. For example, the nitrogen species involved are grouped into another chemical family made up of NO and NO_2. Each of these species reacts with odd-oxygen species to form their nitrogen family counterpart and diatomic oxygen. In this process, the odd-oxygen family members are destroyed while the nitrogen family members are partitioned. Similar processes also occur for hydrogen and chlorine species. Of these three, the nitrogen family catalytic destruction cycle accounts for the greatest amount of odd-oxygen destruction.

Another important aspect of the catalytic destruction cycles is the inverse temperature dependence of the reaction rate coefficients. That is, the reaction rates coefficients of the relevant reactions are smaller with colder temperatures and larger with warmer temperatures. Thereby, reductions in temperatures in the stratosphere cause decreases in local ozone destruction rates, and as a consequence ozone concentrations

increase (in absence of other factors), which has a warming effect. Similarly, increases in temperature reduce ozone concentrations. This inverse temperature dependence means that any temperature forcing is dampended by the chemistry of ozone. However, this phenomenon is only relevant in locations where the chemical destruction of odd-oxygen is a relevant part of the odd-oxygen balance (see Section 2.3.2.3).

2.3.2.3. Effect of Transport

The odd-oxygen continuity equation, in the transformed Eulerian mean perspective on pressure coordinates, is given by

$$\partial_t \chi = S + S_{\mathrm{TROP}} - L - \overline{\omega}^* \partial_p \chi - \overline{v}^* \partial_\phi \chi + M, \tag{2.18}$$

where χ is the mixing ratio of odd-oxygen, S is the photolytic production rate of odd-oxygen (see Appendix A) due to Reactions 2.9 and 2.10, S_{TROP} is the production rate of odd-oxygen due to all other reactions (i.e. tropospheric-like reactions, which are not shown in this work), L is the chemical destruction rate of odd-oxygen, $\overline{\omega}^*$ and $\overline{v}^*$ are the vertical and horizontal residual circulation velocities (see Equations 2.1 and 2.2) respectively, ϕ is latitude, and M describes the total effect of mixing (i.e. non-advective transport). This effect can be quantified from eddy fluctuation terms (deviations from zonal means) as in (Abalos, Randel, Kinnison, and Serrano, 2013). This particular formulation of the odd-oxygen continuity equation splits the total chemical source of odd-oxygen into destruction, photochemical production, and non-photochemical production. The reason for the use of this formulation is the importance of these differences in the work of Chapter 5.

The effect of transport on the stratospheric ozone distribution is of considerable importance. As mentioned earlier, the effect of horizontal transport was one reason why the existence of the stratospheric circulation was first hypothesized (Dobson, Harrison, and Lindemann, 1926). The vertical transport of ozone is also relevant for the distribution of ozone, in particular for the tropical lower stratosphere where the upwelling of ozone-sparse air maintains ozone distributions an order of magnitude below the concentrations that would be expected from purely chemical interaction. Related to this, the rates of chemical odd-oxygen destruction are much weaker than the rates of odd-oxygen removal via transport in this region. This topic was discussed by Garcia and Solomon (1985). One example of their results is shown in Figure 2.8, which suggests that the region where chemical destruction rates are weaker than the removal of odd oxygen by transport in the tropics extends to about 27 km. This figure also shows that the balance of odd oxygen in the high latitude winter hemisphere is completely controlled by dynamics, which is due to the weakness of chemistry caused by the absence of sunlight. However, it should be noted that these results are based on model data and – to the knowledge of the author – this topic has not been revisited since then, so a recreation of these results with a modern model may show substantial devations from the original work.

Abalos, Randel, and Serrano (2012) found strong correlations of ozone tendencies from observations and upwelling from reanalyses within the tropics (see Figure 2.9)

and interpreted these results as suggesting that upwelling plays a strong role in the ozone balance of the tropical lower stratosphere. Abalos, Randel, Kinnison, and Serrano (2013) built on this study and found that ozone was mostly associated with vertical advection (see Figure 2.10), in comparison to other transport terms, above about 80 hPa, by using model results, which was later supported by the work of Abalos, Ploeger, et al. (2013). Furthermore, Stolarski et al. (2014) also showed that the effects of mixing on ozone are even weaker in the southern hemisphere, in comparison to the northern hemisphere. These studies all suggest that the the ozone budget in the southern tropics above 80 hPa is largely controlled by upwelling, in comparison to any other transport terms. Meanwhile below 80 hPa, in-mixing of extratropical ozone-dense air does contribute significantly to local ozone budgets (Konopka, Grooß, et al., 2010; Ploeger, Konopka, et al., 2012). This information forms a foundation for the work of Chapter 5.

The ozone distributions which arrive after all these processes show the densest mixing ratios in the tropical middle stratosphere, which is just slightly above 10 ppmv and occurs around 10 hPa (Figure 2.11). Climatological zonal-mean ozone mixing ratios decrease monotonically with distance from this location (except for an eventual increase near the surface, which is not shown in Figure 2.11). Also visible from this image is the effect of downward extratropical transport of ozone, which makes ozone concentrations in the LMS denser in the extratropics than in the tropics, as air with high odd-oxygen concentrations is carried downwards towards these regions.

The total overhead ozone column is typically measured in Dobson units (DU), which is the thickness of the layer of pure ozone which would be created from all overhead ozone at standard temperature and pressure (0 C and 1000 hPa). Although the highest ozone mixing ratios are found in the tropics, the overhead ozone column is generally thicker in the extratropics than in the tropics. This is not readily apparent from the zonal-mean distribution of ozone mixing ratios as shown in Figure 2.11, as the air with relatively weak ozone mixing ratios in the lower stratosphere provides a much greater share of total column ozone due to the higher pressures there, compared with deeper-stratospheric, ozone-rich air. However, this location (the extratropics) is also where the weakest overhead ozone column is found, namely that of the southern polar region during summer, typically referred to as the ozone hole. This feature has existed since the increases in chlorofluorocarbons (CFC's) during the later half of the 20th century. In contrast, the strongest overhead ozone columns are found in the northern polar region during spring. This is caused by the increased poleward transport during winter, which affects both polar regions. However, in contrast to the south polar vortex (where odd-oxygen is destroyed to form the ozone hole), the northern polar vortex is considerably warmer, which prevents the formation of polar stratospheric clouds (see, e.g., Solomon, Ivy, et al., 2017), a necessary factor for the rapid destruction of odd-oxygen which causes the ozone hole. Meanwhile, ozone columns have a rather small seasonal cycle in the tropics, but are weaker during winter, during which tropical upwelling is strongest (and hence ozone transport out of the tropics is also at its strongest).

2.3.3. Other Chemicals

Beyond water and ozone, a wide variety of chemical species have important effects on the stratosphere through radiative or chemical effects. An incomplete selection of these are CO_2, N_2O, CH_4, chlorofluorocarbons (CFC's, most significantly CFC11 and CFC12), and very short-lived substances (VSLS's). The increases in CO_2 due to the industrialization of human economic activity is well known to be the critical cause of global mean surface temperature warming, as well as related changes in global climate (Charney et al., n.d.; IPCC, 2013). These increases are also expected to decrease temperatures in the stratosphere, an effect which is as well-established as CO_2-related impacts on tropospheric temperatures. This impact (in isolation from other anthropogenic effects) is also expected to increase stratospheric ozone concentrations due to the dependence of ozone destruction reaction rates on temperature (see Section 2.3.2.2).

Oxidation of N_2O by monatomic oxygen is the primary source of NO in the stratosphere. Other nitrogen species are also produced from NO, such that the influx of N_2O into the stratosphere is the most important process affecting the stratospheric active nitrogen (i.e. non-N_2 budget). N_2O also has some effect on the stratospheric radiative budget – causing warming due to shortwave absorption – although these effects are of second-order compared to the effects of water and ozone. N_2O is produced in the troposphere and supplied to the stratosphere via upwelling through the tropical tropopause. N_2O is also emitted into the stratosphere by aircraft and in theory could be created *in situ* via photochemical production following gamma-ray bursts (Thorsett, 1995). A considerable portion (roughly one third) of the N_2O tropospheric source is due to human activity, which is another avenue for potential anthropogenic future climate effects on the stratosphere. More specifically, increases in N_2O emissions – in absence of other changes – would be expected to decrease stratospheric ozone concentrations (due to increased nitrogen-species-related ozone destruction) and contribute to increasing temperatures (amplifying the impacts of ozone reductions). The recent work of Dubé et al. (2020) has found signals of these increases in satellite observations of odd nitrogen species.

CH_4 is transported into the stratosphere from the troposphere. As mentioned earlier, the primary source of stratospheric water vapor created *in situ* is the oxidation of CH_4. Tropospheric concentrations of CH_4 are increasing due to anthropogenic emissions and environmental changes, and these changes might accelerate due to further changes such as permafrost melt (Saunois et al., 2020). These tropospheric increases also mean that stratospheric CH_4 concentrations should increase. As CH_4 is a particularly potent greenhouse gas, this future change implies substantial stratospheric cooling. Furthermore, the amount of water vapor created from oxidization would increase as well, providing an additional cooling effect on the stratosphere as well as greater odd-oxygen loss through greater concentrations of ozone-destroying hydrogen species.

2.3.4. Age of Air

As mentioned already, distributions of both ozone and water vapor show signs of transport effects. This is also the case for a variety of other tracers (carbon monoxide and methane, for example). However, all these species are chemically active in some way. In modeling and theoretical studies, passive tracers have been used to examine "pure" transport (i.e. without the influence of chemistry).

One particularly potent application of passive tracers is the age spectrum, which describes the distribution of an air parcel's "age" as defined by the transit time elapsed since exiting some reference location (typically the earth's surface, tropical surface, or the tropopause). The theoretical framework of the age spectrum begins with (T. M. Hall and Plumb, 1994)

$$\chi(\vec{r},t) = \int_0^\infty \chi(\vec{r},t-t')G(\vec{r},t|\vec{r}_0,t-t')\,\mathrm{d}t', \tag{2.19}$$

where χ is the mixing ratio of some conserved, passive tracer at a point $\vec{r}$ in space and t in time and $\vec{r}_0$ is some reference location. In this equation, G is the Green's function, and forms the basis of the age spectrum, as $G(\vec{r},t|\vec{r}_0,t-t')\,\mathrm{d}t'$ is the mass fraction of air (at point $\vec{r}$ and time t) which was at the reference location at some time $t'+\mathrm{d}t'$ earlier than t. An important feature of this framework is the mean age, which is

$$\Gamma(\vec{r},t) = \int_0^\infty t'\,G(\vec{r},t,t')\;\mathrm{d}t'\;, \tag{2.20}$$

or, in words, the first moment of the age spectrum. The age spectra width is defined as the second moment of the spectra centered around the mean

$$\Delta^2 = \frac{1}{2}\int_0^\infty (t'-\Gamma)^2\,G(\vec{r},t,t')\;\mathrm{d}t'\;. \tag{2.21}$$

The width quantifies the spread or dispersion of the spectra. An important parameter characterizing the shape of the age spectra is the "ratio of moments", which is defined as the spectra width divided by the mean Δ^2/Γ. The ratio of moments is also a critical parameter for estimating mean age from trace gas measurements (e.g., Volk et al., 1997; Bönisch, Engel, Curtius, et al., 2009; Engel, Möbius, et al., 2009; Hauck, Fritsch, et al., 2019; Hauck, Bönisch, et al., 2020), where the value is typically prescribed for the applied inverse method. The reader is encouraged to view T. M. Hall and Plumb (1994) or D. Waugh and T. Hall (2002) for thorough theoretical discussions on the age spectrum.

2.4. Expected Trends

2.4.1. Temperature

During the last century, stratospheric temperatures decreased due to the combined effects of increasing GHG concentrations and ozone depletion, which itself was caused by increasing concentrations of ozone-depleting substances, mostly chlorofluorocarbons. After the Montreal protocol was applied in 1989, concentrations of ozone-depleting substances began to decrease, and stratospheric ozone concentrations increased in consequence. Stratospheric temperatures have been much more stable during this later period (Aquila et al., 2016; Randel, Smith, et al., 2016)).

2.4.2. Water Vapor

Water vapor trends are discussed in Section 4.5 in depth. This discussion is located there due to its high relevance with the results of Chapter 4.

2.4.3. Ozone

Changes in ozone in the future are expected due to a variety of underlying processes. Recent CCM results suggest that ozone mixing ratios should increase throughout much of the stratosphere (see Figure 2.13), with the largest increases in the southern extratropical lower stratosphere. These increases are consistent with the "closing" of the southern ozone hole due to the decrease of CFC concentrations. Increasing ozone mixing ratios in the southern stratosphere are also apparent as increases in the total ozone column in this region. Not shown in Figure 2.13, but shown elsewhere in Keeble et al. (2020), is the robustness of this increase over a variety of GHG emissions scenarios (see Figure 18 in that paper), which demonstrates that the process of the ozone hole healing is to first order unaffected by the processes of a changing climate. However, these processes are expected to change the rate of the ozone hole recovery to some extent, due to changes in the stratospheric circulation (see Section 2.4.4) (see also Butchart and Scaife (2001)).

Ozone is also expected to increase in the deeper stratosphere, likely as a consequence of decreasing temperatures in that region which reduces the reaction rates of the odd oxygen catalytic destruction cycles. While this change in the chemical destruction processes of odd oxygen should take place in the entire stratosphere, the changes are unlikely to cause significant direct changes in the lower stratosphere (below about 25 km as suggested by Figure 2.8) due to the relative unimportance of odd-oxygen chemical destruction processes there. The lower stratosphere is also the only region where ozone concentration decreases are expected from CCM results, caused by the acceleration in tropical upwelling (see Section 2.4.4). This change would increase the removal of ozone from that region, or, in a Lagrangian sense, decrease the residence time of parcels within that region, which would reduce the time over which odd oxygen is allowed to accumulate through photochemical production as it rises there.

While these results are robust over a variety of CCM's, trends in ozone from observations are not yet completely clear on all of these changes. For example, there has been considerable discussion in recent years over the trends in lower stratospheric ozone, especially after the contribution of Ball et al. (2018). The changes found by Ball et al. (2018) were consistent with increases in the stratospheric circulation, and were statisically significant under the methods they employed. However, work by other groups in response to this suggested that the changes found might be a result of the strong dynamical variability in the tropical lower stratosphere (Chipperfield et al., 2018). One location where clear trends are found in observations is the ozone hole, showing signs of recovery. However, some work has suggested that CFC emissions have increased in recent years, which would be disastrous for the continued health of the ozone layer (Montzka et al., 2018). While these trends are certainly concerning, the cause of them is not yet clear, although likely related to new and uncontrolled CFC-11 emissions from Eastern China (Rigby et al., 2019), and the best response to this alarm is further research on the topic.

2.4.4. Residual Circulation

The overall strength of the residual circulation is expected to increase with anthropogenic climate forcing. This phenomenon is based on model results, for example in the work of Hardiman, Butchart, and Calvo (2013) as shown in Figure 2.14. Of the models used in that work, all of them show substantial trends in tropical upwelling strength, making the acceleration of the residual circulation a highly robust result of climate change simulations. These trends are approximately a 2-3% acceleration per decade (not shown in Figure 2.14). Although this result is robust across a variety of models, calculating this trend within a model is accompanied by the challenge of the high variability of the residual circulation strength (Hardiman, P. Lin, et al., 2017).

Due to this high variability, identifying these trends within model data requires long timeseries, such as those from the CMIP5 models used in Hardiman, Butchart, and Calvo (2013), which are 240 years long. This furthermore suggests that the estimation of residual circulation trends from observations may require long-term records. These estimations have as yet been performed either through calculations of the upwelling from reanalyses or non-quantitative estimations of upwelling trends via age-of-air. Reanalysis estimates represent the most "direct" method of calculating residual circulation timeseries, in so far as the data provided can be used to calculate residual circulation velocities, whereas age-of-air data does not provide velocity estimations. However, the recent work of Linz et al. (2017) suggested that inter-hemispheric gradients in age of air may be used to calculate the strength of the residual circulation, providing a method for expanding the utility of age of air estimates. In either the case of reanalysis data or age of air calculations, estimations of residual circulation trends have as yet been non-conclusive. Reanalysis estimates, for example, show long term trends that are in general agreement (i.e. a slow acceleration of the stratospheric circulation) but do not show clear, consistent agreement over shorter (i.e. decadal) timescales, both when estimated directly (Abalos, Legras, Ploeger, et al., 2015) and

from age-of-air calculations (Ploeger, Legras, et al., 2019).

Trends in age of air have also been calculated both from satellite data Stiller, Clarmann, et al. (2012) and balloon-borne observations. The latter observations are described by Engel, Möbius, et al. (2009) and more recently Engel, Bönisch, et al. (2017). These results show weak positive trends in age-of-air, which would suggest – in contrast with model results – a weakening of the stratospheric circulation. However, Engel, Bönisch, et al. (2017) also found the trend to be statistically insignificant, and later work by Fritsch et al. (2020) showed that an optimization of the calculation's parameter settings produced trends which were close to zero and statistically indistinguishable from model trends. Based on satellite observations of long-lived tracers, Stiller, Fierli, et al. (2017) found negative trends in southern-hemispheric age-of-air and positive trends in the northern hemisphere. This result is consistent with that of Engel, Bönisch, et al. (2017), as the measurements used in that work were performed in the northern hemisphere. However, this result still does not provide confirmation of an overall acceleration of the residual circulation. Stiller, Fierli, et al. (2017) instead interprets their results as indication of a shift in the location of stratospheric transport barriers. Conclusive observation-based confirmation or refutation of the acceleration of the residual circulation therefore remains as yet elusive.

2.5. The Development of Stratospheric Transport Models

Atmospheric models (as used in current coupled chemistry climate models) employ different numerical schemes for solving trace gas transport, all of which introduce some unwanted, unphysical numerical diffusion. Numerical diffusion smoothes gradients and small-scale filaments in tracer distributions. Thereby differences in numerical diffusion cause differences in trace gas transport in different transport models, affecting the simulated distributions of trace gas species. Research has been focused on this topic for decades, with early work performed by Rood (1987) examining transport in one dimension. Numerical diffusion in multi-dimensional models can be studied using a variety of tracers and methods. Both T. M. Hall, D. W. Waugh, et al. (1999) and Eluszkiewicz et al. (2000) used mean age of air as a diagnostic of transport. Eyring et al. (2006) also used mean age of air in this direction, but included methane and ozone as well, and the quasi-one-dimensional tape recorder signal to examine differences in transport processes between chemistry climate models (among other model differences). Similarly, Gregory and West (2002) used the tape recorder signal in a more focused study on numerical diffusion. These studies found significantly younger stratospheric mean age of air and a faster water vapor tape recorder propogation for more diffusive transport schemes. Kent, Ullrich, and Jablonowski (2014) provides a detailed analysis of idealized tracers and transport scenarios, but most recently this has been performed by Gupta, Gerber, and Lauritzen (2020), who studied a variety of dynamical cores using mean age of air as a transport diagnostic. Their results

demonstrate that many issues with numerical diffusion are still relevant with modern techniques and computational resources.

Most currently-used transport schemes are based on a regular and fixed grid (e.g., Morgenstern et al., 2010). In this work these schemes will be referred to as Eulerian schemes. Another class of transport schemes, Lagrangian schemes, follow the motion of air parcels through the atmospheric flow, and hence have reduced diffusion characteristics due to the absence of interpolations of tracer distributions to a regular grid (e.g., McKenna et al., 2002). In fact, a "pure" Lagrangian scheme has no inter-gridpoint numerical diffusion at all, and diffusion must be added to the model through some parameterization. Semi-Lagrangian schemes are still based on a regular grid, but incorporate some advantages of Lagrangian transport by calculating the air motion over one model time step through a Lagrangian advection scheme, but this is then followed by remapping onto the grid. One such scheme which is both sophisticated and frequently used in global models is the flux-form semi-Lagrangian (FFSL) scheme (e.g., S. Lin and Rood, 1996; S. Lin, 2004).

Fully Lagrangian transport schemes, by definition, are free of numerical diffusion, as parcels are left entirely isolated from each other when no inter-parcel mixing scheme is applied. Parcel mixing due to small-scale processes (e.g., turbulence) can then be introduced based on physical parameterizations and the strength of mixing can then be controlled. Due to the complications of handling irregular (air parcel) grids, Lagrangian schemes are not commonly used in global climate models. To the knowledge of the author, the only two Lagrangian transport schemes which are currently implemented in a global climate model are ATTILA (Stenke et al., 2008; Stenke et al., 2009; Brinkop and Jöckel, 2019) and CLaMS (Hoppe, Hoffmann, et al., 2014; Hoppe, Ploeger, et al., 2016). Both these schemes have been integrated into the ECHAM/MESSy Atmospheric Chemistry (EMAC) climate model (e.g., Jöckel, Sander, et al., 2005; Jöckel, Tost, et al., 2016) and at the present time neither has been incorporated into another climate model. Other Lagrangian transport schemes also exist, (such as Flexpart, described by Pisso et al. (2019)) but have not been coupled into climate models. The major feature of the ATTILA and CLaMS schemes that enables their application into climate models is the parameterization of mixing.

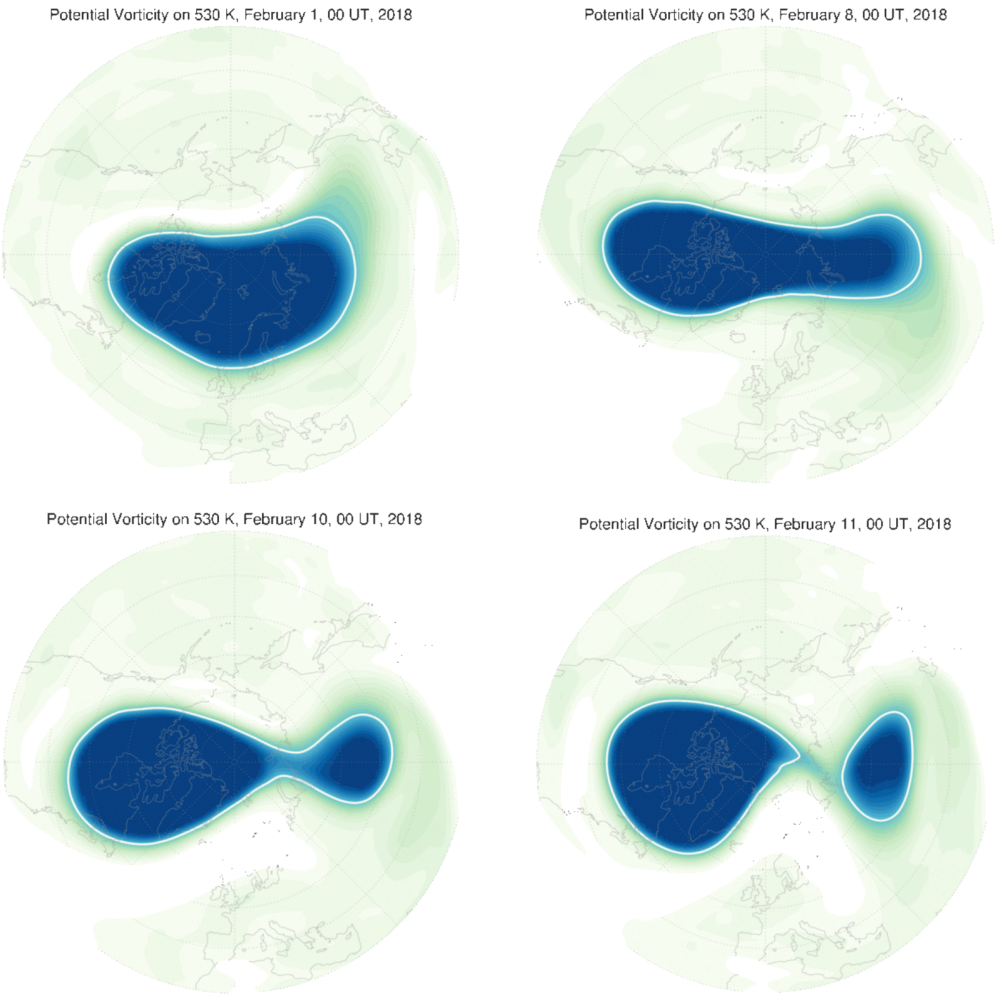

Figure 2.5.: Potential vorticity during the winter of 2017-2018 depicting the polar vortex split event of that year. From the website of Thomas Birner (https://www.meteo.physik.uni-muenchen.de/Thomas.Birner/SSW-animations/anim-PV/2018_530K/loop.html).

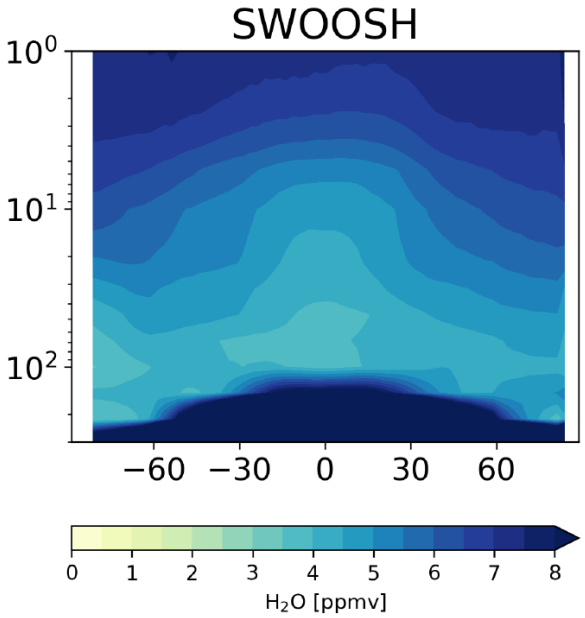

Figure 2.6.: Zonal-mean, climatological-mean (2000-2014) water vapor from the SWOOSH combined observations dataset. From Keeble et al. (2020) (their Figure 12).

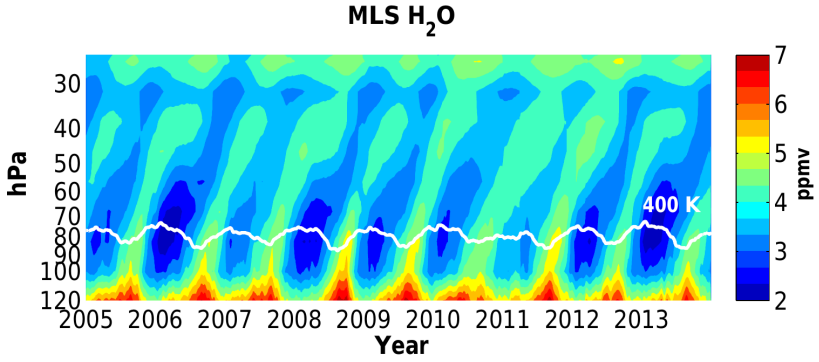

Figure 2.7.: The tape recorder signal seen in MLS satellite observations of water vapor between 10° S and 10° N. From Glanville and T. Birner (2017) (their Figure 1).

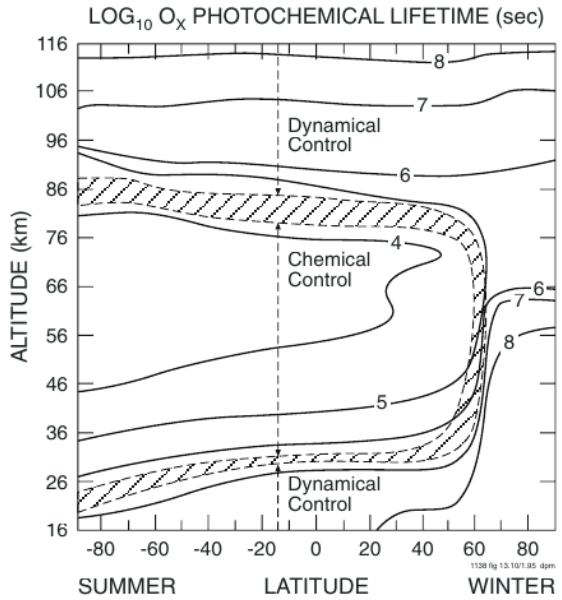

Figure 5.11. Photochemical lifetime of the O_x ($O + O_3$) family (logarithmic scale of values expressed in seconds). In the region of chemical control, the photochemical production and destruction are nearly in balance and steady state conditions can be adopted to derive the concentrations of O_3 and O. In the dynamically controlled regions, photochemical processes play a secondary role and O_x (primarily O_3 in the stratosphere and O in the thermosphere) is primarily influenced by transport processes. In the shaded region, transport and photochemistry play an equally important role. From Garcia and Solomon, 1985.

Figure 2.8.: From Brasseur and Solomon (2005).

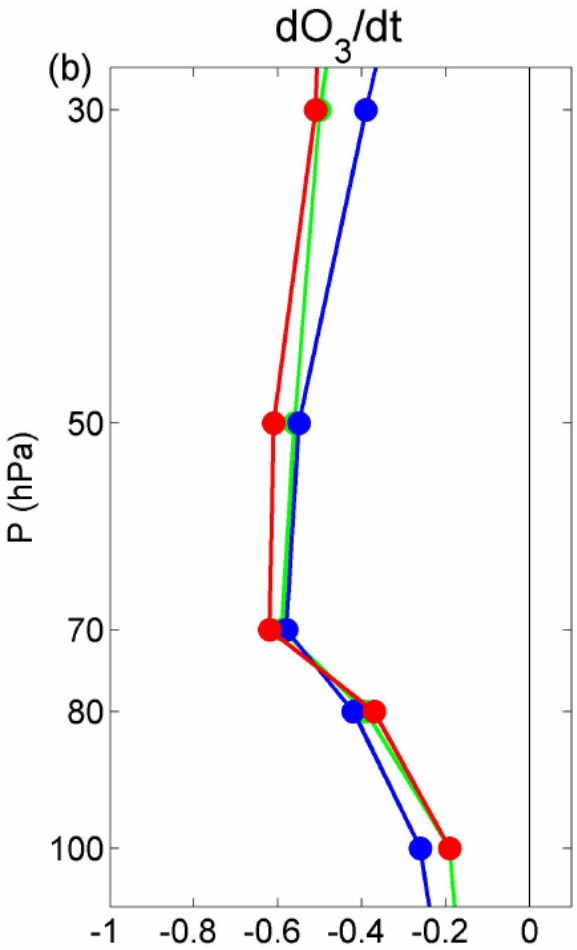

Figure 2.9.: Correlation of ozone tendency with reanalysis upwelling over the tropical lower stratosphere. From Abalos, Randel, and Serrano (2012) (their Figure 10).

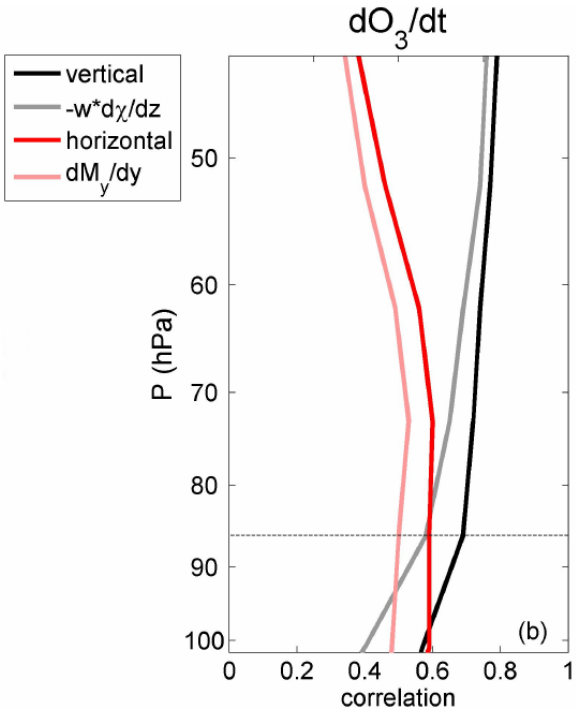

Figure 2.10.: Correlation of a climate model's ozone tendency with transport terms over the tropical lower stratosphere. From Abalos, Randel, Kinnison, and Serrano (2013) (their Figure 13).

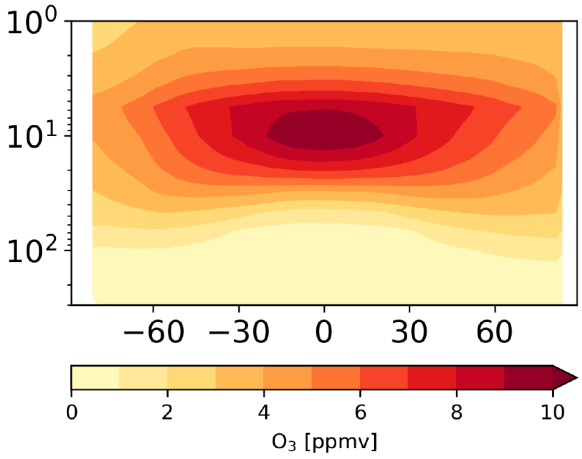

Figure 2.11.: Zonal-mean, climatological-mean (2000-2014) ozone from the SWOOSH combined observations dataset. From Keeble et al. (2020) (their Figure 4).

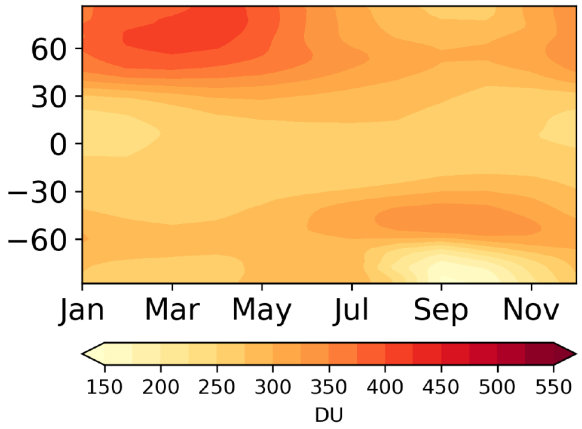

Figure 2.12.: Climatological (2000-2014) ozone columns from the SWOOSH combined observations dataset. From Keeble et al. (2020) (their Figure 4).

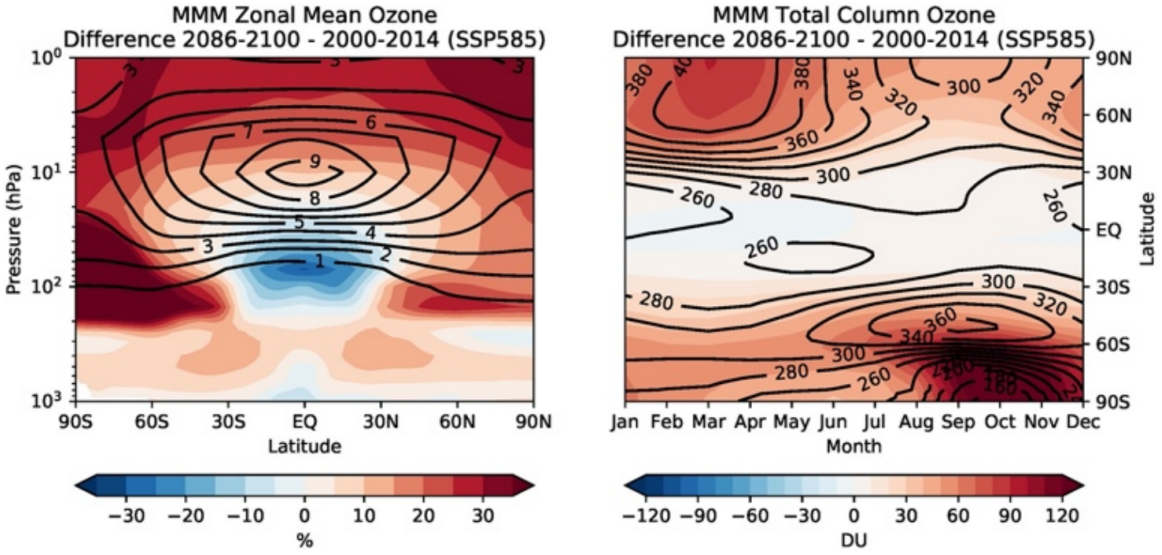

Figure 2.13.: Differences between zonal-mean, climatological-mean ozone observations (SWOOSH 2000-2014) and CMIP6 multi-model mean, zonal-mean, climatological-mean ozone. From Keeble et al. (2020) (their Figure 4).

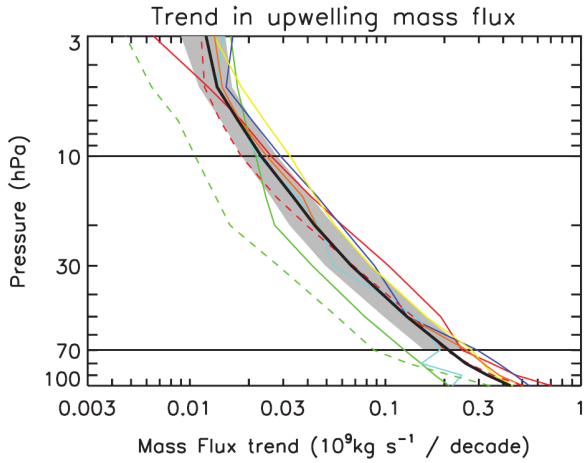

Figure 2.14.: Long-term mean trends in total upwelling mass flux (calculated between turn-around latitudes) from CMIP5 models. Solid black line shows multi-model mean upwelling mass flux. Grey shading shows inter-model standard error as 95% confidence interval. Colored lines show means from individual models. From Hardiman, Butchart, and Calvo (2013) (their Figure 2).

3. Modeling Stratospheric Transport

3.1. Introduction

The upper troposphere and lower stratosphere (UTLS) is an important region for global climate as the chemical composition of radiatively active trace gas species there has crucial impacts on radiation and surface temperatures (e.g., Solomon, K. Rosenlof, et al., 2010). The entry of air masses into the stratosphere is controlled by the chemical and dynamical processes in the UTLS (e.g., Holton et al., 1995; Fueglistaler et al., 2009), presenting a challenge for understanding and modeling the region. To overcome this challenge, climate models must have a realistic representation of UTLS transport processes in order to provide reliable predictions and assist in robust theoretical development. For instance, in simulating the effects of geoengineering by sulfur injections into the stratosphere, uncertainties in the model transport representation could cause substantial uncertainties in the simulations (Tilmes et al., 2018; Kravitz and Douglas, 2020). Even small differences in composition caused by model differences in small-scale transport processes (e.g., turbulence, diffusion) may cause significant model spread in surface temperatures (e.g., Riese et al., 2012). This radiative effect of composition changes in the UTLS is particularly large for water vapour, but also substantial for other species like O_3, N_2O, and CH_4.

Critical processes for models are transport around the wintertime stratospheric polar vortex, stratosphere-troposphere exchange across the tropopause, and horizontal exchange between the tropical lower stratosphere (the tropical pipe, Plumb, 1996) and middle latitudes (for reviews of stratospheric transport processes see e.g., Plumb, 2002; Shepherd, 2007). The steep gradients in observed trace gas distributions in these regions are signs of transport barriers and regions of suppressed exchange, for example, around the polar vortex, at the edge of the tropical pipe, and along the extratropical tropopause. The representation of transport processes in the lower stratosphere in global models is prone to numerical diffusion, as tracer distributions in this region are characterized by sharp gradients and frequent small-scale filamentary structures (McKenna et al., 2002).

Stenke et al. (2008) showed that using the ATTILA scheme in EMAC reduced the excessive transport of water vapour into the lowermost stratosphere (LMS) and into polar regions and the associated cold bias in temperatures could be partly corrected. The representation of stratospheric ozone was also found to have been improved (Stenke et al., 2009). Hoppe, Hoffmann, et al. (2014) further showed that CLaMS transport within EMAC results in a more realistic representation of transport barriers around the southern polar vortex, due to reduced numerical diffusion

compared to the EMAC FFSL scheme.

Here, we build on the study of Hoppe, Hoffmann, et al. (2014) and further analyze the implementation of the Lagrangian transport scheme CLaMS within the EMAC climate model. We compare results from two tracer sets within one EMAC simulation: one set where transport is calculated using the EMAC FFSL scheme and one set using the CLaMS Lagrangian tracer transport scheme. To enable a more detailed analysis of composition and transport time scales, going beyond the average stratospheric transit time (the mean age, D. Waugh and T. Hall, 2002) as considered by Hoppe, Hoffmann, et al. (2014), we calculate the full (time-dependent) stratospheric age of air spectrum (the distribution of stratospheric transit times) of model transport schemes.

This chapter investigates the differences in transport in the lower stratosphere between these two transport schemes using the age spectrum, mean age, and idealized tracers as diagnostics. The work is focused on identifying the regions that are most sensitive to changes in the tracer transport scheme, assessing the time scales for which the transport schemes differ, and identifying the potential consequences for simulated chemical composition and geoengineering simulations.

In Section 3.2.1 the models used and diagnostic methods (age spectrum, forward tracers) are introduced. Section 3.3 presents the results from a global perspective, while Section 3.4 focuses on particular processes and regions. In Section 3.5 the transport scheme differences are discussed against the background of current research on stratospheric geoengineering. The main conclusions are summarized in Section 3.6.

3.2. EMAC-CLaMS and EMAC-FFSL

3.2.1. Models

The model used in this is EMAC, the MESSy (Modular Earth Submodel System) version of the ECHAM5 climate model (see Jöckel, Kerkweg, et al. (2010) for details on EMAC and Roeckner et al. (2006) for details on ECHAM5). EMAC is a modern chemistry-climate model which is commonly used for studies of the stratosphere and upper troposphere (Sinnhuber and Meul, 2015; Oberländer-Hayn et al., 2016; Fritsch et al., 2019), as well as studies of the troposphere. In this work, EMAC is operated at the T42L90MA spectral resolution, corresponding to a horizontal quadratic Gaussian grid of approximately 2.8° x 2.8° resolution with 90 vertical layers. One simulation is performed with this model, by which two sets of time-resolved tracer distributions were calculated. One tracer set was calculated with the standard EMAC FFSL transport scheme, and will be referenced as the Eulerian representation or EMAC-FFSL. The other tracer set was calculated with the CLaMS EMAC submodel, and will be referenced as the Lagrangian representation or EMAC-CLaMS.

The EMAC-FFSL transport scheme is the flux-form semi-Lagrangian (FFSL) scheme (S. Lin and Rood, 1996), which is used in many modern climate models. The EMAC-FFSL vertical coordinate is a hybrid sigma-pressure coordinate, which is another

common choice in the development of modern climate models. The time resolution of the EMAC simulation performed in this work is 12 minutes. The simulation consists of ten years of spin-up, with a following ten years of result production. The EMAC version used in this work is 2.53.1, and the model was free-running (i.e. not forced by meteorological fields). Although EMAC can be used for chemistry-climate model simulations, the configuration in this work did not simulate interactive chemical fields. The water vapor field, however, was interactive, and included stratospheric moistening via methane oxidation (see e.g., Revell et al., 2016). Sea-surface temperatures and sea ice were prescribed from the HadISST climatology (Rayner et al., 2003). Meanwhile, CO_2, CH_4, N_2O, CFC-11, and CFC-12 mixing ratios were fixed at 367 ppmv, 175 ppmv, 316 ppbv, 262 pptv, and 520 pptv, respectively, for calculation of radiation. Other details of the EMAC set-up are identical to those of Jöckel, Tost, et al. (2016).

CLaMS (the Chemical Lagrangian Model of the Stratosphere) is a Lagrangian chemical transport model based on three-dimensional trajectories and an additional mixing parameterization. The EMAC-CLaMS results in this work were produced with a resolution of approximately 3 million air parcels. Unique among Lagrangian models, CLaMS uses a mixing parameterization which is robustly based on physical principles. This parameterization is based on the critical Lyapunov exponent method, details of which can be found in Konopka, Steinhorst, et al. (2004). The vertical coordinate of CLaMS is a hybrid $\sigma - \theta$ coordinate (referred to as ζ) (Hoppe, Hoffmann, et al., 2014). Above the prescribed reference pressure of 300 hPa, ζ is identical to θ and therefore the vertical advection velocity throughout the stratosphere is identically the diabatic heating rate. CLaMS advection is normally driven by horizontal winds and diabatic heating rates from reanalyses (e.g., Konopka, Günther, et al., 2007; Ploeger, Legras, et al., 2019), however in EMAC-CLaMS advection of CLaMS parcels is driven by the horizontal winds and heating rates of EMAC. This advection is driven online, during execution of the simulation, so that the underlying velocity fields for advection in EMAC-CLaMS and EMAC-FFSL are exactly the same. However, there are two differences in how these fields are used by the transport schemes: (1) EMAC-CLaMS interpolates the horizontal winds onto parcel locations, whereas EMAC-FFSL uses the winds directly on the EMAC grid points; (2) as mentioned above, the vertical velocity of EMAC-CLaMS is the diabatic heating rate (calculated by EMAC), whereas EMAC-FFSL uses a kinematic vertical velocity (calculated by closure of the mass balance equation). The horizontal and vertical velocities in the two transport schemes are therefore consistent, but not actually identical. More details of EMAC-CLaMS are described by Hoppe, Hoffmann, et al. (2014) and Hoppe, Ploeger, et al. (2016).

3.2.2. Calculation of Age Spectra in a Model

The goal of this chapter is examination of differences in tracer transport between two advection schemes, for which analysis of passive tracers is ideal. This approach, as opposed to examination of chemically-active species, eliminates differences that could

arise through the differing chemical schemes of EMAC and the CLaMS submodel of EMAC. The diagnostic tool used in this chapter is the age spectrum, described in Section 2.3.4. In models, age spectra can be calculated by a series of tracers which are pulsed at some reference location (in this case the tropical surface). For such a tracer with a pulse in the source region at time t_i the mixing ratio $\chi^i(\vec{r}, t)$ at point $\vec{r}$ and time t can be normalized to the probability density for air of the transit time $\tau = t - t_i$, which is the value of the age spectrum.

$$G(\vec{r}, t, t - t_i) = \chi^i(\vec{r}, t) \; . \tag{3.1}$$

Therefore, a suite of pulse tracers provides the full transit time dependency of the age spectrum function G.

This boundary impulse response method has been used in a few other modelling studies to calculate fully time-dependent stratospheric age spectra (for further details see e.g. Li, D. W. Waugh, et al., 2012; Ploeger and T. Birner, 2016; Hauck, Fritsch, et al., 2019). In this chapter, the tracers are emitted over the course of thirty days, after which emissions are ceased, and one tracer is pulsed every three months, specifically in January, April, July, and October of each year, analogous to the set-up by Hauck, Fritsch, et al. (2019). Tracer emission is performed by prescribing the surface boundary mixing ratio in EMAC. Each tracer is therefore assigned an age based on when the tracer was emitted, and the combined set of tracers is used to create the age distribution. Forty tracers are utilized in total, such that the calculated age spectra span the course of ten years. After 10 years, mixing ratios of the oldest tracer are set to zero throughout the model domain and the tracer is re-pulsed, so that the age spectra always spans from 0 to 10 years. Furthermore, the spectra are normalized so that the integral of the spectra over transit time always equals one.

Due to the truncation of the age spectrum at 10 years of age, although a "true" age spectrum would show a significant fraction of air older than 10 years, the mean age is biased young. This fact is important to bear in mind in comparing the mean age described here to calculations in other studies (e.g., Li, D. W. Waugh, et al., 2012). It has been shown that the age spectrum tail can be extrapolated to infinity by fitting an exponential decay (e.g., Diallo, Legras, and Chédin, 2012) and the mean age can be corrected accordingly. However, to facilitate comparison between EMAC-FFSL and EMAC-CLaMS transport, we refrain from applying this tail correction and focus on the resolved part of the age spectrum with transit times younger than 10 years. The uncalculated differences in the spectrum tail at ages older than 10 years are likely small compared to the differences in the resolved section of the spectra.

3.2.3. Forward Tracers

One disadvantage of the analysis of age spectra is abstraction of results away from the transport of realistic chemically-active species, such as water and ozone. In the results that follow, considerable differences are found in age spectra between the two considered transport schemes. These results indicate distinct differences in tracer

transport, but do not directly predict contrasts in the transport of specific, chemically-active tracers. We therefore investigate additional idealized trace gas species to reflect the results in a less abstract form. In particular, we consider the case of tracers with the simplest chemistry possible - that of radioactive decay. By convoluting an air parcel's age spectrum with an exponentially-decaying weighting, the fraction of a hypothetical radioactive tracer with a decay lifetime T that would remain after transport from the tropical surface (the origin of the pulse tracers) can be calculated

$$\chi^T(r,t) = \int_0^\infty \chi_0^T \, G(r,t,\tau) \, e^{-\frac{\tau}{T}} \, \mathrm{d}\tau \; . \tag{3.2}$$

Here, χ_0^T is the tracer mixing ratio at the tropical surface.

Throughout this chapter, this quantity will be referred to as a "forward tracer", as it is computed forward from the knowledge of the age distributions throughout the model domain.

3.2.4. The EMAC-CLaMS Lower and Upper Boundary

A critical decision in this study lies in the way in which age tracers are pulsed. Differences in the age spectra between the two transport schemes would ideally stem only from differences in transport within the region of interest (the stratosphere and upper troposphere). As mentioned in the introduction, the two transport schemes differ greatly in the representation of convective transport, as EMAC-CLaMS does not account for parameterized convection, while in the grid-point representation the tracers are subject to a convective transport parameterization. To eliminate the effects of this difference below the upper troposphere, the age tracer concentrations of the EMAC-CLaMS representation were fixed to those of EMAC-FFSL below level 73 of the EMAC model. This level corresponds to 270 hPa (330 K) in the tropics and extratropics, and about 250 hPa (300 K) in the winter polar region (poleward of 75 degrees). The procedure is as follows: for each EMAC-CLaMS parcel at each timestep, the EMAC grid cell containing the parcel was identified and if the parcel was located at or below EMAC level 73, the EMAC-CLaMS parcel age tracer values were replaced by EMAC-FFSL age tracer values of that EMAC cell. In this way, EMAC-FFSL results do not qualitatively differ from those of EMAC-CLaMS below EMAC level 73 (the upper troposphere). There are, however, small quantitative differences between the two sets of transport scheme results due to interpolation and numerics because the two representations have different grids and resolutions in this region. This creates very minor differences which are most noticeable near the surface.

The model top in EMAC is at 0.01 hPa (approximately 80 km) (Jöckel, Tost, et al., 2016). As the CLaMS transport scheme has not been extended into the mesosphere so far, the uppermost level in EMAC-CLaMS results is around the stratopause (around 2500 K, see Hoppe, Hoffmann, et al., 2014). Therefore, in regions of downwelling air from the mesosphere, EMAC-CLaMS age of air will be young-biased compared to the EMAC-FFSL age. However, as this chapter focuses on the lower stratosphere, the

effect of these differences is expected to be weak. Furthermore, as the EMAC-CLaMS age is found to be generally older than the EMAC-FFSL age in the lower stratosphere (see Figure 3.1), these age differences can be regarded as conservative estimates of inter-representation differences.

3.3. Differences in the Zonal Mean State: Global Perspective

3.3.1. Mean age of air

Examination of mean age of air (in Figure 3.1) shows many qualitative similarities between the Lagrangian and Eulerian frameworks. In both representations, mean age gradually increases with distance from the tropical tropopause layer (TTL), the region from 355–425 K through which most tropospheric air entering the stratosphere passes (e.g., Holton et al., 1995; Fueglistaler et al., 2009; Butchart, 2014). At all potential temperature levels, mean age is lowest in the tropical stratosphere (tropical pipe, Plumb, 1996) and gradually increases towards high latitudes. Mean age is generally lower in the winter than the summer, consistent with stronger wintertime downwelling in the polar region (bringing older air from higher to lower levels) and the isolation of the polar vortex (which limits the intrusion of young air from lower latitudes). This structure in the mean age distribution agrees well with satellite observations (Stiller, Clarmann, et al., 2012) and other models (e.g., Hauck, Fritsch, et al., 2019).

The Lagrangian approach results in older air throughout most of the stratosphere. Above about 450 K, these differences are of quantitative nature and qualitatively the mean age distributions are similar during both seasons. A closer look shows that the particular contours are in somewhat different positions, especially around the polar vortexes. In particular, EMAC-CLaMS results show a lower extent of old polar vortex air than EMAC-FFSL, most easily seen in the 3- and 4- year contours, which are at lower altitudes in EMAC-CLaMS.

Below 450 K there are clear qualitative differences between the representations, most visible in the 1-year contour. This contour has nearly the same shape in the winter hemispheres in both transport schemes, but in the summer hemisphere this contour shows a qualitative inter-representation difference, particularly between 50 and 75 degrees latitude. In this region, between 350 K to 400 K, the contour shows an eave (a vertical inversion with young air extending over the subtropics, resembling a roof) in EMAC-CLaMS, but in EMAC-FFSL this contour rises towards the equator without showing an eave structure. In EMAC-CLaMS, the eave structure was found in the northern hemisphere during January in each year of the simulation, was less pronounced during October, November, and February, and was not found in any month during any year in the EMAC-FFSL results. For the southern hemisphere, the eave structure was found in the EMAC-CLaMS results in July and was less pronounced during April, June, and August. The inter-representation mean age differences which are associated with this eave structure are approximately half a year.

Quantitative differences are largest within the polar vortexes, with higher mean age in EMAC-CLaMS. Other comparison studies of Lagrangian and Eulerian transport have already found that Lagrangian transport produces higher mean age within the polar vortexes due to stronger vortex edge transport barriers (Stenke et al., 2008; Hoppe, Hoffmann, et al., 2014). The results of this chapter echo those findings, and show a slightly stronger inter-representation discrepancy in the southern polar vortex, reaching a maximum of 0.7 years (compared to 0.6 years in the northern polar vortex). The southern polar vortex also shows stronger confinement of the mean age differences, compared to the northern hemisphere. In particular, the 0.4 year contour around the southern polar vortex extends to 75° S, while in the north it extends nearly to 50° N. These results are likely due to the greater dynamical variability in the northern polar vortex (Butler et al., 2017). This greater dynamical variability likely causes blurring of the inter-representation discrepancy there, compared to the more consistent southern polar vortex.

Above 450 K, air is mostly older in EMAC-CLaMS than EMAC-FFSL. The largest differences occur at the edges of the tropical pipe (around 25° N/S) and in the summertime middle and high latitude stratosphere. The summer edge of the tropical pipe shows larger differences than the winter edge, particularly around 600 K. This particular point has been identified as a local minimum in diffusive activity by both Haynes and Shuckburgh (2000) and Abalos, Legras, and Shuckburgh (2016), suggesting that the large inter-scheme differences here (as well as the winter side of the tropical pipe) are due to weaker nonphysical diffusion in EMAC-CLaMS over EMAC-FFSL. Above 500 K in southern high latitudes, EMAC-CLaMS shows younger air than EMAC-FFSL. These differences could be caused by recirculation differences, but could also be impacted by the differences in the upper boundaries of the two transport schemes (see Section 3.2.1) and will therefore not be investigated further as these effects cannot be readily separated.

There are several other regions with notable quantitative inter-representation differences in mean age. On the northern and southern flanks of the region of horizontal outflow from the tropical tropopause layer (around 35° N/S and 400 K) EMAC-CLaMS shows younger air than EMAC-FFSL. This difference is stronger in the winter hemisphere (greater than 0.5 years) and weaker in the summer hemisphere (less than 0.5 years). Although these differences are much weaker compared to the differences in the polar vortexes, they are rather large when the mean age in these regions is considered (approximately 50% of mean age, similar to the polar vortexes). The differences in these regions are the counterparts to those within the polar vortexes; in the lower stratosphere EMAC-FFSL has older air near the boundaries of the tropical stratosphere and younger air within the polar vortexes due to stronger diffusion across the latitudinal age gradient along the polar vortex edge, creating a dipole feature in mean age differences.

3.3.2. Chemical Composition

Inter-representation differences in mean age are caused by differences in transport, meaning that simulations with chemically-active tracers would also show corresponding differences in chemical composition. As an example, in Figure 3.2 we consider an idealized chemical tracer with a 2 year lifetime and an exponential decay globally (analogous to the E90 tracer commonly used to evaluate model transport, e.g., (Prather et al., 2011; Abalos, Randel, Kinnison, and Garcia, 2017), see Section 3.2.3 for details), which we assume to have been emitted from the tropical surface at a mixing ratio of 1 ppbv. Difference patterns in this 2 year lifetime tracer are largely a mirror image of differences in mean age, as larger age means greater chemical loss for the idealized tracer from the original mixing ratio. However, the regions of highest sensitivity to the transport scheme differ somewhat for the 2 year tracer compared to mean age, as the tracer is less sensitive to changes in the spectrum tail. Maximum differences in tracer amount between EMAC-FFSL and EMAC-CLaMS are found in the polar vortex (up to 40%) and in the summertime lowermost stratosphere (LMS) (up to 20%). These results suggest that there could be substantial impacts of the chosen transport scheme on resulting chemical composition in these regions. Quantitative differences in the regions, however, depend on the tracer lifetime, and in the case of realistic observed chemical species, the particular sources and sinks of those species.

Figure 3.3 shows inter-representation differences in forward tracer mixing ratios at various locations for exponential decay lifetimes ranging from one tenth of a year to ten years. In all locations and for all lifetimes, EMAC-FFSL shows larger tracer mixing ratios than EMAC-CLaMS, related to younger age in these regions (compare Figure 3.1). The lifetime of highest sensitivity to the transport scheme varies considerably between the different regions. In the LMS maximum differences occur for trace gas species with a lifetime of a few months (red lines). In the polar vortex, on the other hand, maximum differences occur for lifetimes of a few years (blues). Relative differences (in percent) show a different dependency on lifetime (monotonic decrease), as the tracer mixing ratio decreases with lifetime at a given location (Figure 3.3). For short lifetimes, relative differences grow enormously in some regions. For instance in the polar vortex (both NH and SH) EMAC-FFSL tracer mixing ratios are higher than for EMAC-CLaMS by up to a factor 5. The southern polar vortex stands out as a region with extremely large differences in the entire lifetime range below about 2 years.

Figure 3.4 presents horizontal and vertical gradients of the 2-year lifetime forward tracer. Broadly speaking, the vertical gradients are strongest along the tropopause, while the horizontal gradients are strongest at the subtropical jets, the polar vortexes (most strongly at the southern polar vortex), and the edges of the tropical pipe. While this is true in the results of both transport schemes, EMAC-CLaMS always shows gradients which are as strong or stronger than those of EMAC-FFSL. In particular, the vertical gradients at the extratropical tropopause are approximately twice as strong in EMAC-CLaMS, as are the horizontal gradients at the southern polar vortex and

the edges of the tropical pipe. Meanwhile the horizontal gradients at the subtropical jets are approximately 50% stronger in EMAC-CLaMS than in EMAC-FFSL. These results suggest that the representation of transport barriers is substantially stronger in EMAC-CLaMS than in EMAC-FFSL. While this has been shown for the case of the polar vortex already by Hoppe, Hoffmann, et al. (2014) the analysis here generalizes these findings to all the aforementioned stratospheric transport barriers.

3.3.3. Inter-annual variability

Inter-annual variability in the mean age fields is shown in Figure 3.5. The results clearly indicate that the choice of transport scheme affects the simulated inter-annual transport variability. In both representations the greatest variability is found in the northern polar vortex and second to that at the edges of the tropical pipe. Whereas high mean age variability is found in the center of the northern polar vortex, for the southern polar vortex the strongest mean age variability is found at the edge of the vortex. This is the case in both schemes, and is likely to be primarily related to the frequency of sudden stratospheric warmings, which occur much more often in the northern polar vortex than the southern polar vortex. In EMAC-FFSL, the mean age variability at the southern polar vortex edge is roughly equal to the variability found at the edges of the tropical pipe. However, in EMAC-CLaMS the variability at the edges of the tropical pipe is roughly twice as strong as the variability at the edge of the southern polar vortex. The inter-representation difference in this comparison is partially due to stronger southern polar vortex edge variability in EMAC-FFSL than in EMAC-CLaMS. However, this discrepancy is smaller than the inter-representation difference in tropical pipe edge variability; variability at the tropical pipe edges is about twice as strong in EMAC-CLaMS as in EMAC-FFSL. This is also the case in the northern polar vortex, where mean age variability is about 50% stronger in EMAC-CLaMS than in EMAC-FFSL.

Figure 3.6 shows inter-annual variability normalized by local mean age. From this prespective, the northern polar vortex still appears as a hotspot of variability and is still stronger in EMAC-CLaMS than in EMAC-FFSL. Conversely, the southern polar vortex edge shows much weaker variability compared to other locations, due to high mean age values in that region, and appears to have variability of approximately equal magnitude in both representations. The largest difference in this perspective from that of absolute difference values is found around the tropical tropopause. Variability in this location is stronger in EMAC-FFSL than in EMAC-CLaMS. Furthermore, in EMAC-FFSL this variability is strongest beyond the subtropical jets, rather than at the tropical tropopause (i.e. equatorward and upward of the subtropical jets). In the case of EMAC-CLaMS, variability beyond the subtropical jets is of a similar magnitude to variability along the tropical tropopause. These findings could indicate a critical role for transport across the subtropical jets to cause the differences in the eave structures in the age distribution between the Lagrangian and Eulerian frameworks (see Figure 3.1). Analysis of the age spectra in Section 3.4.2 will shed more light on the reasons for the occurrence of the eaves.

3.3.4. Age spectrum shape

Spectra width ranges from near zero to almost 2.5, with the lowest values found in the troposphere and the highest values found in the most troposphere-remote regions of the stratosphere, like the extratropical middle stratosphere and the polar vortexes (not shown). The summertime eave pattern in EMAC-CLaMS found in mean age and forward tracer contours is also seen in spectra width as a region of higher widths (not shown). Figure 3.7 shows the ratio of moments from the age spectra. In general, the ratio of moments is relatively small in the tropics, related to narrow age spectra there, and increases in middle latitudes where age spectra are broader. The ratio of moments is larger in the summer compared to the winter hemisphere. The decrease at the upper levels and in the polar vortex is, to some degree, related to the truncation of the spectra at 10 years, which causes slight underestimation of age spectra width. The patterns agree qualitatively with results from other models (e.g., T. M. Hall and Plumb, 1994; Hauck, Fritsch, et al., 2019). Quantitatively, the ratio values are lower than those found in the recent study by (Hauck, Fritsch, et al., 2019), which is related to the truncation of the spectrum tail here and should not be viewed as contrary to those results.

The inter-representation ratio differences (Figure 3.7, b and e) show that the ratio of moments (hence the spectrum shape) is sensitive to the transport scheme used. Throughout most regions of the stratosphere, the ratio of moments is larger in EMAC-FFSL than EMAC-CLaMS. The largest differences (up to 40%) occur in the winter hemisphere subtropics at potential temperature levels between about 350 K and 450 K. In this location, EMAC-CLaMS shows a very localized region of low spectrum moment ratios, while EMAC-FFSL shows a much weaker minima and only shows this in the southern tropics.

The summertime LMS is the only region where the ratio of moments is larger in EMAC-CLaMS than EMAC-FFSL. A remarkable feature is the vertical dipole in the summertime subtropical lowest stratosphere with larger ratios below (around 350 K) smaller ratios (around 380 K). In other words, at this location relatively broad spectra reside below narrower spectra. This characteristic in the ratio of moments is much more clear in EMAC-CLaMS than in EMAC-FFSL and is likely related to the eave structures found in the mean age distribution in EMAC-CLaMS. The details of the age spectra in this region will be investigated in Section 3.4.2.

3.4. Differences in the representation of transport processes

To gain further insight into inter-representation differences in transport processes, we turn our investigation to the stratospheric age spectrum. The discussion in this section is subdivided according to the regions with the most significant differences: the tropical and mid-latitude stratosphere, the polar vortexes, and the LMS.

3.4.1. Tropical and mid-latitude stratosphere

Due to strong polar downwelling motion and the cyclonic circumpolar flow, air masses inside the wintertime stratospheric polar vortexes are largely isolated against exchange with middle latitudes, even more so in the southern hemisphere, where the cyclonic circumpolar flow is stronger than in the northern hemisphere. Figure 3.9b shows the age spectra within the southern stratospheric polar vortex. Below 3 years, the spectra show clear qualitative differences. EMAC-FFSL shows two peaks in this region: one at 2.5 years and the other at 1.25 years. Meanwhile EMAC-CLaMS shows only one peak, which is at 2.5 years. The common peak at 2.5 years is much stronger in EMAC-CLaMS than in EMAC-FFSL. The contribution from air younger than 2 years is about twice as strong in EMAC-FFSL as in EMAC-CLaMS. This much higher fraction of young air inside the polar vortex in EMAC-FFSL than in EMAC-CLaMS is caused by stronger diffusive transport across the vortex edge in the FFSL transport scheme. This difference suggests that simulations of chemically-active tracers with short stratospheric lifetimes and tropospheric origins would show substantially stronger southern polar vortex concentrations in EMAC-FFSL, compared to EMAC-CLaMS. For long-lived trace gas species differences would be smaller. Consequently, the amount of ozone-depleting substances in polar regions with lifetimes below a few years and related polar ozone loss can substantially differ depending on the chosen transport scheme.

Variability in the age spectra seem to be roughly similar at most ages, but is substantially different below 3 years of age, with much more variability in EMAC-CLaMS at the 2.5 years peak and much more variability in EMAC-FFSL below 2 years of age. At ages older than 3 years the age spectra are qualitatively similar, showing multiple maxima at 1-year intervals at the half-year marks, and regular minima at the 1-year marks. This means stronger contribution of air emitted during January, and weaker contribution of air emitted during July. Both schemes show this quality, with EMAC-CLaMS showing a greater difference between the contributions at the maxima and minima.

Figure 3.9a shows age spectra within the northern polar vortex. As in the southern polar vortex, ages above 3 years show qualitative similarity between the representations; maxima in the spectra correspond to January-emitted tracers while minima correspond to July-emitted tracers. At ages younger than 2.75 years, EMAC-FFSL shows greater tracer concentrations than EMAC-CLaMS. However, the difference between the two representationss in this location for young ages is much smaller than the difference in the southern polar vortex, while variability in the age spectra is much stronger (approximately a factor of 2) in EMAC-CLaMS than in EMAC-FFSL.

3.4.2. Lowermost Stratosphere

A particularly interesting feature in the mean age and tracer distributions in the summertime LMS in Figures 3.1 and 3.2 is the eave structure. The structure - only found in EMAC-CLaMS - has two features: an old-air region at the level of the

subtropical jet (around 360 K) and a young-air region above that (around 400 K). Conversely, in EMAC-FFSL these two regions have similar age . As the mean age and forward tracer contours in Figures 3.1 and 3.2 in the upper region follow similar paths in both representations, transport from the upper region into the lower region is not likely to play a role in the discrepancy of the eave structure representation. Therefore, the eave structure, as present in EMAC-CLaMS, probably arises from weaker direct transport from the troposphere (i.e. not through the tropical tropopause layer) into the lower eave region, in comparison to EMAC-FFSL.

To gain more insight into the underlying processes, Figure 3.10 shows the corresponding age spectra for the two schemes at the 360 K and 400 K levels between 50-60 degrees latitude. In both cases, the upper level age spectra are very similar in both EMAC-FFSL and EMAC-CLaMS. In the southern hemisphere in particular, these spectra are nearly identical, with only slightly more tracer between 0.5 and 1.5 years of age found in EMAC-CLaMS. Meanwhile the northern hemisphere results show somewhat less agreement between the two representations in the upper levels, with slightly less tracer at 0.25 years and somewhat more tracer between 0.5 and 1.0 years in EMAC-CLaMS. However, there is considerable inter-representation difference in the relationship between the age spectra in the upper region and the lower region; EMAC-FFSL results show nearly identical spectra in both regions, while EMAC-CLaMS shows a consistent difference in the upper and lower region spectra. In the EMAC-CLaMS spectra for both hemispheres, the upper region shows more air younger than 0.5 years while the lower region shows more air between 0.5 years and 1.5 years, and both regions show nearly identical contributions from air at 0.5 years.

The differences in age spectra, mean age, and tracer mixing ratios suggest that the eave structure in the LMS is caused by an interplay of transport processes as described in the following: The LMS mean age distribution results from a mixture of old air masses downwelling from the stratosphere and young air masses transported into the region by the shallow branch of the BDC (e.g., Bönisch, Engel, Curtius, et al., 2009). In spring and summer, a new transport pathway emerges which is related to upward transport in the tropics and poleward transport directly above the subtropical jet, and characterized by transport time scales of about half a year to 1.5 years. This poleward transport happens in the layer of about 380–450 K, which belongs to the region above the subtropical jet and below the tropical pipe. Fast transport in this layer agrees well with the existence of a tropically controlled transition region for water vapour as proposed by K. H. Rosenlof et al. (1997). The EMAC-CLaMS simulation shows a clear age inversion related to this flushing of the extratropical LMS with young air above the jet. In the EMAC-FFSL simulation, on the other hand, this feature is totally absent because a much higher fraction of young air with transit times shorter than 0.5 years blurs the old air signature in the layer around 350 K.

Hence, the Lagrangian and Eulerian transport schemes result in different preferences for transport pathways into the summertime LMS: poleward transport above the jet (Lagrangian) versus cross-tropopause transport at levels below (Eulerian). It remains to be shown from trace gas observations in the LMS whether the eave structure evident in the age distribution from Lagrangian transport is a feature of

the observed atmosphere. Initial indications for a mixture of old wintertime air and young air masses from transport above the subtropical jet in that region during early spring have already been found in aircraft in-situ measurements of N_2O and CO by Krause et al. (2018).

3.5. Discussion

The results of the work presented thus far have shown substantial differences in tracer transport between EMAC-FFSL and EMAC-CLaMS. Given that the FFSL transport scheme used by EMAC is also used in a wide array of other climate models, the effects of unphysical numerical diffusion in EMAC-FFSL which have been described here are likely to affect tracer transport in other climate models as well. This could cause complications for the interpretation of results from these models, especially for stratospheric transport. One such topic, for which there is considerable modeling activity at the moment, is geoengineering through stratospheric aerosol injection (SAI). This has been proposed as a method to reduce or entirely offset the surface temperature effects of global warming (e.g., Crutzen, 2006) and is likely to gather more attention as the global mixing ratios of greenhouse gases rise. Relatedly, the latest-generation climate models from the Coupled Model Intercomparison Project phase 6 (CMIP6) show an even stronger equilibrium climate sensitivity and simulate stronger climate warming than the model generation before (Forster et al., 2020) further fueling discussion about solar geoengineering.

A modelling effort to assess the opportunities and risks of solar geoengineering using stratospheric sulfate aerosols within the Geoengineering Large Ensemble (GLENS) project has recently been presented by (Tilmes et al., 2018). In this project, injection strategies have been proposed to maintain the distribution of global surface temperatures in the future, and potential side-effects (e.g., on precipitation and stratospheric ozone) have been discussed (Kravitz and Douglas, 2020). Although the results of that work suggest that it may be possible to use SAI successfully (i.e., to maintain the global distribution of surface temperatures), the authors note that a main uncertainty in their model results is related to stratospheric transport processes and their representation in current climate models.

Our model experiment, which applies one climate model with two different transport schemes in the same simulation, is well-suited to shed further light on this uncertainty of geoengineering projections related to uncertainties in air mass dispersal due to the model representation of stratospheric transport. It is noteworthy here that this discussion concerns air mass transport and not the transport of sulfate, as our simulation does not include stratospheric chemistry. However, we consider a state-of-the-art transport scheme (EMAC-FFSL) which is also applied in other current climate models and a novel Lagrangian scheme (EMAC-CLaMS) which has significantly less numerical diffusion. As results from this chapter show, two regions emerge where transport differences between the two representations are especially large: the LMS and the polar vortex. Both are critical regions for the processes which affect the effi-

cacy of SAI. In particular, sulfate concentrations in the LMS crucially affect radiative forcing, whereas sulfate concentrations in the polar vortex control the side-effects of geoengineering on stratospheric ozone.

To illustrate the potential differences in geoengineering simulations caused by model transport representation, we modified our experiments to include continuous point-source injections of tracers with idealized chemistry. The injection is handled by forcing the tracer mixing ratio to 1 ppbv within a region of nine EMAC grid cells (3-cells wide both east-west and north-south). The idealized chemistry is represented by a global exponential decrease with 30-, 90-, and 365-day lifetimes. Figure 3.11 shows the dispersal of a 365-day lifetime tracer which was injected at 30° N and 180° E at the 89 hPa pressure level. The results are shown for the two transport schemes after about 5 years of simulation and the results represent the state of the simulation on a single timestep. Both models show three regions with high tracer mixing ratios: (1) a plume between 300° E and 330° E which is the most prominent feature of the snapshot; (2) a second plume west of 260E and between 40-50S; (3) and then a third local maxima of tracer mixing ratios in the upper northwest corner of the image. In the EMAC-FFSL results this latter region seems to be separate from the others in the image, while in EMAC-CLaMS this region seems to be connected to the main plume by a trail of weaker tracer mixing ratios. In both features (1) and (2), EMAC-CLaMS results show higher mixing ratios in the centers of the plumes. In feature (1), these mixing ratios even reach nearly as high as the emission mixing ratio (1 ppbv), showing that the central area of the plume remained isolated during transport over 60 degrees of longitude. In comparison, the highest mixing ratios found in EMAC-FFSL are about 0.45 ppbv - half the emission mixing ratio. Furthermore, there is clearly a much wider variety of small-scale features in the results of EMAC-CLaMS compared to those from EMAC-FFSL. Hence, the stronger numerical diffusion in EMAC's FFSL transport scheme blurs small-scale features and filaments compared to Lagrangian transport and results in a more homogeneous tracer distribution.

Global tracer distributions from the two models at the end of the 5 year simulation period (for the 365 days lifetime tracer) are shown in Figure 3.12 for the case of austral spring (September–November). The tracer plume extending from the injection source location in the southern subtropics towards the south pole is broader and more smeared out in EMAC-FFSL than EMAC-CLaMS, also related to the differences in numerical diffusion. The difference figure (Figure 3.12) indicates even clearer that for EMAC-CLaMS the plume is more centered around its core whereas for EMAC-FFSL it is broader with more tracer above and below. In particular inside the polar vortex (poleward of about 60° S), tracer mixing ratios are substantially (approximately 35%) higher for the more diffusive FFSL transport scheme.

These differences emerge for all injected tracers considered, including over each of the lifetimes of 30, 90, and 365 days. We therefore expect that for realistic chemistry there should also be significantly higher sulfur concentrations in polar regions for more diffusive model transport schemes, compared to Lagrangian schemes. As relative differences in the polar vortex are substantial, we expect a large uncertainty of simulated ozone depletion from geoengineering sulfur injections related to the used

model transport scheme. Narrowing this uncertainty further down, in particular using simulations including appropriate stratospheric chemistry for sulfur and ozone, should be a priority for future research in this direction. For the moment, in view of such large uncertainties in stratospheric transport in current models and the potential dangers of SAI geoengineering, real-world applications of SAI remain highly questionable and inadvisable.

3.6. Conclusions

In this chapter, we have assessed the impact of the choice of trace gas transport scheme on the representation of stratospheric transport. The two transport schemes that we have studied are the Lagrangian scheme of CLaMS and the Eulerian FFSL scheme of EMAC, the latter of which is commonly used in modern chemistry-climate models. Differences in transport time scales were investigated by comparing the full time-dependent age spectrum and idealized, radioactively-decaying forward tracers in representations from both schemes. The results show that stratospheric transport barriers are, in general, much stronger in simulations with Lagrangian trace gas transport whereas they are weaker for the FFSL scheme due to stronger, unphysical numerical diffusion associated with the latter method. These results are broadly consistent with previous studies comparing Lagrangian and Eulerian transport, in particular the works of Hoppe et al. 2014, 2016 and Stenke et al. 2008, 2009, both of which found slower transport and stronger transport barriers in Lagrangian schemes. These conclusions hold for the transport barriers around the polar vortex, along the subtropical jets, and at the edges of the tropical pipe. Two regions of the stratosphere emerge from the simulations for which differences caused by the transport scheme are particularly large: (i) the polar vortex and (ii) the summertime LMS. Inside the polar vortex, the air is substantially older in the Lagrangian transport simulation due to reduced diffusive transport from middle latitudes through the vortex edge. Consequently, chemical tracers with short lifetimes show much lower mixing ratios. Also in the LMS, the air is much older for the Lagrangian simulation, as diffusive cross-tropopause transport of young air from the troposphere is reduced.

In particular, a very different structure in the age of air and tracer distributions emerges in the summertime LMS in the two representations. The Lagrangian representation of EMAC-CLaMS shows an age inversion structure, or eave, where older air resides below younger air, while this feature is entirely absent in the EMAC-FFSL results. This structure is related to fast poleward transport above the jet, which creates the young air layer above the older air. In the EMAC-FFSL results, strong diffusive cross-tropopause transport totally blurs this layered structure.

The results of this chapter show that a fully Lagrangian transport scheme (that of CLaMS) results in significantly less numerical diffusion, stronger stratospheric transport barriers, and clearer structures in trace gas distributions (e.g., gradients, filaments), even when compared to a sophisticated, state-of-the-art flux-form semi-Lagrangian scheme (that of EMAC). Differences in simulated trace gas transport

related to the choice of the transport scheme raise important questions about the uncertainty of stratospheric transport in climate model simulation, and in particular for geoengineering model experiments.

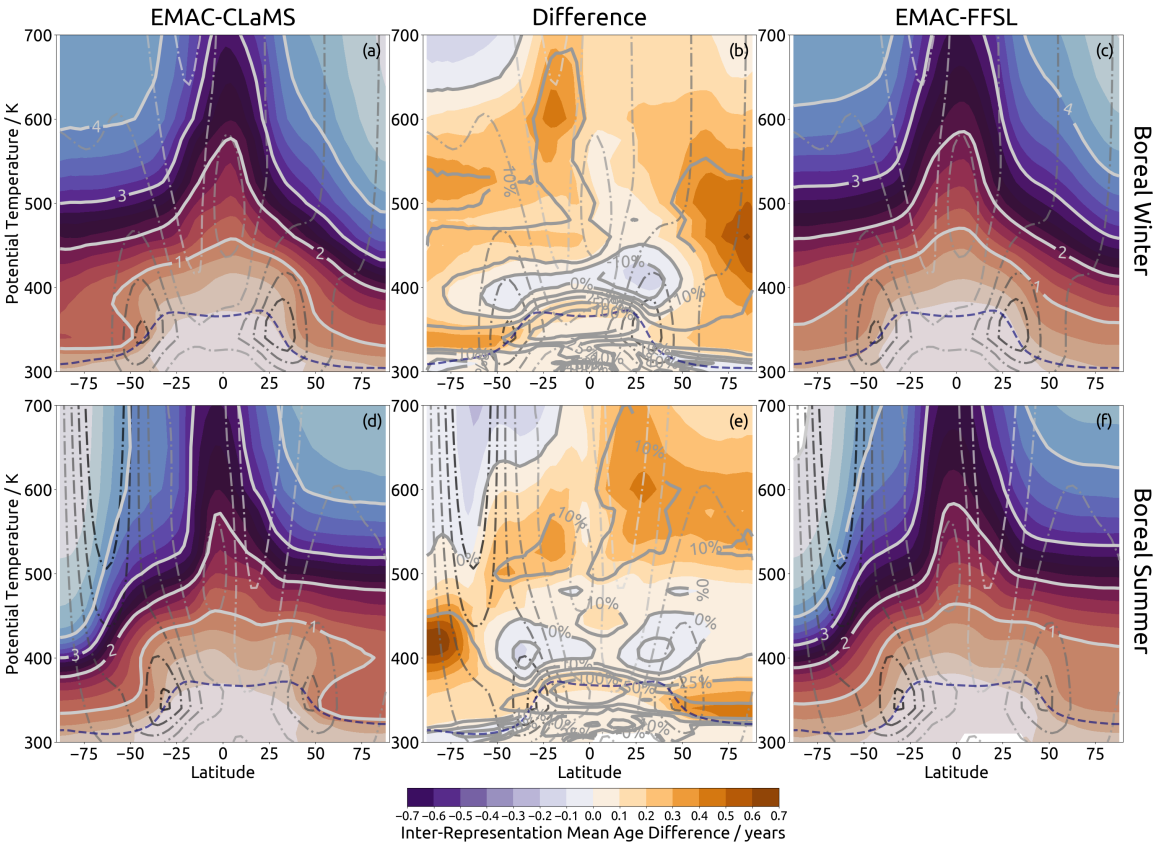

Figure 3.1.: Mean age of air computed from age spectra for EMAC-CLaMS (a, d) and EMAC-FFSL (c, f) and the difference between them (b, e) in boreal winter (mean of December, January, and February) (a, b, c) and boreal summer (mean of June, July, and August) (d, e, f). For the central figures, shading shows the absolute differences (in years) between the representations (EMAC-CLaMS minus EMAC-FFSL) and contours show percentage differences (with EMAC-FFSL as baseline). Otherwise, contours and shading show mean age (in years), with a shading interval of 0.25 years.

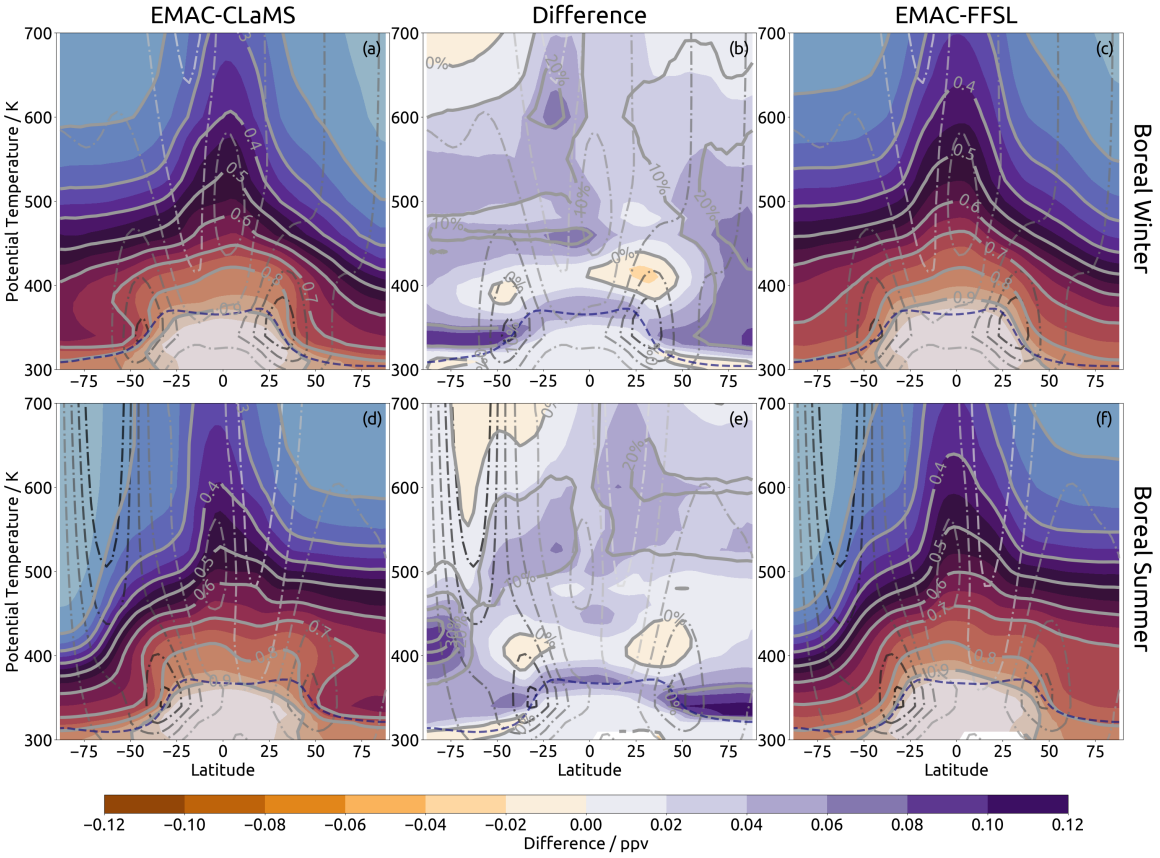

Figure 3.2.: Same as Figure 3.1 but the quantity examined is a "forward-tracer" of 2-year lifetime (see text for details), with the exception that the percentage differences show in panels b and e use EMAC-CLaMS as the baseline (i.e. 30% means that EMAC-FFSL results shows 30% more forward tracer than those of EMAC-CLaMS) (see Section 3.2.3 for details).

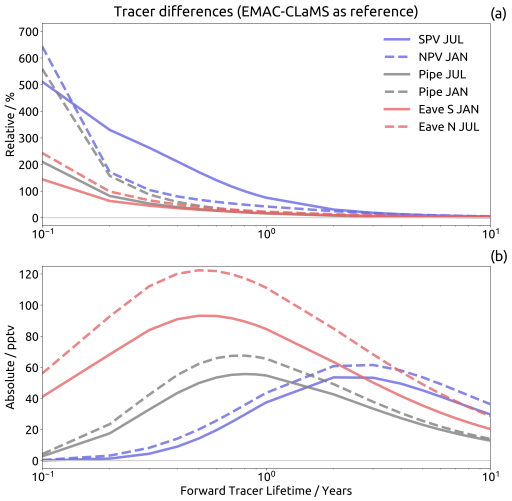

Figure 3.3.: Inter-representation difference (a: relative difference, EMAC-FFSL minus EMAC-CLaMS normalized by EMAC-CLaMS; b: absolute difference, EMAC-FFSL minus EMAC-CLaMS) in forward tracer mixing ratios in several regions during January ("JAN") and July ("JUL"), versus exponential decay lifetime of the tracer. Results are shown for the southern polar vortex ("SPV", 70-90° S, 450 K), northern polar vortex ("NPV", 70-90° S, 480 K), tropical pipe ("Pipe", 5° S–5° N, 500 K), and summertime eave locations ("Eave", 50°–75° north or south, 360 K).

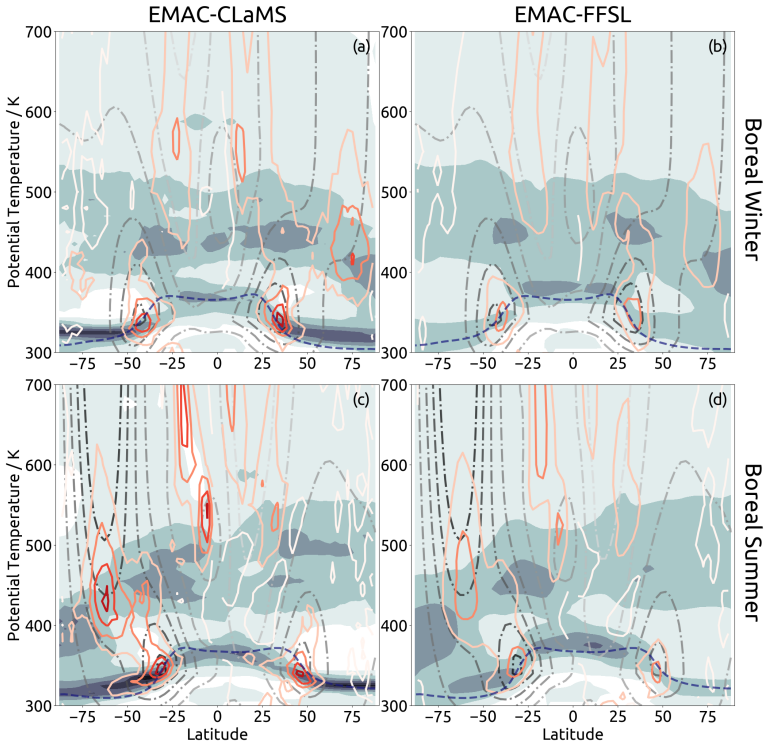

Figure 3.4.: Gradients of a 2-year lifetime forward tracer, from the tracer field calculated by the 10-year mean of representation age spectra. Shown are results from EMAC-CLaMS (a, c) and EMAC-FFSL (b, d) during January (a, b) and July (c, d). The vertical gradient is calculated with respect to potential temperature and shown in the grey shading while the horizontal gradient is calculated with respect to the absolute value of latitude and shown with the colored line contours. Plotted gradients do not have explicit units; the vertical (horizontal) gradient is normalized to the maximum vertical (horizontal) gradient found in all four panels. Darker (redder) shading (contours) correspond to the maximum value, while lighter (paler) shading (contours) correspond to the smallest values. The steps between shadings (contours) are fixed fractions for both the filled and line contours.

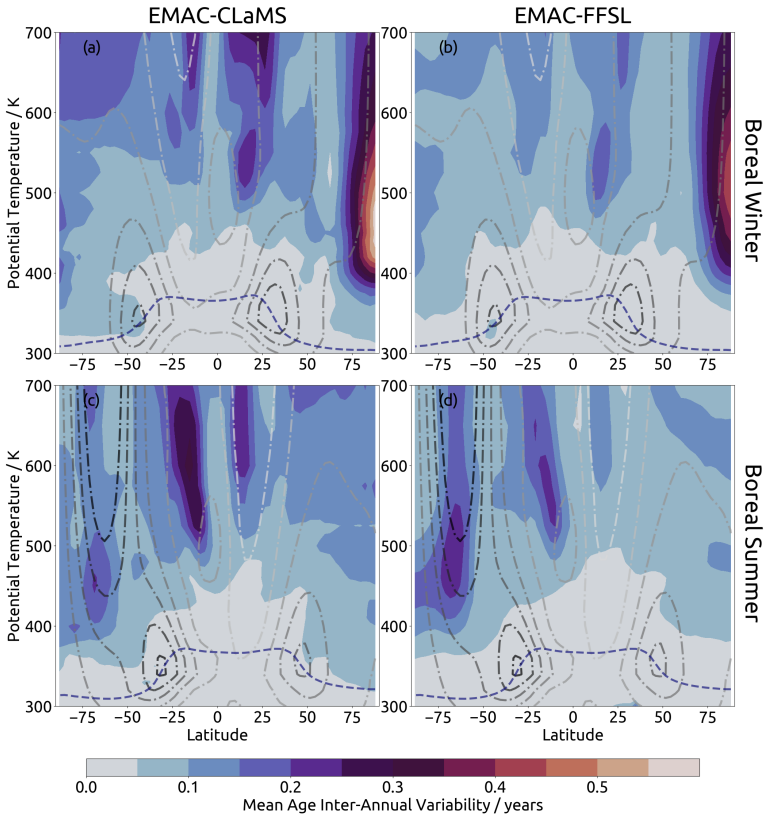

Figure 3.5.: Standard devation of spectra monthly-average mean age over the ten-year climatology from EMAC-CLaMS (a, c) and EMAC-FFSL (b, d) during boreal winter (a, b) and summer (c, d).

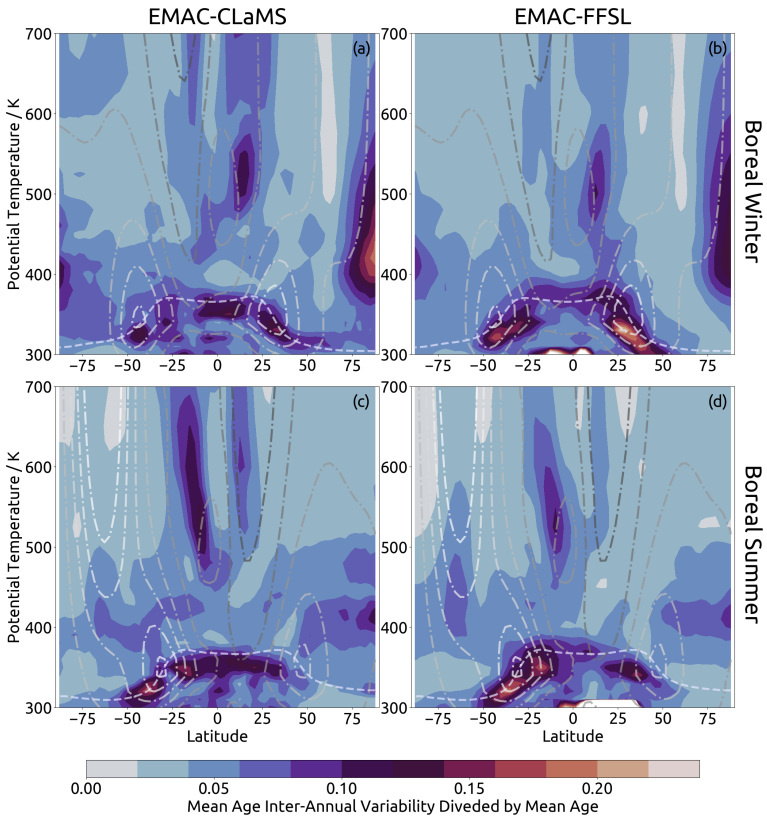

Figure 3.6.: Same as Figure 3.5, but the quantity shown is the standard deviation of spectra mean age scaled (divided) by the spectra mean age.

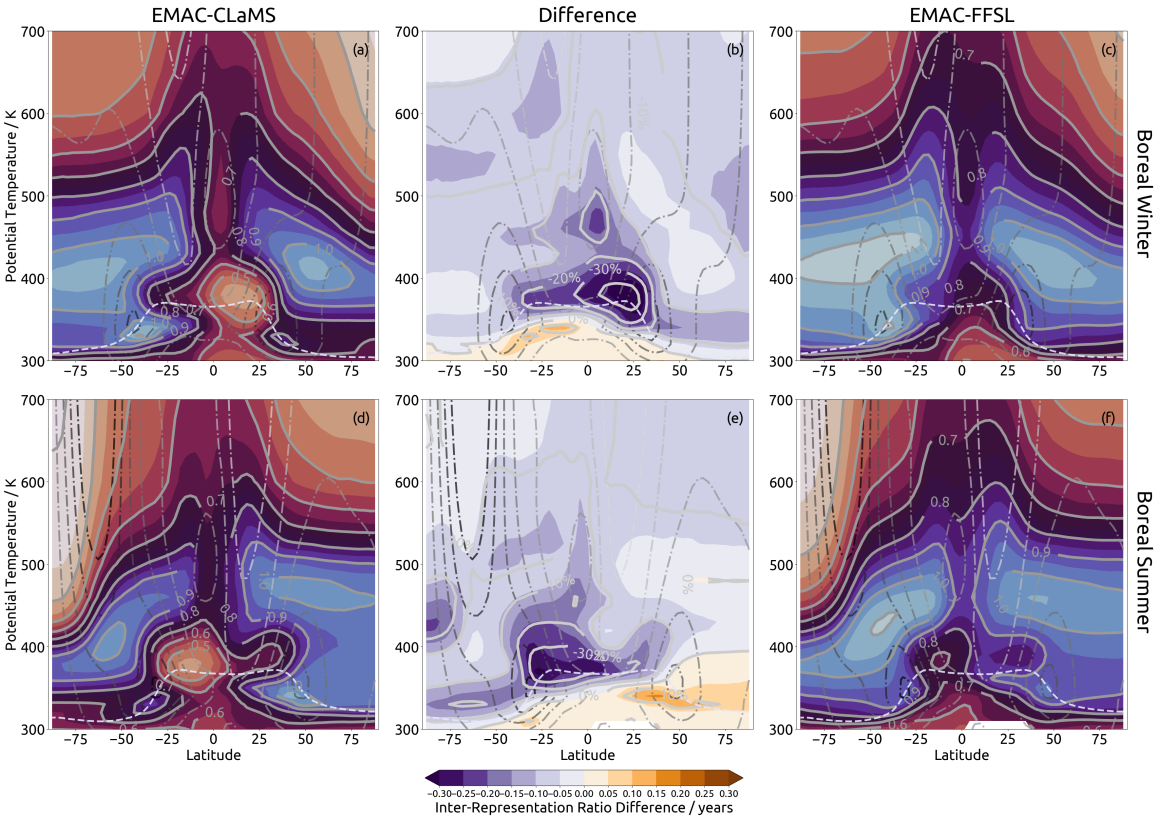

Figure 3.7.: Panels correspond to those of Figure 3.2, but the quantity shown in the age spectra ratio of moments (width divided by mean age, units of years).

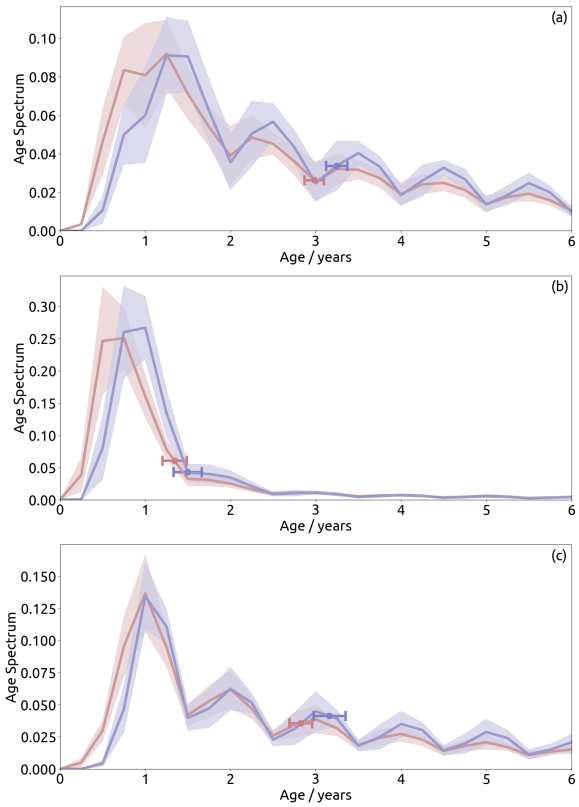

Figure 3.8.: Age spectra from the results of EMAC-FFSL (red) and EMAC-CLaMS (blue) at 500 K for (a) the southern mid-latitude stratosphere (40-60° S, July), (b) the tropical pipe (6° S–6° N, January), and (c) the northern mid-latitude stratosphere (40-60° N, January). Lines indicate multi-annual mean with shading showing annual variability. Dots indicate mean age of spectra, with surrounding bars showing annual variability. Variability for both quantities is computed as two standard deviations.

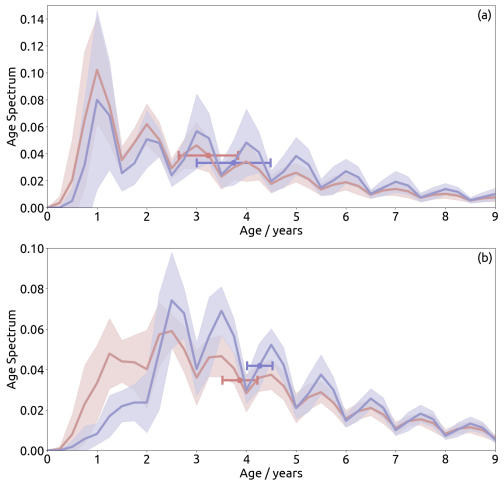

Figure 3.9.: Age spectra from EMAC-FFSL (red) and EMAC-CLaMS (blue) within (a) the northern polar vortex (480 K, 70–90° N, January). and (b) the southern polar vortex (90-70° S 450 K, July), Lines indicate multi-annual mean with shading showing annual variability. Dots indicate mean age of spectra, with surrounding bars showing annual variability. Variability for both quantities is computed as two standard deviations.

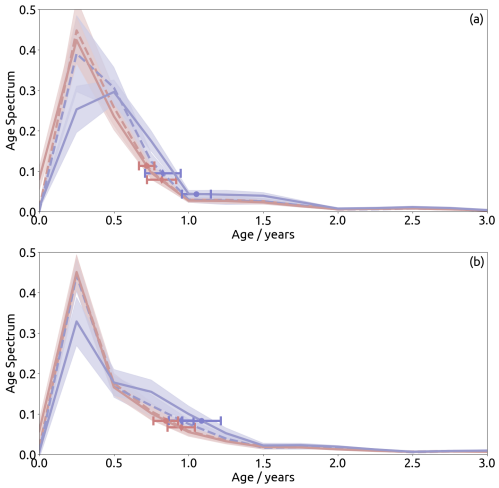

Figure 3.10.: Age spectra from the results of EMAC-FFSL (red) and EMAC-CLaMS (blue) within the summertime LMS regions of the eave structures at 360 K (sold lines) and 400 K (dashed lines) in (a) Northern hemisphere (55–75° N, July), and (b) Southern hemisphere (55–75° S, January).

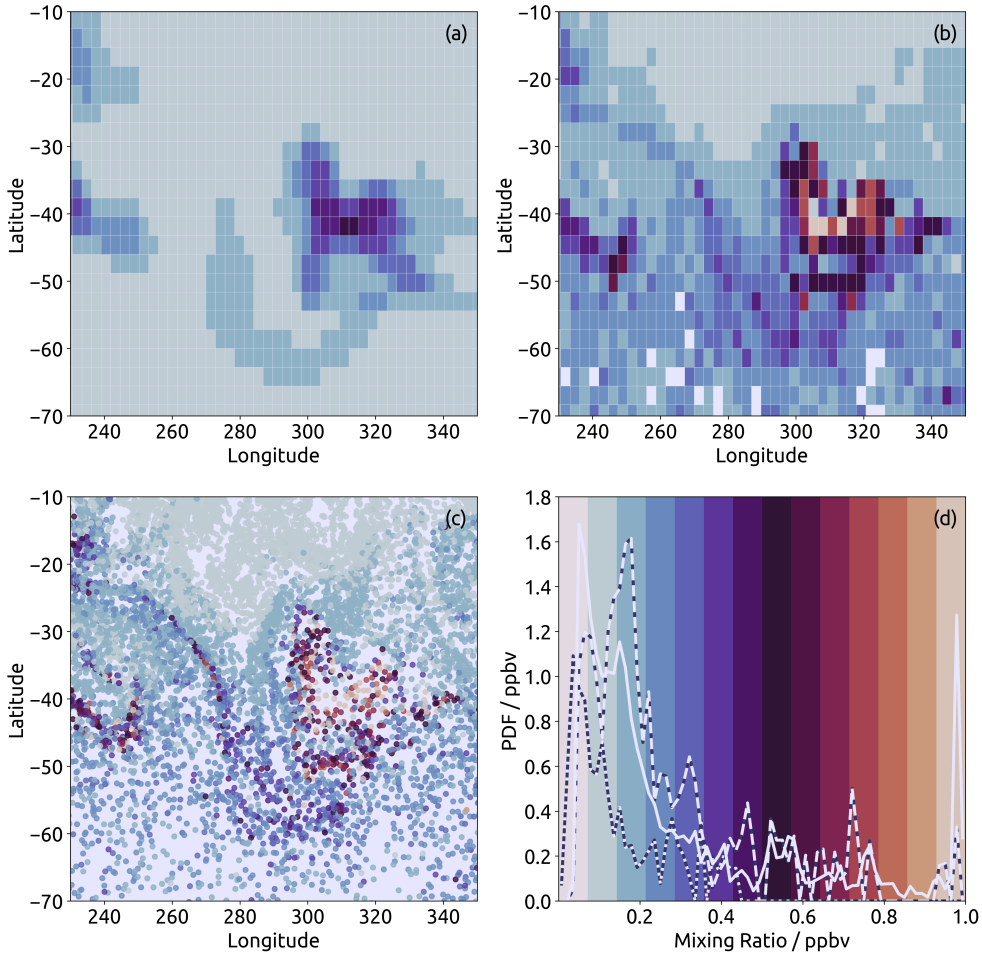

Figure 3.11.: Region from plume injection experiment showing results for a long-lived (365-day lifetime) tracer. Panel (a): EMAC-FFSL results on EMAC grid at model level 63 (approximately 100 hPa, level of plume injection). Panel (b): EMAC-CLaMS results gridded onto the EMAC model grid at the same level as the EMAC results. Panel (c): EMAC-CLaMS data for parcels within EMAC model level 63 in the unprocessed Lagrangian representation. Panel (d): histograms showing distributions of tracer mixing ratios within the shown region. The color map used in panels a-c corresponds to the background colors in panel d. Histograms are shown for panel a (short-dashed line), panel b (long-dashed line), and panel c (solid line). Histograms are computed using only data which is shown in the other three panels (i.e., within the shown region and within EMAC model level 63), and the histograms of gridded results are mass-weighted.

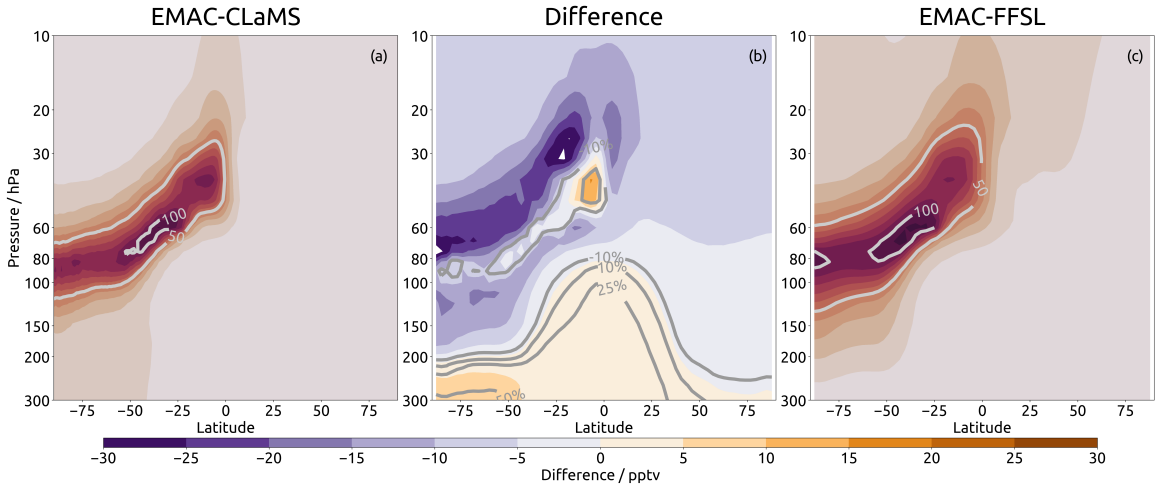

Figure 3.12.: Zonal mean tracer distribution from continuous mass injection in the stratosphere (30S, 100hPa) from EMAC-CLaMS (a) and EMAC-FFSL (c) results, contours showing tracer mixing ratios in pptv (emission value of 1 ppbv). Also show is the difference between the fields (b) with both absolute differences (shading) and percentage differences (contours, EMAC-CLaMS as reference). Results are shown for a 1-year lifetime tracer.

4. Radiative Effects of Stratospheric Water Vapor

Chapter 3 describes the effects of schemal differences on passive tracer transport. In that work, the CLaMS transport scheme was driven by the EMAC climate model, but the results of CLaMS transport had no feedback on the climate model results. In this chapter, work is described wherein CLaMS water vapor fields were used to drive EMAC radiation calculations. In principle, any radiatively-active chemical could be used in this investigation. Water has been chosen in this case due to the simplicity of the chemistry involved, which reduces the possible interference of differing chemistry models on the resulting water vapor fields.

4.1. Radiative Coupling

Section 3.2 describes the one-way coupling of EMAC and CLaMS, whereby CLaMS was made dependent on (driven by) EMAC dynamical fields while EMAC was independent of the state of CLaMS. EMAC-CLaMS also has the capacity for "full" coupling (i.e. feedback) of the CLaMS transport scheme into EMAC through fields of radiatively-active tracers (e.g., water, ozone). To achieve this, the following procedure is performed on each time step of the simulation for each radiatively-active tracer requested in the model set-up (so far, only water vapor).

During model set-up, an EMAC-FFSL grid level index is supplied by the user for which all higher EMAC-FFSL levels should be controlled by EMAC-CLaMS fields and all lower EMAC-FFSL levels should be controlled by EMAC-FFSL fields. This is depicted (in an idealized fashion) in Figure 4.1. In this case, the first and second layers are dominated by EMAC-FFSL, while the upper six layers are dominated by EMAC-CLaMS. That is, the tracer field used in the EMAC-FFSL radiation calculation in this lower region is precisely that of the EMAC-FFSL transport scheme without any direct effect of the EMAC-CLaMS transport scheme. Meanwhile, the parcel tracer values of EMAC-CLaMS parcels which are within an EMAC-FFSL lower-region grid cell are fixed to those of the respective EMAC-FFSL grid cell. In the higher region, the tracer field supplied to radiation is calculated from the EMAC-CLaMS tracer field.

The precise procedure for the upper-boundary calculation is as follows. First, the EMAC-FFSL grid cell boundaries in latitude, longitude, and pressure are used to determine which EMAC-FFSL grid cell contains each EMAC-CLaMS parcel. Second, for each EMAC-FFSL grid cell the average tracer value (for the tracer in question,

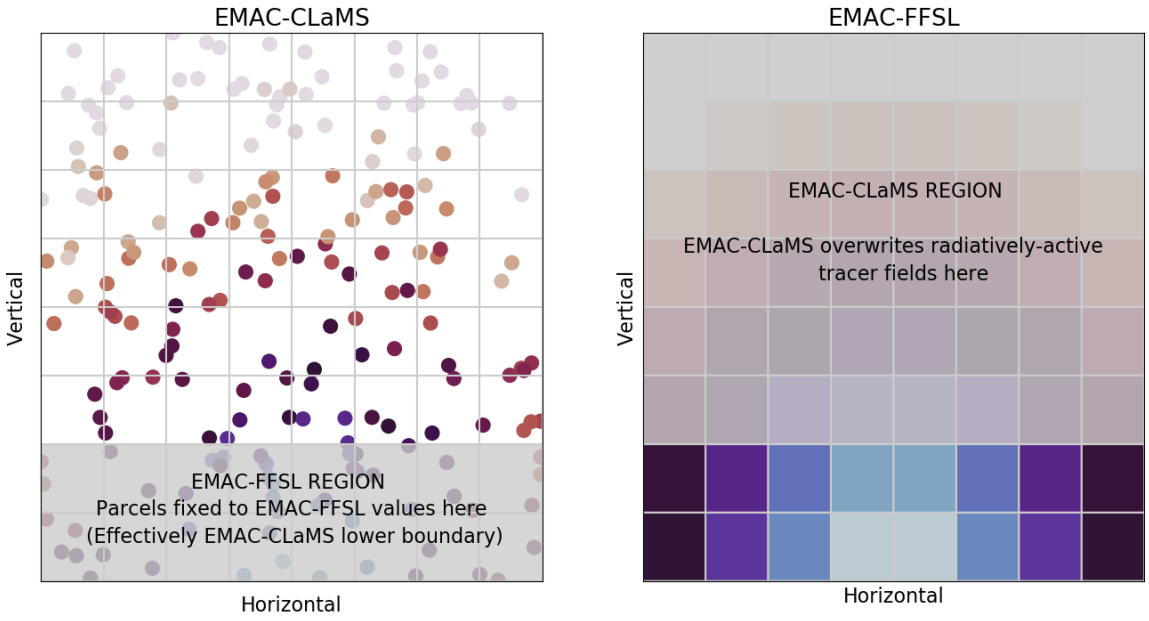

Figure 4.1.: Schematic showing the coupling relationship between the two transport schemes. The image on the left represents the EMAC-CLaMS transport scheme with a distribution of Lagrangian parcels each with some tracer value. The image on the right represents the EMAC-FFSL transport scheme with a distribution of tracer values in its Eulerian grid. The tracer values are indicated with the parcel/grid coloring. Within this schematic, these values and their distribution are arbitrary. Shaded regions indicate areas of coupling. That is, areas where a transport scheme's field is affected by or ignored in favor of the field of the other transport scheme.

be it water, ozone, or something else) from all the EMAC-CLaMS parcels contained in that grid cell was calculated. For all EMAC-FFSL grid cells containing at least one EMAC-CLaMS parcel, these average EMAC-CLaMS parcel tracer values were supplied to the EMAC-FFSL radiative calculation field (again, only for the higher region, as designated by the user during model set-up). For all EMAC-FFSL grid cells which are contained in the higher region but within which there are no EMAC-CLaMS parcels, the tracer value supplied to the radiation calculation was that of the EMAC-FFSL representation for that grid cell.

In the work that follows, EMAC-FFSL level 63 was chosen as the coupling boundary. This level corresponds to approximately 250 hPa.

4.2. Experiment Design

The experiments described in this chapter were designed to investigate the effect of transport scheme on the water vapor field and the effect of the chosen water vapor

field (i.e. coupled/EMAC-CLaMS or uncoupled/EMAC-FFSL) on EMAC radiative calculations. Two simulations were analyzed: an uncoupled simulation and a coupled simulation. In the coupled simulation, the EMAC-CLaMS water vapor distribution was used to drive the EMAC radiation calculation (as described in section 4.1). In the uncoupled simulation, the EMAC-FFSL water vapor distribution was used to drive the EMAC radiation calculation. Both simulations were calculated for 10 years beginning from the same model state, from which only the last year was used for analysis. The initial model state was calculated after a 10 year simulation without EMAC-CLaMS water vapor coupling.

All simulations (including the initial model state) were designed under the so-called quasi chemistry-transport model (QCTM) set-up of EMAC (Deckert et al., 2011). Under this set-up, the distributions of radiatively active chemicals (excluding water vapor) are not interactively calculated, but are rather prescribed from datasets. The datasets used are distributions from the ESCiMo simulations (Jöckel, Tost, et al., 2016), which are high-resolution EMAC simulations with fully-interactive chemistry encompassing a wide variety of chemicals, including all radiatively-active tracers used in this work. The ESCiMo simulation from which the radiatively-active chemical data was taken is the RC1-base-07 simulation. This simulation was chosen because it covers the same period (historical) and uses the same grid resolution (90 vertical layers with a middle atmosphere focus) as the present work.

In addition to water vapor, the only other radiatively-active tracer calculated in the present simulations was methane. This distribution was calculated due to the impact of this tracer on stratospheric water vapor (see Section 2.3.1). The calculation was performed separately in EMAC-FFSL and EMAC-CLaMS, without using an identical calculation method. This distribution was not used in the radiative calculation (instead the ESCiMo methane distribution was used) to remove potential discrepancies between the uncoupled and coupled model runs which might have otherwise arisen from differences in model dynamics. However, the differences in the methane oxidation calculation could contribute to the differences between EMAC-FFSL and EMAC-CLaMS water vapor fields, but this contribution is only likely to be significant in the deeper stratosphere.

4.3. Water Differences

4.3.1. Water Vapor Distribution Differences in Uncoupled Simulation

Figure 4.2 shows the water distributions from CLaMS and EMAC in the uncoupled simulation. The distributions (i.e. left and right panels) show general qualitative similarity: air becomes drier with decreasing pressure at all latitudes with the notable exception of the tropical water vapor minimum, which occurs around 85 hPa, consistent with the tropical tropopause level, in both representations. However, a notable qualitative difference is also apparent between the two representations at extratropi-

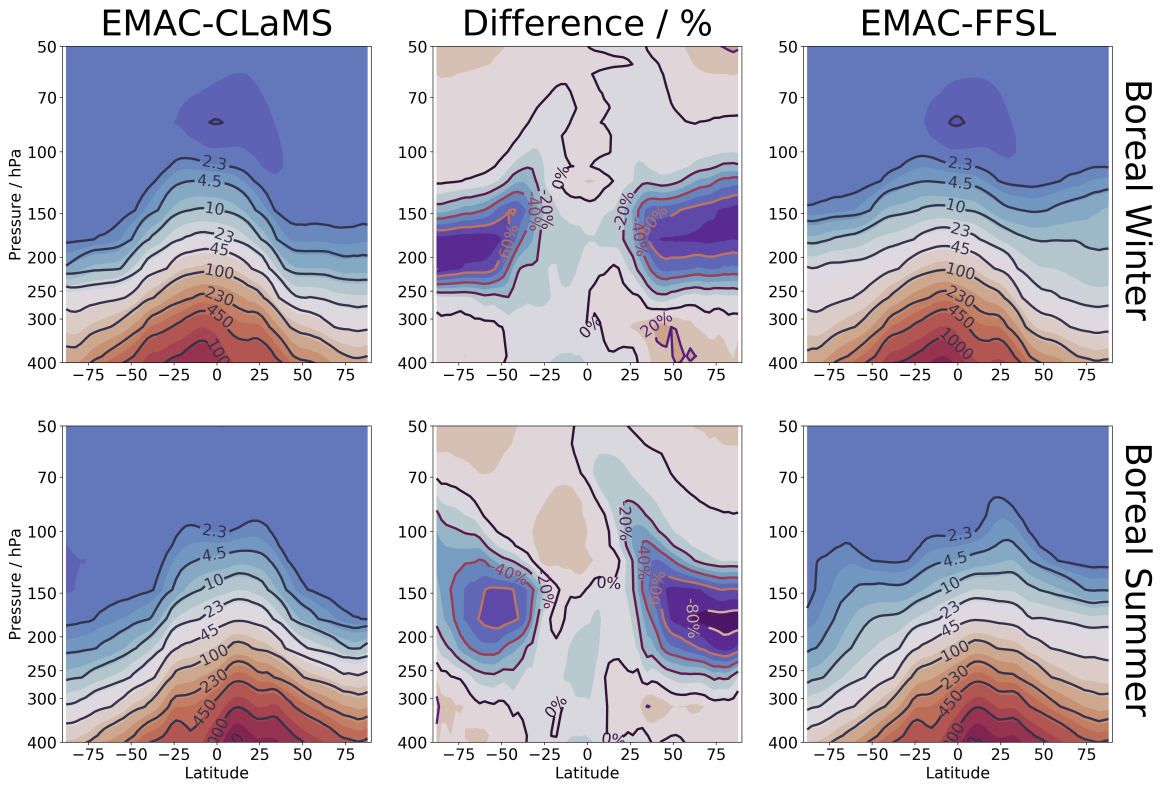

Figure 4.2.: Water vapor distributions for the final year of the uncoupled simulation (see section 4.2). Left: EMAC-CLaMS results. Right: EMAC-FFSL results. Middle: percentage difference (CLaMS minus FFSL divided by FFSL). Top: boreal winter (January). Bottom: boreal summer (July). On left and right, contours are in ppmv, while in the middle contours are in percent. In the middle panels, shading steps are 10%.

cal latitudes. In particular, for many water vapor contours, outside of the tropics the pressures at which these contours are found increase with increasing latitude, but this change is much sharper in EMAC-CLaMS than in EMAC-FFSL. In fact, in EMAC-FFSL some contours decrease in pressure with increasing latitude when the same contours are strictly increasing in pressure in EMAC-CLaMS. The clearest example of this is the 2.3 ppmv contour, which sometimes lofts with increasing latitude in the winter hemisphere for EMAC-FFSL, but is strictly descending in EMAC-CLaMS. Furthermore, boreal summer shows even more stark qualitative differences between the two transport representations, in that EMAC-FFSL shows a "peak" in the 2.3 and 4.5 ppmv contours around 25 N, and shows little to no descent in the 2.3 ppmv contour in the southern hemisphere until nearly the south pole. In fact, there is a considerable lofting of the 2.3 ppmv contour around 70 S in EMAC-FFSL.

These qualitative differences suggest that EMAC-FFSL shows either stronger upward, cross-tropopause transport of water in the extratropics or stronger isentropic

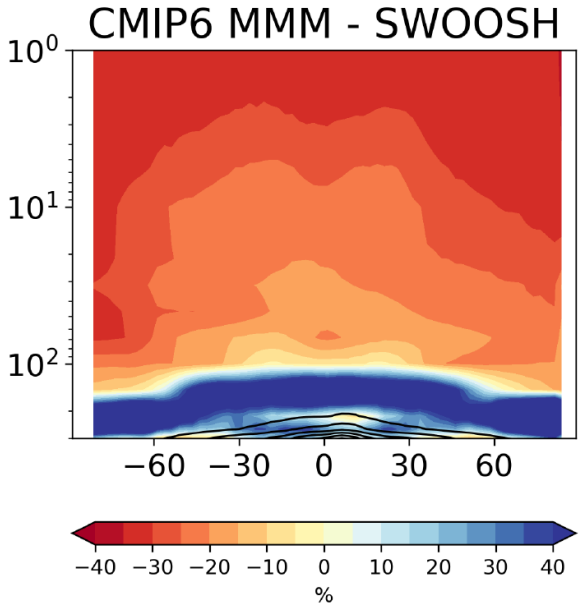

Figure 4.3.: Shown is the difference between the CMIP6 multiple model mean and observations from the SWOOSH dataset (CMIP6 minus SWOOSH). Cool colors indicate more water in CMIP6 than SWOOSH. From Keeble et al. (2020) (their Figure 13).

poleward transport from the TTL than EMAC-CLaMS.

The quantitative differences (Figure 4.2 center panels) magnify these qualitative extratropical differences. By far the greatest discrepancy is found in the extratropical lower stratosphere (between about 150 and 250 hPa). There, EMAC-CLaMS water vapor mixing ratios are less than 60% of the values found in EMAC-FFSL. The difference in a given hemisphere is greatest during local summer (i.e. 80% versus 70% in the northern hemisphere and 70% versus 60% in the southern hemisphere). These differences bear a striking similarity to the differences in stratosphere water vapor between CMIP6 models and observations found in the work of Keeble et al. (2020), seen in Figure 4.3. In that work, it was found that models, on average, had approximately twice as much water in the extratropical lower stratosphere, in comparison to observations.

Beyond the extratropical lower stratosphere, relatively minor numerical differences are found between the two representations. Of note are a small region around 350 hPa and 50 N where EMAC-CLaMS shows 20% greater water vapor than EMAC-FFSL. This difference is only due to a quirk in the differences of the transport scheme resolutions, in that the zonal-mean of EMAC-CLaMS data is produced by the average of all parcels zonally, for which the distribution of parcels may not be even across an entire latitude. This results in a difference in the calculated zonal-mean water value between EMAC-FFSL and EMAC-CLaMS when the distributions are in fact identical in the region (because the region is below the lower boundary set for EMAC-CLaMS

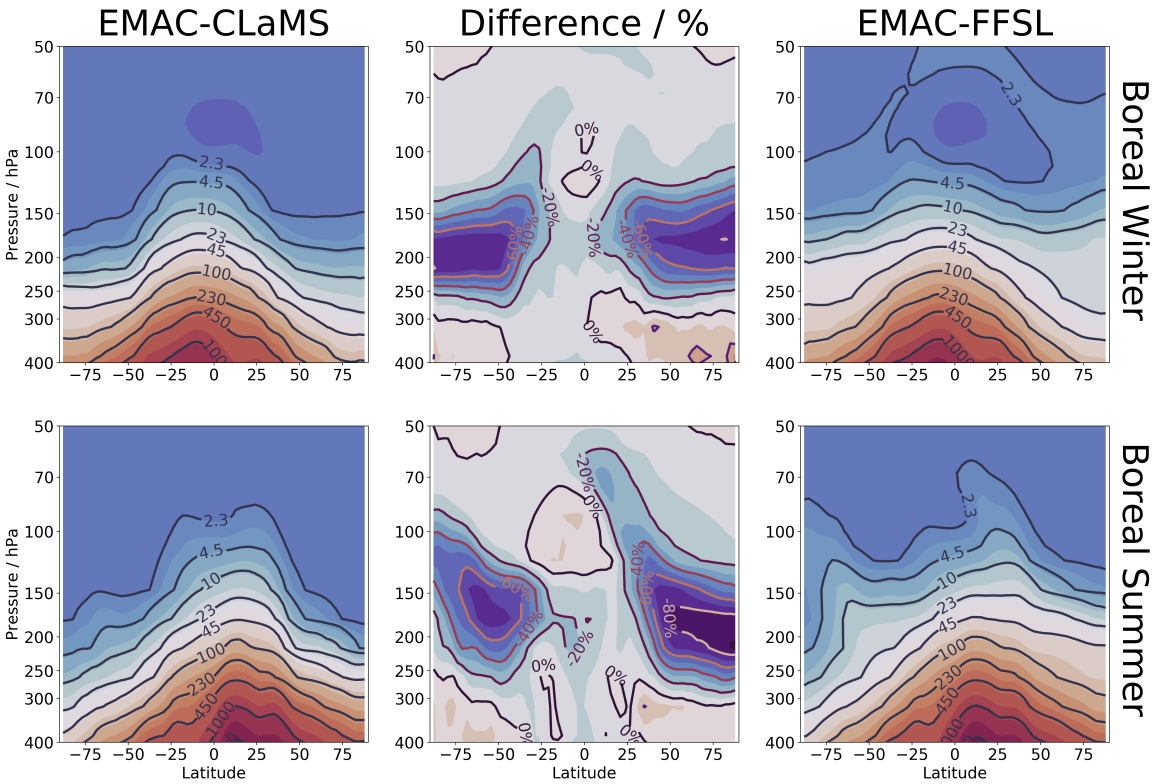

Figure 4.4.: Water vapor distributions for the final year of the coupled simulation (see section 4.2). Left: EMAC-CLaMS results. Right: EMAC-FFSL results. Middle: percentage difference (CLaMS minus FFSL divided by FFSL). Top: boreal winter (January). Bottom: boreal summer (July). On left and right, contours are in ppmv, while in the middle contours are in percent.

water vapor). Additionally, there appears to be a pattern in the differences around 25 N/S wherein the summer hemisphere shows a "tongue" of lower EMAC-CLaMS water vapor which reaches up towards 70 hPa. This result may not be significant under a statistical analysis, but may warrant further investigation.

The coupled simulation (Figure 4.4, left and right panels) shows slightly more water vapor than the uncoupled simulation (Figure 4.2, left and right panels). This is apparent both in the location of water vapor contours – which are slightly higher in the coupled simulation than in the uncoupled simulation – and in the minimum value of water vapor around 85 hPa in the tropics – where the coupled simulations show slightly more water vapor. These differences are consistent among both schemes and both seasons. The cause of this difference is not immediately clear, but is likely caused by slighty warmer tropical tropopause temperatures in the coupled simulation.

One notable consistency between the two simulations is found in the EMAC-FFSL boreal summer panels, wherein both the "peak" around 25 N for the 2.3 and 4.5

ppmv contours and the sudden dip in contours around 80 S (albeit for the coupled simulation in the 4.5 ppmv, whereas this is found in the 2.3 ppmv contour in the uncoupled simulation) are found. As the dynamics of the two models are likely to have significantly diverged over the 10 year model run, it seems likely that these features are climatological for EMAC-FFSL during boreal summer.

Examining the differences in the coupled simulation water vapor distributions (center panels, Figure 4.4), the general pattern of the uncoupled simulations is found: major differences show that EMAC-CLaMS has less than 60% of the water vapor mixing rations found in EMAC-FFSL in the extratropical lower stratosphere; a slight "tongue" of lower EMAC-CLaMS water vapor is found on the summer side of the tropics reaching up around 70 hPa; other differences are relatively minor. The only differences between the center panels of Figure 4.2 and Figure 4.4 is that the "background" (outside of regions of major difference) values are perhaps slightly closer to 0% in the coupled simulation compared to the uncoupled simulation, and that the extratropical lower stratosphere differences are slightly stronger in the coupled simulation compared to the uncoupled simulation. However, the cause of this difference between the coupled and uncoupled simulations is not readily apparent.

4.4. Temperature Differences

As water is of critical importance for the stratospheric radiative budget, the large differences in EMAC-CLaMS and EMAC-FFSL water vapor mixing ratios should have some effect on stratospheric temperatures. This effect is shown in Figure 4.5 (center panels), where it is clear that the uncoupled and coupled simulation temperature distributions are most different in the extratropical lower stratosphere. In this region, the coupled simulation is approximately 5 K warmer than the uncoupled simulation, and is in no case colder than the uncoupled simulation. Differences are largest in the northern hemisphere, reaching above 10 K in some locations, but this difference is most apparent during boreal summer, and less apparent during boreal winter. This corresponds to the schemal water vapor differences seen in Figures 4.2 and 4.4, where boreal summer shows stronger schemal differences in the north compared to the south, but boreal winter does not show such a strong hemispheric difference in the schemal discrepancy. The results of earlier work suggest that these differences in temperature are almost certain to have some significant effect on stratospheric dynamics (Maycock, Joshi, Shine, et al., 2014).

Other simulation temperature differences include warmer coupled simulation temperatures in the tropics above 100 hPa. The cause of this could be natural dynamical variability, but it may also be the case that the small inter-schemal water vapor differences seen in this region have significant effects on the radiative budget, owing to the long radiative timescales in this region (Hitchcock, Shepherd, and Yoden, 2010; T. Birner and Charlesworth, 2017).

Additionally, during boreal winter in the northern middle statosphere (northward of 50 N and between 50 and 100 hPa) there are considerably warmer temperatures

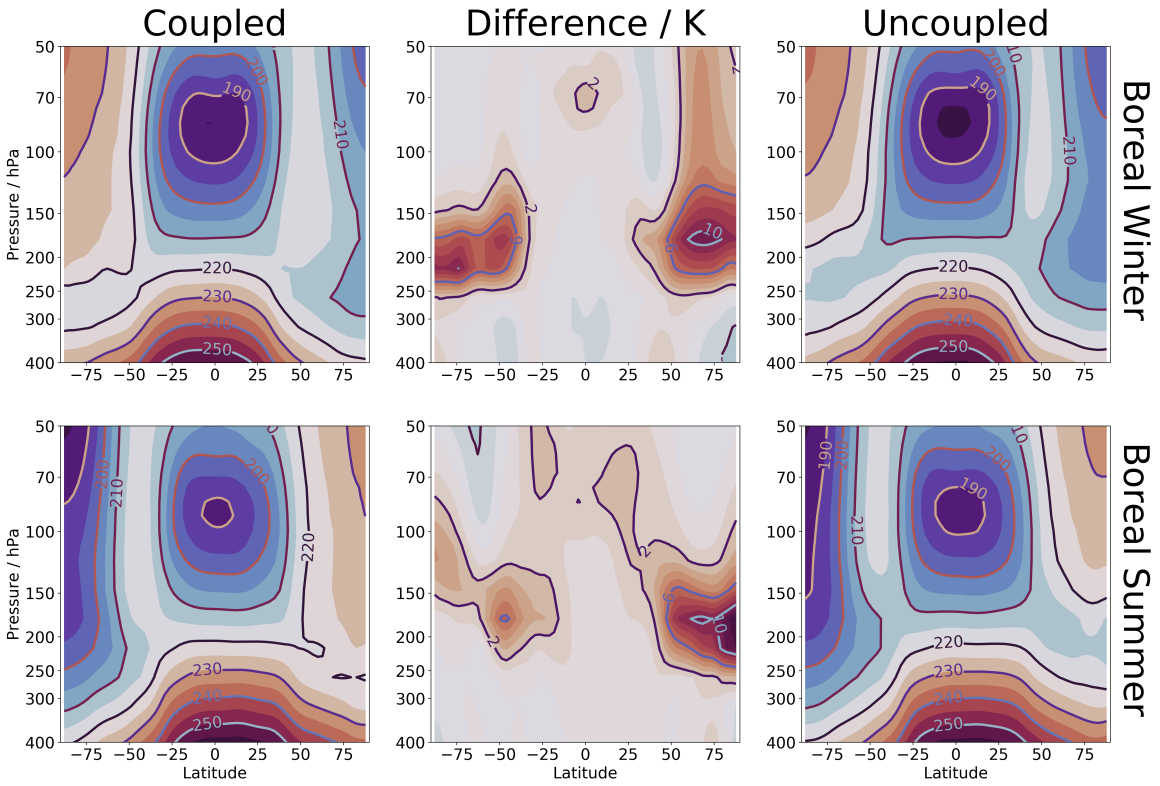

Figure 4.5.: EMAC temperature distributions for the final year of the simulations (see section 4.2). Left: coupled simulation. Right: uncoupled simulation. Middle: difference (coupled minus uncoupled). Top: boreal winter (January). Bottom: boreal summer (July). Contours are all in Kelvin. Shading steps are 5 K in the left and right panels and 1 K in the center panels.

(approximately 4 K). This occurs despite no apparent schemal differences in water vapor in this region, as far as is shown in Figures 4.2 and 4.4. Although certainty on the reason requires more investigation, the cause for this may be differences in EMAC-CLaMS and EMAC-FFSL water vapor in the higher atmosphere (above 50 hPa), where EMAC-CLaMS shows more water vapor (not shown), which could increase downwelling longwave radiation. This discrepancy (of a wetter upper stratosphere in EMAC-CLaMS compared to EMAC-FFSL) may have occurred due to the differences in handling the impact of methane on stratospheric water vapor in EMAC-FFSL and EMAC-CLaMS. Removing this discrepancy is likely to be technically achievable (by applying the EMAC-FFSL water tendency from this process to CLaMS parcels, per the EMAC-FFSL grid cells where they are present), but remains outside the scope of this work.

4.5. Recent Literature Context

The two transport schemes studied in this work showed the largest differences in stratospheric water vapor in the extratropical lowermost stratosphere (LMS). Stratospheric water vapor in this region has been a topic of much recent interest, with a focus on the radiative effects of the changes in the quantity due to climate change. The recent body of work on this topic begins with the study of Banerjee et al. (2019). Their work compared stratospheric water vapor among the CMIP5 models, which used a sudden quadrupling of carbon dioxide to estimate the effects of climate change. Effectively, such an experiment involves computing a control simulation where carbon dioxide is left at pre-industrial levels and comparing this to an "equilibrium" high carbon dioxide state. The experiments described in this chapter are not as comprehensive as those of Banerjee et al. (2019), and therefore might not be one-to-one comparable to studies using trends in carbon dioxide. Furthermore, the CMIP5 models are not chemistry-climate models, which means that some processes relevant for climate change in the stratosphere are not accounted for.

Banerjee et al. (2019) show increases in stratospheric water vapor (see Figure 4.6) which are global in almost all models. Of all the models shown, only eight show decreases or no change in water vapor in the southern polar region between 100 and 10 hPa, while all other models show increases in this region and all other regions show increases in water vapor in all models. The regions of increase include the LMS. In fact, the LMS contains the strongest increases[1] in a majority of the CMIP5 models, with only the CNRM-CM5, CNRM-CM5-2, CSIRO-Mk3-6-0, and IPSL-CM5A-MR models showing the largest increases in other regions. These four models also show massive (> 150%) increases in water vapor in the deeper stratosphere, which is a stark contrast from the other models. Furthermore, these four models also show heavy increases in the extratropical lower stratosphere, of about 80% or more. These are still not the least increases in this region of the other models, which show increases of at least 50%. This conclusively shows that drastic increases in extratropical lower stratospheric water vapor are a robust result of all CMIP5 models. Banerjee et al. (2019) also notes that the increases in stratospheric water vapor create a significant positive feedback on surface temperatures, which they found to be comparable to the surface albedo feedbacks and cloud feedbacks. This result echoes the work of several previous studies which discussed the significance of the stratospheric water vapor feedback (Solomon, K. Rosenlof, et al., 2010; Maycock, Shine, and Joshi, 2011; Dessler et al., 2013). Most significantly for the work presented in this chapter, Banerjee et al. (2019) also estimated that the changes in the extratropical lower stratosphere accounted for three fourths of the total radiative feedback.

Several studies have followed the work of Banerjee et al. (2019), For example, Xia, Y. Huang, and Hu (2020) studied the CMIP6 models, which also robustly showed increases in extratropical lower stratospheric water vapor. Furthermore, they noted that

[1] Figure 4.6 only shows percentage changes, but absolute increases are also largest in this region. This fact is not surprising, however, as water vapor mixing ratios are largest in this region, compared to the rest of the stratosphere.

the radiative feedback associated with stratospheric water vapor increases strengthened over the course of the simulation period. Y. Huang Y. W. and H. Huang (2020) found that the stratospheric water vapor feedback was insignificant due to its feedbacks on other processes, which they suggested were not accounted for by prior studies which relied on a fixed dynamical heating assumption (such as Banerjee et al. (2019)). Using the same model, Y. Wang and Y. Huang (2020) also found that the stratospheric water vapor radiative feedback was insignificant compared to other climate-change processes. Li and Newman (2020) used methods similar to those of Y. Huang Y. W. and H. Huang (2020) and found a significant stratospheric water vapor radiative feedback. Furthermore, this work found substantial impacts on stratospheric processes and phenomena which they associated with the stratospheric water vapor feedback, including the attribution of the feedback towards 30% of increases in tropical upward mass flux. A similar result was found by (Maycock, Joshi, P., et al., 2013), who isolated the effects of changing stratospheric water vapor from other climate effects by increasing stratospheric water vapor to the exclusion of any other changes. Li and Newman (2020) also found a significant contribution of the stratospheric water vapor feedback onto arctic amplification, which carries with it implications for northern hemispheric climate.

A wide variety of methods have been applied in these works, as well as a variety of models such as the intermediate complexity model of Solomon, K. Rosenlof, et al. (2010) to the coupled atmosphere-ocean CCM of Li and Newman (2020). While most of these models and methods have shown significant effects of the stratospheric water vapor radiative feedback on tropospheric climate – as well as on stratospheric dynamics – the recent works of Y. Wang and Y. Huang (2020) and Y. Huang Y. W. and H. Huang (2020) raise questions about these interpretations and the methods used to arrive at them. However, no clear consensus has yet been developed on the topic.

The results of the work presented in this chapter also point to another methodological question, namely that of the models used. More specifically, the work shown here demonstrates the possibility that model transport schemes have the potential to arrive at very different conclusions on extratropical lower stratospheric water vapor mixing ratios. As already discussed, Banerjee et al. (2019) has shown that the strongest stratospheric water vapor trends in CMIP5 models occur in the extratropical lower stratosphere, and has estimated that these trends cause about 75% of the surface effects of the stratospheric water vapor feedback. Furthermore, the work of Keeble et al. (2020) clearly indicates the model biases towards high water vapor mixing ratios in the extratropical lower stratosphere (see Figure 4.3) and in particular that these biases are of more than 40%[2]. The work shown here addresses some of these topics, showing that the semi-Lagrangian transport scheme of EMAC produces extratropical lower stratospheric water vapor which is approximately 100% larger (at a minimum, reaching a maximum of 500% larger) than that found in the Lagrangian

[2] Unfortunately this region is not focused on by Keeble et al. (2020), such that the exact magnitude of these differences remain unclear

model of EMAC-CLaMS.

Four factors are known to be the primary sources of stratospheric water vapor: (1) transport through the tropical tropopause; (2) transport through the subtropical tropopause; (3) extratropical overshooting convection; (4) *in situ* methane oxidation. Factor (1) does not cause the differences found between EMAC-CLaMS and EMAC-FFSL, as the schemal water vapor differences found above the tropical tropopause are near zero (in relative terms). Although methane oxidation is handled differently between EMAC-CLaMS and EMAC-FFSL, this factor is unlikely to affect the differences in the extratropical lower stratosphere, where the age spectra (see for example Figure 3.10) is heavily weighted towards younger air, which is therefore unlikely to have significant water vapor caused by the slow process of methane oxidation. Finally, the differences in age spectra in the extratropical lower stratosphere (again, see Figure 3.10) described in Chaper 3 suggest that differences in the effects of overshooting convection are less likely to be the cause of differences in transport timescales between the troposphere and the extratropical lower stratosphere. If this is true, then schemal differences in transport through the subtropical tropopause is likely to be the cause of the massive differences in extratropical lower stratospheric water vapor between EMAC-CLaMS and EMAC-FFSL. However, these results are based on the transport of tropically-emitted tracers, not water vapor, and therefore more study may be necessary to eliminate the possible effects of overshooting convection.

That being said, differences in transport across the subtropical jet – particularly of transport due to unwanted, unphysical numerical diffusion which is present in EMAC-FFSL and not present in EMAC-CLaMS – remain a likely cause of the water vapor differences in the extratropical lower stratosphere, for the transport schemes studied in this work. If the representation of the subtropical jet is the primary cause of these differences, this would have very significant implications for the study of the stratospheric water vapor feedback, as all of the models from previous studies which have been cited in this Chapter used transport schemes that were of a semi-Lagrangian nature (as in EMAC-FFSL) or are of a non-Lagrangian nature. This would raise the possibility that the water vapor balances in the extratropical lower stratosphere (which are critical to the study of the stratospheric water vapor feedback) are biased due to excessive transport of water vapor from the wet tropical troposphere to the dry extratropical stratosphere, and that climate change-related trends in LMS water vapor are biased as well.

4.6. Conclusions

The work of this chapter has demonstrated the differences between Lagrangian (EMAC-CLaMS) and Eulerian (EMAC-FFSL) transport on water vapor distributions in the stratosphere within a climate model (EMAC). The most important differences found were in the LMS, where EMAC-CLaMS showed between 60 and 90% less water vapor than EMAC-FFSL, which are likely to be caused by the absence and presence of unphysical numerical diffusion in EMAC-CLaMS and EMAC-FFSL, respectively.

These difference had corresponding radiative effects of up to 10 K in the LMS. Both of these results point to potential biases within contemporary climate models due to the choice of transport schemes, as models typically use Eulerian, not Lagrangian, transport schemes. Given that modern climate models use Eulerian (or semi-Lagrangian) transport schemes and are also heavily wet-biased in the LMS (see Banerjee et al. (2019)), it seems likely that the adoption of Lagrangian transport schemes would present an improvement in the LMS water vapor balance within models.

One uncertainty involved in this work is the possible effects due to differing methane oxidation schemes in EMAC-CLaMS and EMAC-FFSL. This uncertainty could, however, be removed for other chemicals (and indeed for water as well) by applying the same chemistry models towards CLaMS and EMAC chemistry. The models in question are JVAL (Sander et al., 2014) – a photodissociation rate model – and MECCA – a comprehensive chemistry model. Unifying the chemistry calculations of CLaMS and EMAC would make the coupling of arbitrary radiatively-active species feasible, including those that are strongly affected by chemistry. The most relevant of these would certainly be ozone. Another interesting direction of this work is the investigation of aerosols, such as those emitted by volcanic eruptions.

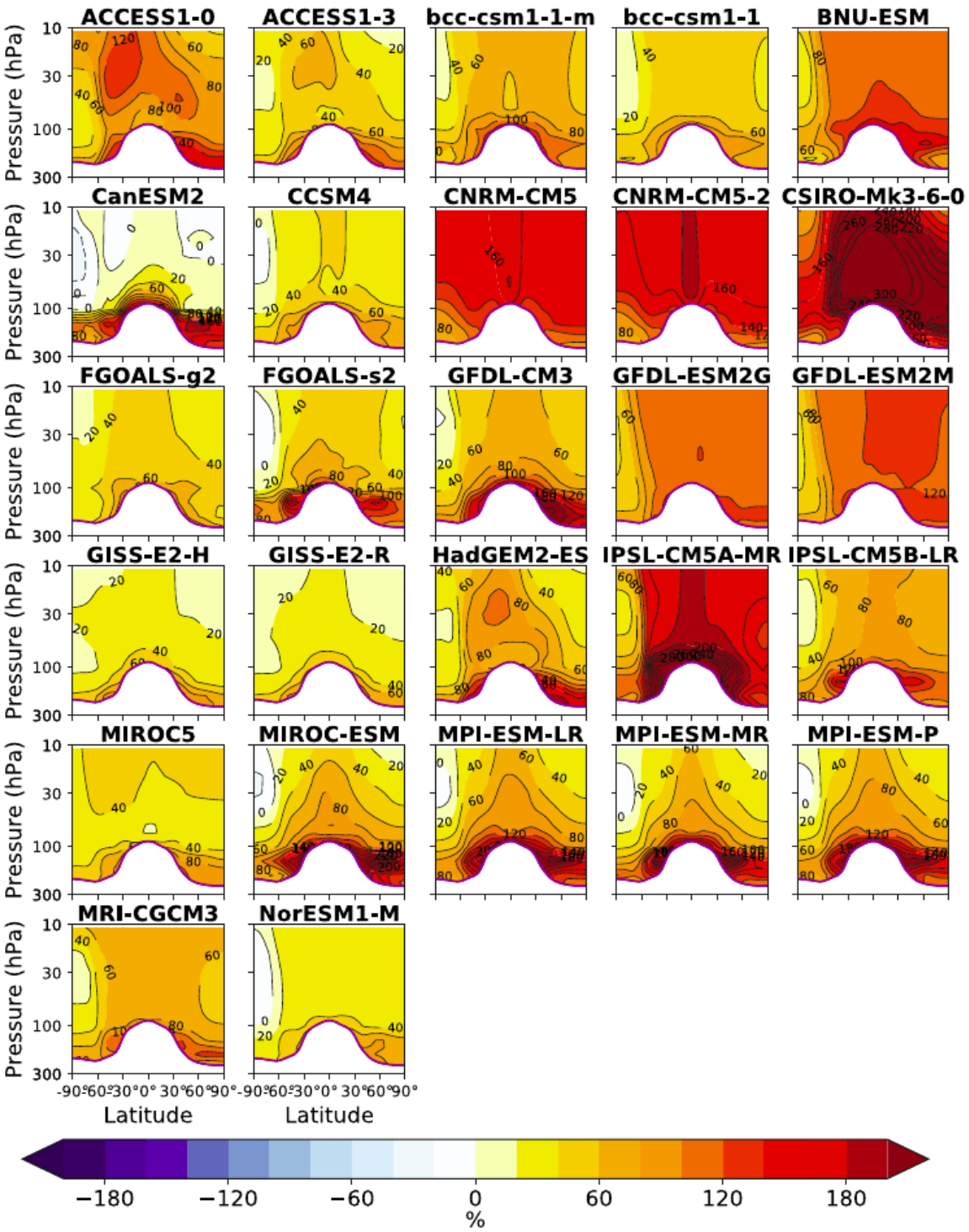

Fig. 2 The relative (%) response of SWV to 4 × CO_2 in individual CMIP5 models. Values below the PORT piControl tropopause are masked out

Figure 4.6.: Relative changes in water vapor between late and early periods in CMIP6 models. From Banerjee et al. (2019) (their Figure 2).

5. Quantifying Brewer-Dobson Circulation Variability from Ozone Observations

As the Brewer-Dobson circulation (BDC) has wide ranging effects on the distribution of tracers in the stratosphere, understanding the evolution of the circulation's strength is of considerable interest. As mentioned previously, a robust result of climate model simulations is the acceleration of the BDC (Hardiman, Butchart, and Calvo, 2013). However, observation-based studies searching for signs of this acceleration have been non-conclusive. In this chapter, work is described wherein a novel quantity is investigated as a proxy for transformed Eulerian mean upwelling. The proxy assumption is found to be effective at one location in the stratosphere, supported by both theoretical understanding and model assessment.

5.1. Current Knowledge

The stratospheric circulation plays a first-order role in the distribution of ozone and water throughout the region, which has attendant effects on surface climate and habitability as well as feedbacks on stratospheric dynamics. The representation of the circulation in models and reanalyses is structurally consistent, but contains considerable disagreement in terms of mean strength and variability (Hardiman, Butchart, and Calvo, 2013). Due to the feedback-dominated processes of the stratosphere, small biases in processes within one model (or reanalysis) may result in circulation differences which are greater than might be expected. Building knowledge on the stratospheric circulation through models alone thereby presents a significant challenge, while the impossibility of directly measuring the circulation precludes straightforward comparison of theory and models with observations. Furthermore, the body of scientific literature on the topic of BDC trends is not in agreement; models robustly predict an acceleration of the circulation, as does theoretical understanding, while reanalyses and observational studies based on age of air do not show the clear trends predicted by the first two sources (e.g., Stiller, Fierli, et al., 2017). These conflicts motivate the importance of a more direct estimate of BDC strength based on observations.

One simple way of measuring the strength of the circulation is through tropical stratospheric upwelling. This measure constrains the total strength of the circulation, as the circulation only lofts within the tropics and in all other regions is dominated by downwelling or horizontal transport. A number of studies have been performed

which have attempted to constrain this quantity through various methods. The earliest example of this, to the knowledge of the author, is Brewer (1949), who wrote that tropical vertical velocities would "prove to be... about 50 m/day", or approximately 0.6 mm/sec. Using diabatic heating rates, Murgatroyd and Singleton (1961) estimated similar values (see their Figure 2). Fu, Hu, and Yang (2007) applied more sophisticated calculations to estimate the vertical profile of upwelling. Their results show a minimum in upwelling near 20 km, above which upwelling (as measured in geometric units) increases. Randel, F. Wu, Oltmans, et al. (2004) and Randel, F. Wu, Vömel, et al. (2006) found values similar to those of Brewer (1949) by examining the correlation of the stratospheric water vapor tape recorder signal and cold point tropopause temperature. Glanville and T. Birner (2017) applied two methods to calculate tropical vertical velocities from water vapor observations, even including estimations of the seasonal cycle of upwelling.

Mean age of air has been used as a qualitative estimation of circulation trends by Stiller, Fierli, et al. (2017), the results of which show more nuanced changes in the stratospheric circulation than the simple acceleration suggested by model simulations. Engel, Bönisch, et al., 2017 showed trends in mean age of air gathered by balloon-borne observations, showing statistically-insignificant positive trends (indicating a slower circulation), but these measurements were only gathered in the northern hemisphere. However, recent work has shown that some uncertainties in their calculation could mean that the observations are not inconsistent with a strengthening circulation when taking ranges of uncertainty into account (Fritsch et al., 2020). Linz et al. (2017) showed that the tropical-extratropical mean age of air difference could be used to estimate the strength of the stratospheric circulation. However, the calculation of mean age of air is difficult, requiring observations of long-lived tracers (such as CFC's), for which only short timeseries of observations exist. Furthermore, despite the long chemical lifetimes of the used tracers, this calculation is complicated by the need to account for losses that still occur. These calculations rest upon knowing the lifetimes of these tracers, which is still a topic of research (Ray et al., 2017).

At present, the only data sources which provide some time-resolved (not seasonal-resolved) estimation of tropical residual circulation upwelling are reanalyses. However, Abalos, Legras, Ploeger, et al. (2015) and Ploeger, Legras, et al. (2019) found inconsistent trends over decadal periods among these sources, although longer periods (i.e. multiple decades) showed greater consistency among reanalysis trends. Furthermore, although the values provided by reanalyses have high resolution and show the qualitative structure of the stratospheric circulation (including sub-annual variability) which are expected from other estimations, the reliability of these results is not clear due to the inherent opacity of reanalysis calculation methods. That is, reanalyses quantities are calculated by a combination of observation data assimilation and cost-function minimization, which leaves no clear logical pathway between observations and output. This precludes many methods of uncertainty estimation, leaving users to simply accept the data as is without being able to quantify the related reliability.

No method has been applied towards ascertaining a time-dependent circulation strength in a more direct way than reanalyses. However, some studies have noted

changes in ozone which might be indicative of circulation changes. An early example is Randel, Park, et al. (2007), who noted that lower stratospheric ozone trends are consistent with an accelerating circulation. Ball et al. (2018) found similar results, but dismissed the possibility of an accelerating circulation accounting for the trends, while the results of their work were followed by a number of studies suggesting dynamical variability plays a role in creating the trends they found. None of these studies, however, provided a time-resolved calculation of circulation strength, which would be a useful tool for a variety of topics of considerable research interest. The work presented in this chapter introduces a novel quantity, termed *effective ozone upwelling*, which is shown to be a valid proxy for TEM upwelling, within a certain region (southern tropics at 70 hPa) and context (upwelling anomalies and not absolute values).

5.2. Effective Upwelling

The novel quantity introduced in this work, termed effective ozone (EO) upwelling, is defined as

$$\overline{\omega}^*_{eff} = \frac{\overline{S} - \overline{\partial_t \chi_{O_3}}}{\overline{\partial_p \chi_{O_3}}}, \tag{5.1}$$

where S is the photochemical production rate of ozone ($2J_2\chi_{O_2}$).

EO upwelling has the following relationship to TEM upwelling

$$\overline{\omega}^*_{eff} = \overline{\omega}^* - \frac{S_{\mathrm{TROP}} - L + \mathrm{M} - \overline{v}^* \partial_\phi \chi_{O_3}}{\partial_p \chi_{O_3}}, \tag{5.2}$$

where L is the chemical loss rate of ozone and S_{TROP} is the "tropospheric" production rate of ozone (i.e. ozone production which is not due to S in Equation 5.1). Therefore, $\overline{\omega}^*_{eff}$ and $\overline{\omega}^*$ should be equal in regions with weak horizontal ozone transport, mixing, and loss, and little "tropospheric" ozone production.

In the tropics, oxygen photolysis becomes the dominant form of ozone production in the stratosphere, while ozone loss rates are small compared to dynamical ozone loss below approximately 25 km (Garcia and Solomon, 1985). Thereby, the chemical components of the ozone balance equation approximate to S in this region (i.e. only the stratospheric source of ozone). Furthermore, mixing processes near 70 hPa have been shown to be weak near this region compared to advection (Abalos, Randel, Kinnison, and Serrano, 2013), and are even weaker in the southern tropics than in the northern tropics (Stolarski et al., 2014). Therefore, from a theoretical basis, if EO upwelling might be used as a proxy for TEM upwelling, the region with the best conditions for this is the southern tropics near 70 hPa. Conveniently, the upwelling velocities in this region are frequently used to assess the strength of BDC trends in modeling studies. This work therefore focuses on upwelling near 70 hPa in the southern half of the tropics (20° S to the equator). All calculations have been performed for this location, unless otherwise noted.

5.3. Validity of Proxy Assumption

We turn now to model results, whereby the validity of the proxy assumption can be quantitatively assessed. The model results used for this assessment are from the ESCiMo project (Jöckel, Tost, et al., 2016), and specifically the RC1-base-07 simulation is used, which is a historical calculation with high vertical resolution (particularly in the stratosphere). This simulation uses the same resolution as the model runs employed in Chapters 3 and 4, and is also the same simulation from which fields of radiatively-active tracers are used for driving EMAC in the simulations described in Chapter 4.

It was found that EO upwelling did not have a long-term mean near that of TEM upwelling (shown in Figure 5.2). This is likely due to the absence of mixing terms, as chemical terms beyond the single reaction assumed (destruction and troposphere-like production reactions) were found to have a miniscule (less than 1%) quantitative effect (not shown). However, anomalies from the long-term mean for both EO and TEM upwelling were found to be comparable quantities (shown in Figure 5.1). The total (not deseasonalized) time series shows a correlation between EO and TEM upwelling of 0.871, with a linear fit of 0.724. In the deseasonalized series, after applying a three-month running average, the corresponding correlation is 0.751 and the linear fit is nearly 1. Without a three-month running mean (not shown) correlation is only 0.616 (although the linear fit is still strong at 0.958), due to monthly variations in upwelling that are not reflected in the ozone timeseries. These results show that, within the ESCiMo simulation examined, EO upwelling is an effective proxy for TEM upwelling, in the context of seasonal cycles and 3-month mean deseasonalized variability. The strong correlations between TEM and EO upwelling suggest that long-term trends should be similar between the two quantities. In confirmation of this, the timeseries of TEM upwelling had a trend of 0.0071 mm/s/decade while that of EO upwelling was 0.0077 mm/s/decade.

A second form of EO upwelling was also calculated (not shown). In this second form, production rates were not accounted for. In the seasonal cycle, the correlation coefficient between this second form and TEM upwelling was 0.816, but the linear fit was 1.47 times that of a perfect fit. For 3-month-average deseasonalized upwelling, this correlation was 0.35 and the fit was 0.70, rendering this method unfit for analysis. It is therefore necessary that production rates be included in the calculation of EO upwelling.

EO upwelling was also calculated with two types of input data: (1) meridionally-resolved ozone and production rates; (2) tropically-averaged ozone and production rates. The validation results shown in Figure 5.1 are for the first type. However, results calculated for the second type showed differences in correlation coefficients on the order of 0.001 and differences in fits with TEM upwelling of less than 2%. In this work, EO upwelling for observational results is produced with a type-1 calculation. That is, production rates are calculated for ozone profile series at different latitudes and EO upwelling is calculated as a meridionally-resolved quantity, after which a tropical mean is calculated.

5.4. Upwelling Seasonal Cycle

Figure 5.3 shows a comparison of the seasonal cycle of EO upwelling calculated from SHADOZ and BASIC data with that of TEM upwelling from ESCiMo and four reanalysis products: ERA5, ERAi, MERRA2, and JRA55. Although all sources agree on the structure of the upwelling seasonal cycle, the amplitude of the BASIC and SHADOZ EO upwelling cycle is considerably stronger than that of ESCiMo, ERA5, and ERAi. This difference is approximately a factor of two, based on the peak-to-trough amplitude of the cycles. Additionally, BASIC EO upwelling shows an even stronger cycle than SHADOZ, by about 30%. The SWOOSH EO upwelling seasonal cycle (not shown for ease of reading) is nearly the same as that of BASIC. JRA55 TEM upwelling, however, has nearly the same seasonal amplitude as the EO upwelling of BASIC, and shows a very similar pattern overall. MERRA2, meanwhile, has a much stronger TEM upwelling seasonal cycle than any TEM or EO upwelling timeseries.

5.5. Timeseries

The upper panels of Figure 5.3 also show timeseries of EO upwelling derived from all three ozone datasets (SHADOZ, SWOOSH, and BASIC). General qualitative agreement between the timeseries is clear from the full (i.e. not deseasonalized) timeseries, although SHADOZ shows a more nuanced seasonal peak than either SWOOSH or BASIC. This is also evident in the seasonal cycle, as discussed in Section 5.4. In the deseasonalized timeseries, many features of variability seem to be similar between the datasets, for example the increases in upwelling around 1998, 2009, and 2016. These peaks correspond to the El Niño winters, corresponding to the findings of previous studies which have suggested the role of ENSO in modulating the stratospheric circulation (Calvo et al., 2010; Diallo, Konopka, et al., 2019, e.g.).

Trends were calculated from the BASIC dataset. BASIC had a positive (acceleration) trend of 0.038 mm/s/decade, which is similar to the non-seasonal variability (standard deviation) of the timeseries, of 0.043 mm/s. SWOOSH had a positive (acceleration) trend of 0.046 mm/s/decade, which is similar to the non-seasonal variability (standard deviation) of the timeseries, of 0.063 mm/s. SHADOZ showed a weak negative (deceleration) trend of -0.007 mm/s/decade, which is an order of magnitude smaller than the non-seasonal variability (standard deviation), of the timeseries of 0.070.

The trend from SHADOZ is certainly insignificant. However, those from BASIC and SWOOSH are much larger than might be expected from model results, which suggest trends of roughly 2% per decade. The BASIC and SWOOSH trends would then suggest – assuming 0.5 mm/s as the baseline upwelling – a percentage trend of 10% per decade, which is much faster than expected from models. Taking on a straightforward statistical test, we can say that none of the dataset trends are significant as they are all smaller than their respective standard deviations. Applying

	SHADOZ	BASIC	SWOOSH	ERA5	ERAi	JRA55	MERRA2
SHADOZ	1.00	0.34	0.18	0.34	0.31	0.22	0.16
BASIC	0.34	1.00	0.86	0.23	0.29	0.39	0.20
SWOOSH	0.18	0.86	1.00	0.27	0.24	0.31	-0.06
ERA5	0.34	0.23	0.27	1.00	0.64	0.46	0.16
ERAI	0.31	0.29	0.24	0.64	1.00	0.49	0.28
JRA55	0.22	0.39	0.31	0.46	0.49	1.00	0.33
MERRA2	0.16	0.20	-0.06	0.16	0.28	0.33	1.00

Table 5.1.: Pearson correlation coefficients among EO upwelling derived from ozone datasets and TEM upwelling from reanalyses. Data used is three-month-average deseasonalized upwelling.

more comprehensive statistical methods to establish the significance of these trends should be a priority for future work on this topic.

5.6. Correlations with Reanalyses

Beyond the described EO upwelling data, the only other timeseries of upwelling are provided by reanalyses. Here, the EO upwelling data derived from each ozone dataset is compared to TEM upwelling obtained from four modern reanalyses (ERA5, ERAi, JRA55, MERRA2). This data is summarized in Table 5.1. We note here that the correlations shown are for three-month-average deseasonalized upwelling, rather than upwelling including a seasonal cycle, to focus on long-term variability.

The strongest correlation found is between the ERA-interim (ERAi) and ERA5 reanalyses TEM upwelling, at 0.64. This is not surprising, as ERA5 is the direct successor of ERAi. JRA55 TEM upwelling is also (relatively) well correlated with ERAi and ERA5, at 0.49 and 0.46, respectively. However, MERRA2 upwelling does not correlate strongly with those of any other reanalyses, the best such correlation being 0.33 with JRA55 upwelling. Among observation datasets, SWOOSH and BASIC EO upwelling are highly correlated at 0.86. This is likely to be the case due to the similarity of the underlying ozone data, as both datasets use a combination of satellite observations. In fact, SWOOSH and BASIC are nearly identical in the late period (not shown). However, neither BASIC nor SWOOSH is well correlated with SHADOZ upwelling.

Correlations between EO upwelling and TEM upwelling from reanalyses are also not very strong, the highest being the 0.39 correlation between BASIC and JRA55. Even among the weak correlations, no EO upwelling timeseries shows consisently stronger correlations among reanalysis TEM upwelling than the other EO upwelling datasets. However, all EO upwelling datasets show their weakest correlation with MERRA2 TEM upwelling. This provides another example of a study showing MERRA2 as an outlier among other reanalysis products with regards to stratospheric tropical upwelling (e.g., Ploeger, Konopka, et al., 2012; Ploeger, Legras, et al., 2019; Laube et al.,

2020). Furthermore, the rather inconclusive correlations between EO upwelling and reanalysis TEM upwelling provide no support for the use of any one ozone dataset in the calculation of EO upwelling. Although SHADOZ data is highly resolved in the vertical and associated with less observational uncertainty than satellite-based observations, the limited horizontal resolution of SHADOZ presents a potential weakness in its use as a source of global ozone data, for the purpose of EO upwelling calculations.

5.7. Limitations of the Method

Differences between EO upwelling derived from datasets of satellite (BASIC and SWOOSH) and radiosonde (SHADOZ) ozone observations are apparent in the results shown in Sections 5.4, 5.5, and 5.6. One major difference between these datasets (radiosonde versus satellite) seems likely to cause some of the difference between their results, beyond the method of observation. This difference is the horizontal resolution of the observation method. That is, radiosonde data is obtained at locations which are fixed over the observation time period while satellite data is obtained at locations which vary over the observation time period. Therefore, although radiosonde data may have stronger vertical resolution, the fact that the horizontal resolution is so limited (compared to satellite data) may hinder the use of this data for the estimation of global-mean EO upwelling anomalies, for which a more global representation may be necessary. However, the comparatively limited vertical resolution of satellite data may also be a hindrance to calculation of the vertical gradient, which is necessary for the calculation of EO upwelling. Furthermore, the assessment of trends in the EO upwelling series may require a substantially longer ozone timeseries than is presently available, owing to the high natural variability of BDC upwelling. At present, only about thirty-five years of data are available, which may not be sufficient for estimating trends. However, a statistical estimate of this is, at present outside, of the scope of this work.

5.8. Validity at other levels

As discussed in Section 5.3, EO upwelling is not a reliable estimator of the absolute value of TEM upwelling. However, it was found that the anomalies of TEM and EO upwelling were similar under some conditions, namely limited to the southern half of the tropics and 70 hPa. Furthermore, three-month-averages of deseasonalized upwelling were applied, reducing the effects of short-term changes in upwelling which were not reflected in the EO upwelling timeseries. The validity of this was addressed in Section 5.3, based on results shown in Figure 5.1, where it was shown that the correlation of deseasonalized EO and TEM upwelling was 0.75 and the linear fit between the two was 0.98, in the context of ESCiMo model results. These quantities are shown in Figure 5.4, along with the same quantities at other levels.

These results show that the EO-TEM upwelling correlation is above 0.7 in a region

between 150 and 30 hPa. This suggests that EO upwelling could be an effective proxy for TEM upwelling within this region for the purposes of identifying qualitative variability in TEM upwelling. To apply EO upwelling as a quantitative proxy, linear fits must also be near 1[1]. Between 70 and 30 hPa, this is the case, as linear fits in this region are above 0.9. Therefore, the region between 70 and 30 hPa is the region where an EO-TEM upwelling proxy assumption is most robust and practical. Although the linear fit is far from 1 in the region around 100 hPa, the high correlation coefficient indicates that there could be potential application of EO upwelling as a qualitative proxy for TEM upwelling at this location. Lastly, we note that the likely reason for the weak correlations above 30 hPa is that chemical odd-oxygen destruction rates become similar to the loss rates due to transport at these altitudes (Garcia and Solomon, 1985) (see also Figure 2.8).

5.9. Application of SHADOZ data

Observations from the SHADOZ dataset (Witte et al., 2017) are used in this work. Data from nine SHADOZ sites have been compiled to create a timeseries of the zonal-mean tropical ozone profile. For each site, all data available from 1998 to 2018 have been included. The sites, the latitudes of the sites, and the first and last measurements used in the sites are shown in Table 5.2.

Site Location	Latitude	First Date	Last Date
San Cristobal, Ecuador	0.9 S	2000-01-06	2008-10-23
Nairobi, Kenya	1.3 S	1998-01-07	2018-12-19
Malindi, Kenya	3.0 S	1999-03-06	2006-01-04
Natal, Brazil	5.4 S	1998-01-05	2018-12-11
Watukosek, Java	7.6 S	1998-01-07	2013-10-30
Pago Pago, American Samoa	14.4 S	1998-01-02	2018-12-19
Suva, Fiji	18.1 S	1998-01-05	2018-12-30
La Reunion Island, France	21.1 S	1998-01-06	2017-12-18
Irene, South Africa	25.9 S	1998-11-11	2018-12-19

Table 5.2.: SHADOZ sites used in this study.

Ascension Island, although at 8 S and therefore inside of the region of interest, was excluded due to a sharp change in ozone which was of a much greater magnitude than any found in any other site at any time.

[1] A fit below 1 indicates that EO upwelling is less variable than TEM upwelling, while a fit above 1 indicates that EO upwelling is more variable than TEM upwelling.

5.10. Calculation of Photolysis Rates

Ozone photochemical production rates are calculated by

$$S = 2\chi_{O_2} J_{O_2}, \tag{5.3}$$

where J_{O_2} – the rate of photolysis of diatomic oxygen – is calculated as

$$J_{O_2}(z) = \int_{\lambda_1}^{\lambda_2} \Phi(\lambda')\sigma(\lambda')T(\lambda', z)d\lambda', \tag{5.4}$$

where Φ and σ are the quantum yield and cross-section of diatomic oxygen, respectively, λ' is wavelength, z is the vertical coordinate, and T is the spectrally- and vertically-dependent transmission function. In this work, the transmission function was calculated using *uvspec*, a radiative transfer calculation tool from the libRadTran package. *uvspec* is recognized as one of the most robust available tools for the calculation of photolysis rates, and has been used as the reference tool for the creation and validation of a variety of photolysis rate parameterizations. Although calculations with *uvspec* have relatively high computational costs, the limited number of calculations needed in this work means that the use of *uvspec* was feasible.

The radiative transfer calculations in the context of this work depend on overhead ozone and diatomic oxygen number densities as well as the cross-sections of those species. Therefore, in addition to the necessary ozone mixing ratio data, temperatures and pressures need to also be provided. Two of the ozone datasets used in this work – BASIC and SWOOSH – do not provide associated temperature data but do contain pressure information. The final ozone dataset used in this work – SHADOZ – provides complete pressure data for each ozonesonde profile, but often does not have complete temperature data. Temperature data from the ERA-Interim reanalysis dataset was used to fill in the missing data in all three datasets. The sensitivity of the calculation to the temperature dataset used was tested by using temperature data from two other reanalyses (MERRA-2 and JRA-55), but this sensitivity was found to be negligible, as the production rates calculated from BASIC ozone data using each temperature dataset varied by less than 1% of the seasonal cycle amplitude.

For the SHADOZ dataset, it was also necessary to fill in missing ozone data above levels for which SHADOZ did not provide ozone data. This missing data was obtained from the BASIC dataset, but, likewise, the sensitivity of the choice of overhead-ozone data was tested by using ERA-Interim data in place of that of BASIC and was found to be negligible (less than 1% variation in comparison to seasonal cycle amplitude). The spectral boundaries of the calculation were fixed to 190.5 and 220.5 nm, including the Schumann-Runge bands (190-204 nm) and part of the Herzberg continuum (204-240 nm). Including lower and higher wavelengths was found to increase computation times significantly and was not found to provide significant contributions to the overall photolysis rate (i.e. greater than 1% of calculated total photolysis rate). These regions were therefore excluded. The daily-average photolysis rate was obtained by

Month	Mean (ppbv/day)	Average Error (%)
Jan	4.24	5.13
Feb	4.42	5.41
Mar	3.92	8.30
Apr	2.50	8.75
May	1.71	11.57
Jun	1.26	14.01
Jul	1.33	17.74
Aug	2.06	10.27
Sep	2.97	7.38
Oct	3.78	6.84
Nov	3.90	4.89
Dec	3.86	4.51

Table 5.3.: SHADOZ production rate climatology. Monthly time-mean site-mean production rates (ppbv/day) and the monthly time-mean average error associated with using the time-mean production rate data compared to the time-resolved production rate data.

performing the radiative transfer calculation for solar zenith angles corresponding to 11 different timesteps, each one hour apart. The sensitivity of the calculation to the number of calculated timesteps was assessed, using a number of timesteps up to 600, and 11 timesteps was found to be sufficient. The cross-section data for the calculation corresponds to the recommendations of JPL. Finally, diatomic oxygen mixing ratios were assumed to be 0.21 for all calculations.

5.11. Simple Calculation

The method described in this chapter can be easily applied to other ozone datasets. However, photochemical production rates were calculated for each month of each dataset, which is a non-trivial calculation. In comparison, the remaining terms of EO upwelling can be calculated trivially from any ozone dataset. We have also estimated that a seasonal climatology of photochemical production rates would suffice for preliminary estimations of EO upwelling. We provide here one such seasonal climatology (in Table 5.3), which readers are encouraged to apply to other datasets. This climatology was calculated from the SHADOZ dataset, while the climatologies for other datasets are not provided as the differences between each climatology are small (certainly smaller than the differences between a climatology and a photochemical production rate timeseries).

5.12. Discussion

This chapter has introduced a novel quantity – EO upwelling – and investigated the utility of this quantity as a proxy for TEM upwelling. The proxy assumption was found to be supported by both theory and a comparison of both upwelling quantities using EMAC model data, in context of upwelling anomalies (and 3-month average anomalies in the context of deseasonalized timeseries). This presents an advancement in the estimation of the stratospheric circulation from observations, as no previous work has presented a method for producing timeseries of circulation velocities or strengths from observational data.

EO upwelling calculated from each dataset was in general agreement in terms of seasonal cycle but even in this case small differences were apparent between the two satellite-observation datasets (BASIC and SWOOSH) and SHADOZ, the only radiosonde database used. More considerable differences between the satellite and radiosonde datasets were apparent in the deseasonalized timeseries, as the former showed positive (acceleration) trends while the latter showed a very weak negative trend. Although no rigorous statistical analysis of these trends has been performed in this work, it was noted that the satellite trends were similar to (above 66% of) their respective standard deviations, while the SHADOZ trend was much smaller than (10% of) its standard deviation. The trends found from the satellite timeseries were roughly 0.05 mm/s/decade, which would correspond roughly to a 10-20% increase in upwelling per decade. This is much stronger than the trend expected from model results, which is approximately 2-3% per decade. However, the EO upwelling trends are very likely influenced by multi-annual and decadal variability which could make them larger than the true long-term trend. The application of longer datasets to the calculation of EO upwelling would be a significant boon in this regard, as the ozone datasets used in this work may not be long enough to calculate robust trends in upwelling, which is a quantity known from prior studies to be highly variable compared to the trends expected from it (Hardiman, P. Lin, et al., 2017).

The trend results presented here are the first of their kind; no other method, presented to date, has been used to quantitatively estimate stratospheric upwelling trends from observations. The results of this work show, at least, upwelling trends from a new observation-based dataset which are not contradictory with the acceleration of tropical upwelling seen in model data but also do not provide clear support of the model-based finding. The dataset which shows the most dissimilarity to this process is that derived from SHADOZ, the timeseries of which is also about 40% shorter than those of BASIC or SWOOSH.

The proxy assumption validation performed in Section 5.3 used model ozone and production rate data with the full model resolution. This presents a point of future work for understanding EO upwelling, as the observational datasets used in the calculation of the quantity have a coarser resolution than model data, both in space and time. The reliability of this method would therefore benefit from an extension of the model results application towards including the effects of reduced (compared to the model) resolution. More precisely, model data could be sampled in a pseudo-

observational way, for example by using weekly columns at selected, fixed grid cells to mimic the observational sampling of radiosonde measurements. Another method could be applied towards mimicking satellite measurements, although the best method for this is less clear. The information provided by these pseudo-observational validation methods would provide greater certainty of the reliability of the EO-TEM proxy assumption towards observational applications. Finally, the reliability of this method would also benefit from replication of the proxy assumption validation using data from other models.

The application of EO upwelling as a proxy for TEM upwelling may be useful at levels other than 70 hPa, in particular between 70 hPa and 30 hPa. EO upwelling might also perform well as a qualitative proxy for TEM upwelling in the region around 100 hPa. Quantities similar to EO upwelling could also be calculated using other chemicals in the stratosphere. Candidate species for these applications should have some location where; (1) their chemistry is simple; (2) mixing is weak; (3) their vertical transport is stronger than their horizontal transport, under a priori estimation; (4) the vertical gradient of the species is large. The reason for condition (1) is ease of calculation, while condition (2) is necessary to limit the effect of mixing in the resultant upwelling velocities. Condition (3) would be helpful to ensure that horizontal transport is also a small factor in the resultant upwelling velocities. Although condition (4) is related to condition (3), this is of separate – and strong – importance to the derivation of effective upwelling from any species, as weak vertical gradients would be more susceptible to observational error. Given the breadth of chemicals measured by modern satellite observations, the application of other species towards effective upwelling calculations should be pursued. The author suggests investigation of N_2O, CH_4, and CO in particular.

5.13. Conclusions

The work of this chapter has introduced EO upwelling, a novel measure of tropical stratospheric upwelling, and has shown that this quantity can be an effective proxy for anomalies of TEM upwelling, when examined near 70 hPa in the southern tropics. EO upwelling (calculated from three datasets) was found to have a seasonal cycle which was similar to that of TEM upwelling from reanalyses. Futhermore, timeseries of EO upwelling show prominent signals during El Niño winters, as expected from prior work on the effect of ENSO on the stratospheric circulation (e.g., Diallo, Konopka, et al., 2019). Trends in EO upwelling were found to differ between the datasets used, with radiosonde (SHADOZ) measurements showing near-zero trends while satellite (SWOOSH and BASIC) measurements showed positive but insignificant trends.

A myriad of options are available for future work using EO upwelling. For example, some statistical methods could be applied to provide other estimates of trends or to quantify the impact of ENSO, the QBO, or other forcings on stratospheric upwelling. EO upwelling could also be calculated at other altitudes, giving vertically-resolved upwelling information. The differences between using satellite and radiosonde datasets

in calculating EO upwelling should also be investigated, as differences in resolution may lead to biases in the resulting upwelling timeseries. Finally, similar effective upwelling quantities could be calculated from observations of other chemicals.

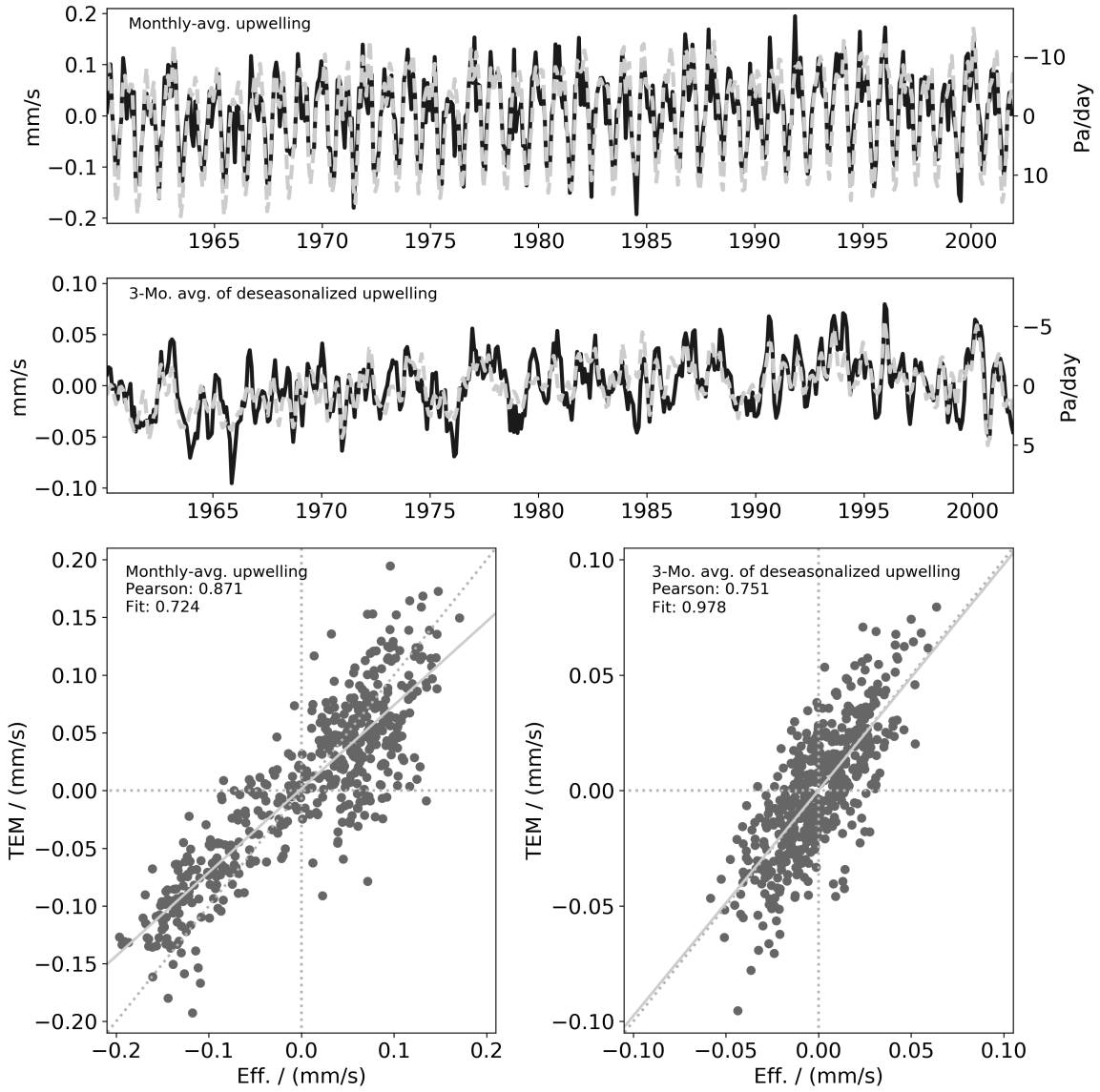

Figure 5.1.: Comparison of EO and TEM upwelling anomalies from the ESCiMo RC1-Base-07 simulation (see text for details). Top and middle panels show timeseries with TEM as black solid and EO as grey dashed lines, respectively. Bottom panels show scatter plots comparing TEM and EO upwelling with Pearson correlation coefficient and linear fit of data. Middle and bottom-right panels show 3-month-average of deseasonalized upwelling while top and bottom-left panels show monthly-average data including seasonal cycle.

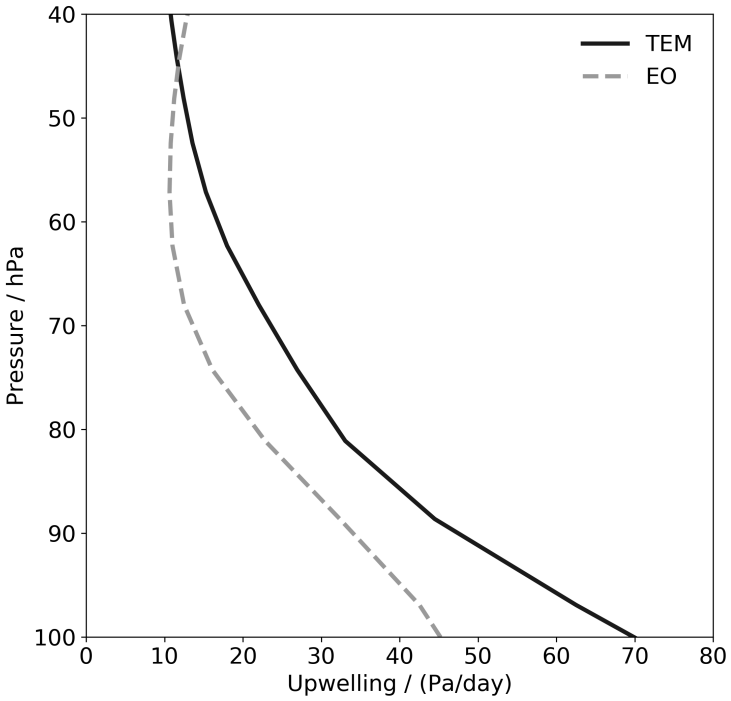

Figure 5.2.: Mean EO and TEM upwelling from ESCiMo RC1-Base-07 simulation (see text for details), averaged over the southern tropics (20S - equator) and the entire simulation period.

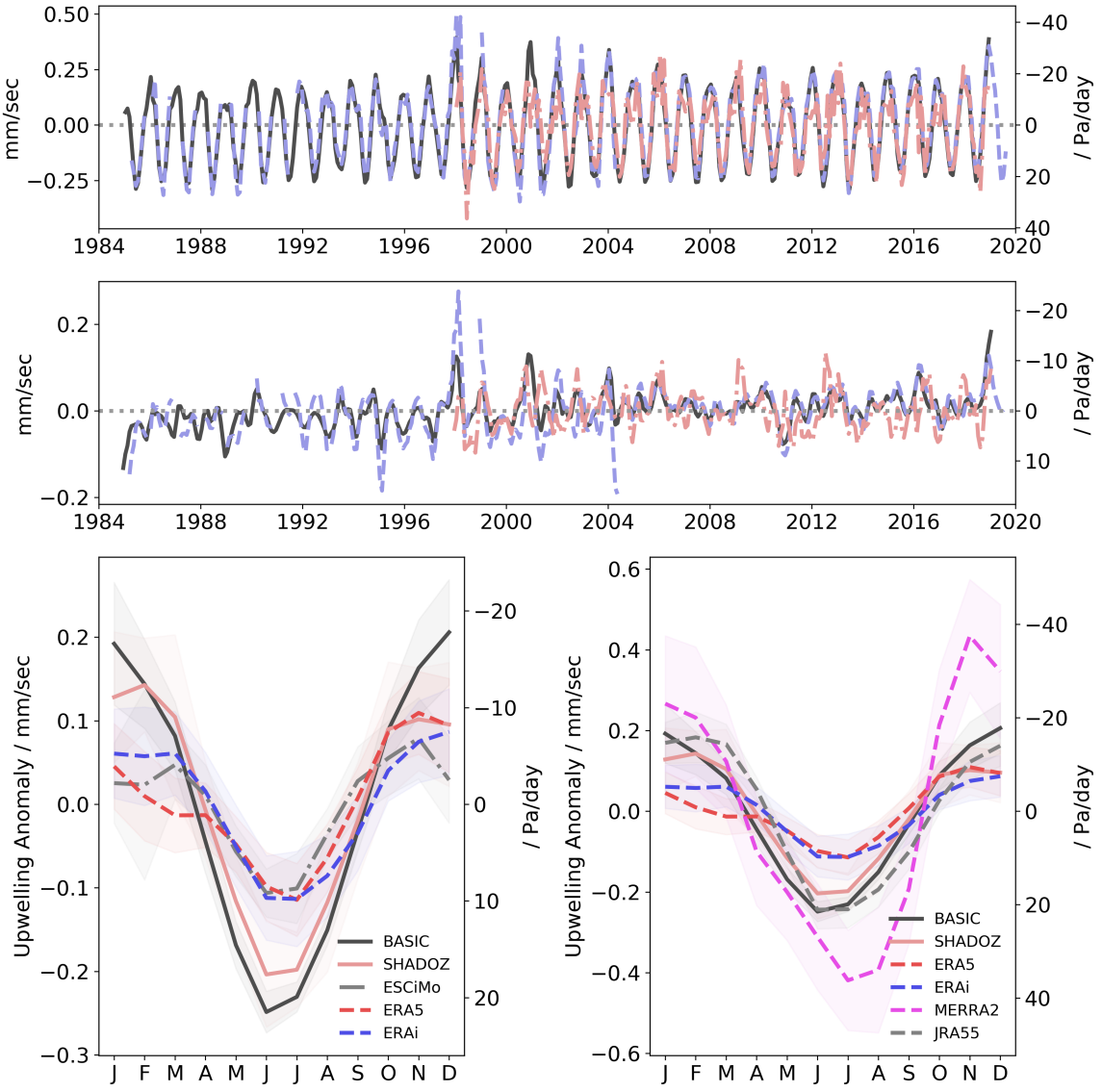

Figure 5.3.: Top and middle panels show EO upwelling from ozone datasets as total and three-month-average deseasonalized timeseries. Shown datasets are BASIC (black solid), SWOOSH (blue dashed), and SHADOZ (red dot-dashed). Bottom panels: EO Upwelling from SHADOZ, ESCiMo, and reanalyses. Left panel shows ESCiMo results and is focused on a tighter range of upwelling values for ease of interpretation, compared to right panel.

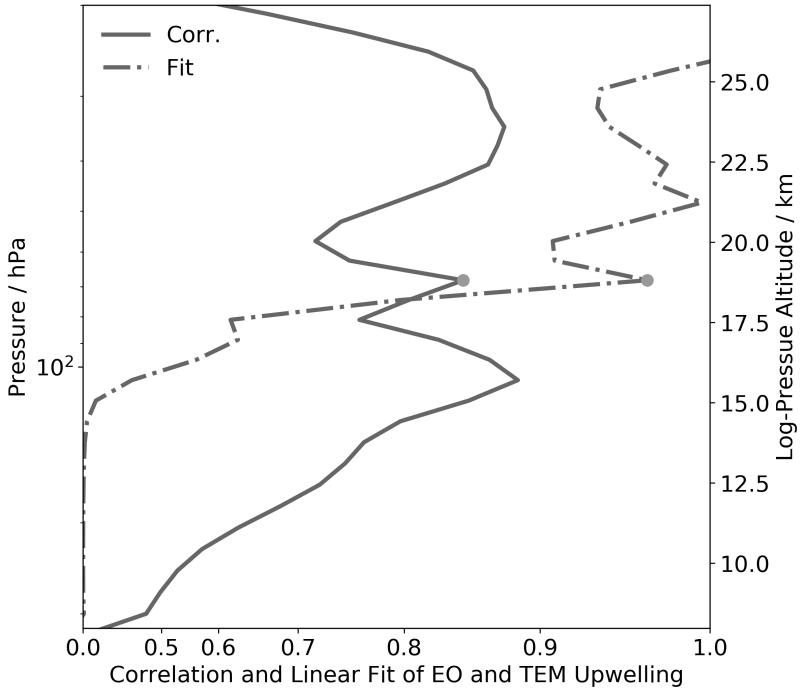

Figure 5.4.: Pearson correlation coefficient and linear fit between 3-month-average deseasonalized southern-tropics average EO and TEM upwelling from ESCiMo data. Note the non-linear scaling, which was applied to focus on correlation and fit values which could indicate the effectiveness of a proxy assumption.

6. A Closing Word

The first major result of this work shows that the flux-form semi-Lagrangian (FFSL) transport scheme – in common use among modern climate models – still shows signs of major effects due to numerical diffusion which are not present in the CLaMS fully-Lagrangian transport scheme. These effects appeared most strongly around transport barriers, such as around the tropopause or the polar vortex, which are also areas where the fine features of chemical distributions play significant roles in a number of processes.

For one example, the EMAC-FFSL age spectra within the southern polar vortex suggest that very short-lived substances – which are known contributors to ozone destruction – could breach this location after tropospheric emission and affect ozone concentrations there. This has also already been suggested by the work of Sinnhuber and Meul (2015). However, the EMAC-CLaMS transport scheme does not show similar results, suggesting that this possibility within a model may depend on the effects of unphysical numerical diffusion caused by the model's transport scheme.

In a much more widely researched case, water vapor within the extratropical lowermost stratosphere (LMS) is thought to be particularly potent with regards to local and surface radiative feedbacks, in both cases causing warming (Banerjee et al., 2019). Furthermore, this effect was likely in part due to the strong climate change-related moistening trends in the region, and Banerjee et al. (2019) suggested that of the total surface radiative feedback due to stratospheric water vapor, three-quarters was associated with increases in LMS water vapor. This region, however, was also shown to have the strongest wet biases with respect to observations by Keeble et al. (2020), which raises some uncertainty on the reliability of the wide body of research on the stratospheric water vapor radiative feedback (e.g., Solomon, K. Rosenlof, et al., 2010; Maycock, Joshi, Shine, et al., 2014), at least in quantitative terms. The present work raises more questions on this topic, as the EMAC-FFSL transport scheme was found to distribute much more water vapor into the extratropical LMS (roughly 100% more) compared to EMAC-CLaMS. As the EMAC-FFSL transport scheme is a state-of-the-art model, and similar to many schemes used in other modern climate models, these results should provide a call for more research on the roles of numerical diffusion in stratospheric transport, and for the expanded application of Lagrangian transport models.

The second major result of this work is the development of a new quantity (effective ozone upwelling) and method for estimating tropical upwelling from observations, a category which has very few contributions to date. Many of these studies have only made qualitative connections (e.g., Stiller, Fierli, et al., 2017) and some studies have provided quantitative estimates of limited features (e.g., Randel, F. Wu, Vömel, et

al., 2006). To the knowledge of the author, the most thorough quantitative estimates have been made by Fu, Hu, and Yang (2007) (using expensive radiative calculations) and Glanville and T. Birner (2017) (which was limited to calculating seasonal climatologies). The method described here has the advantages of relative computational ease and time resolution that includes inter-annual variability. Furthermore, the data required for this method (ozone mixing ratios) is available from multiple datasets which extend over relatively long periods. However, only the calculation of anomalies is useful for comparison to standard upwelling calculations, and when deseasonalized the data should be analyzed under a three-month running mean.

Calculations using this quantity seem to largely agree with reanalysis results in the seasonal cycle, with MERRA2 showing a stronger seasonal cycle, ERA products showing weaker seasonal cycles, and JRA55 showing a very similar seasonal cycle strength. The satellite-derived datasets (BASIC and SWOOSH) agree closely with each other in long-term trends and month-to-month variability, both showing a positive but statistically insignificant acceleration trend and being highly correlated with each other. The radiosonde-derived dataset of SHADOZ shows poor correlations with the satellite-based datasets and shows a very different trend, which is effectively zero.

Therefore, although the method described here shows promise of utility for estimating new characteristics of upwelling strength heretofore unavailable from observations, future work will need to focus on understanding what features of observational datasets affect estimated variability. Although the method shown in this work is fixed to ozone measurements, there is also potential for application to other chemicals for which observations are available. It is the conjecture of the author that N_2O, CH_4, and CO could be interesting candidates for such research.

This dissertation has investigated the stratospheric circulation through both modeling and observations. In terms of modeling results, it has been shown that there are considerable differences in the transport time scales resulting from the CLaMS Lagrangian and EMAC standard flux-form semi-Lagrangian transport schemes. It has also been shown that these differences in transport time scales correspond to major differences in resulting tracer distributions depending on the transport scheme used, most notably for very-short lifetime tracers (through convolution of age spectra i.e. "forward-tracers", as in Chapter 3) and water vapor (directly calculated as shown in Chapter 4). These differences in transport scheme characteristics suggest that Eulerian models may have substantial biases in tracer distributions within sensitive regions, motivating the continued study and integration of Lagrangian transport schemes in climate models. In terms of observation-based results, a novel measure of tropical stratospheric upwelling derived from ozone observations has been presented, verified as an effective proxy for standard upwelling, and derived from observations. These dual results – from both model and observation approaches – provide avenues for the expansion of knowledge on the stratosphere and its circulation.

Bibliography

[1] M. Abalos, B. Legras, F. Ploeger, et al. "Evaluating the advective Brewer-Dobson circulation in three reanalyses for the period 1979–2012". In: *Journal of Geophysical Research: Atmospheres* 120.15 (2015), pp. 7534–7554. DOI: 10.1002/2015JD023182.

[2] M. Abalos, B. Legras, and E. Shuckburgh. "Interannual variability in effective diffusivity in the upper troposphere/lower stratosphere from reanalysis data". In: *Quarterly Journal of the Royal Meteorological Society* 142.697 (2016), pp. 1847–1861. DOI: 10.1002/qj.2779.

[3] M. Abalos, F. Ploeger, et al. "Ozone seasonality above the tropical tropopause: reconciling the Eulerian and Lagrangian perspectives of transport processes". In: *Atmospheric Chemistry and Physics* 13.21 (2013), pp. 10787–10794. DOI: 10.5194/acp-13-10787-2013.

[4] M. Abalos, W. J. Randel, D. E. Kinnison, and R. R. Garcia. "Using the Artificial Tracer e90 to Examine Present and Future UTLS Tracer Transport in WACCM". In: *Journal of the Atmospheric Sciences* 74.10 (2017), pp. 3383–3403. DOI: 10.1175/JAS-D-17-0135.1.

[5] M. Abalos, W. J. Randel, D. E. Kinnison, and E. Serrano. "Quantifying tracer transport in the tropical lower stratosphere using WACCM". In: *Atmospheric Chemistry and Physics* 13.21 (2013), pp. 10591–10607. DOI: 10.5194/acp-13-10591-2013.

[6] M. Abalos, W. J. Randel, and E. Serrano. "Variability in upwelling across the tropical tropopause and correlations with tracers in the lower stratosphere". In: *Atmospheric Chemistry and Physics* 12.23 (2012), pp. 11505–11517. DOI: 10.5194/acp-12-11505-2012.

[7] D. G. Andrews and M. E. McIntyre. "Planetary Waves in Horizontal and Vertical Shear: The Generalized Eliassen-Palm Relation and the Mean Zonal Acceleration". In: *Journal of Atmospheric Sciences* 33.11 (1976), pp. 2031–2048. DOI: 10.1175/1520-0469(1976)033<2031:PWIHAV>2.0.CO;2.

[8] D. G. Andrews and M. E. Mcintyre. "An exact theory of nonlinear waves on a Lagrangian-mean flow". In: *Journal of Fluid Mechanics* 89.4 (1978), pp. 609–646. DOI: 10.1017/S0022112078002773.

[9] D. G. Andrews and M. E. Mcintyre. "An exact theory of nonlinear waves on a Lagrangian-mean flow". In: *Journal of Fluid Mechanics* 89.4 (1978), pp. 609–646. DOI: 10.1017/S0022112078002773.

[10] D. Andrews and M. Mcintyre. "Generalized Eliassen-Palm and Charney-Drazin Theorems for Waves on Axismmetric Mean Flows in Compressible Atmospheres". In: *Journal of The Atmospheric Sciences - J ATMOS SCI* 35 (Jan. 1978), pp. 175–185. DOI: 10.1175/1520-0469(1978)035<0175:GEPACD>2.0.CO;2.

[11] V. Aquila et al. "Isolating the roles of different forcing agents in global stratospheric temperature changes using model integrations with incrementally added single forcings". In: *Journal of Geophysical Research: Atmospheres* 121.13 (2016), pp. 8067–8082. DOI: https://doi.org/10.1002/2015JD023841.

[12] L. M. Avallone and M. J. Prather. "Photochemical evolution of ozone in the lower tropical stratosphere". In: *Journal of Geophysical Research: Atmospheres* 101.D1 (1996), pp. 1457–1461. DOI: 10.1029/95JD03010.

[13] M. P. Baldwin et al. "Sudden Stratospheric Warmings". In: *Reviews of Geophysics* 59.1 (2021), e2020RG000708. DOI: https://doi.org/10.1029/2020RG000708.

[14] W. T. Ball et al. "Evidence for a continuous decline in lower stratospheric ozone offsetting ozone layer recovery". In: *Atmospheric Chemistry and Physics* 18.2 (2018), pp. 1379–1394. DOI: 10.5194/acp-18-1379-2018.

[15] A. Banerjee et al. "Stratospheric water vapor: an important climate feedback". In: *Climate Dynamics* (Aug. 2019). DOI: 10.1007/s00382-019-04721-4.

[16] T. Birner and H. Bönisch. "Residual circulation trajectories and transit times into the extratropical lowermost stratosphere". In: *Atmospheric Chemistry and Physics* 11.2 (2011), pp. 817–827. DOI: 10.5194/acp-11-817-2011.

[17] T. Birner and E. J. Charlesworth. "On the relative importance of radiative and dynamical heating for tropical tropopause temperatures". In: *Journal of Geophysical Research: Atmospheres* 122.13 (2017), pp. 6782–6797. DOI: https://doi.org/10.1002/2016JD026445.

[18] H. Bönisch, A. Engel, Th. Birner, et al. "On the structural changes in the Brewer-Dobson circulation after 2000". In: *Atmospheric Chemistry and Physics* 11.8 (2011), pp. 3937–3948. DOI: 10.5194/acp-11-3937-2011.

[19] H. Bönisch, A. Engel, J. Curtius, et al. "Quantifying transport into the lowermost stratosphere using simultaneous in-situ measurements of SF_6 and CO_2". In: *Atmos. Chem. Phys.* 9 (2009), pp. 5905–5919.

[20] G. Brasseur and S. Solomon. *Aeronomy of the middle atmosphere*. P.O. Box 17, 3300 AA Dordrecht, The Netherlands: Springer, 2005. ISBN: 1-4020-3284-6.

[21] A. W. Brewer. "Evidence for a world circulation provided by the measurements of helium and water vapour distribution in the stratosphere". In: *Quarterly Journal of the Royal Meteorological Society* 75.326 (1949), pp. 351–363. DOI: 10.1002/qj.49707532603.

[22] S. Brinkop and P. Jöckel. "ATTILA 4.0: Lagrangian advective and convective transport of passive tracers within the ECHAM5/MESSy (2.53.0) chemistry–climate model". In: *Geoscientific Model Development* 12.5 (2019), pp. 1991–2008. DOI: 10.5194/gmd-12-1991-2019.

[23] J. B. Burkholder et al. *Chemical Kinetics and Photochemical Data for Use in Atmospheric Studies, Evaluation No. 18*. Tech. rep. Pasadena, California: Jet Propulsion Laboratory, 1993.

[24] N. Butchart. "The Brewer-Dobson circulation". In: *Reviews of Geophysics* 52.2 (2014), pp. 157–184. DOI: 10.1002/2013RG000448.

[25] N. Butchart and A. A. Scaife. "Removal of chlorofluorocarbons by increased mass exchange between the stratosphere and troposphere in a changing climate". In: *Nature* 410.6830 (Apr. 2001), pp. 799–802. ISSN: 1476-4687. DOI: 10.1038/35071047.

[26] A. H. Butler et al. "A sudden stratospheric warming compendium". In: *Earth Syst. Sci. Data* 9 (2017), pp. 63–76. DOI: 10.5194/essd-9-63-2017.

[27] N. Calvo et al. "Dynamical Mechanism for the Increase in Tropical Upwelling in the Lowermost Tropical Stratosphere during Warm ENSO Events". In: *Journal of the Atmospheric Sciences* 67.7 (2010), pp. 2331–2340. DOI: 10.1175/2010JAS3433.1.

[28] D. L. Chapman. "XXXV. On ozone and atomic oxygen in the upper atmosphere". In: *The London, Edinburgh, and Dublin Philosophical Magazine and Journal of Science* 10.64 (1930), pp. 369–383. DOI: 10.1080/14786443009461588.

[29] E. J. Charlesworth, T. Birner, and J. R. Albers. "Ozone Transport-Radiation Feedbacks in the Tropical Tropopause Layer". In: *Geophysical Research Letters* 46.23 (2019), pp. 14195–14202. DOI: https://doi.org/10.1029/2019GL084679.

[30] E. J. Charlesworth, A.-K. Dugstad, et al. "Impact of Lagrangian transport on lower-stratospheric transport timescales in a climate model". In: *Atmospheric Chemistry and Physics* 20.23 (2020), pp. 15227–15245. DOI: 10.5194/acp-20-15227-2020.

[31] J. G. Charney et al. *Carbon Dioxide and Climate*. Woods Hole, Massachusetts.

[32] M. P. Chipperfield et al. "On the Cause of Recent Variations in Lower Stratospheric Ozone". In: *Geophysical Research Letters* 45.11 (2018), pp. 5718–5726. DOI: https://doi.org/10.1029/2018GL078071.

[33] O. Coddington et al. "Solar Irradiance Variability: Comparisons of Models and Measurements". In: *Earth and Space Science* 6.12 (2019), pp. 2525–2555. DOI: https://doi.org/10.1029/2019EA000693.

[34] P. J. Crutzen. "Albedo enhancements by stratospheric sulfur injections: a contribution to resolve a policy dilemma? An Editorial Essay". In: *Clim. Change* 77 (2006), pp. 211–219.

[35] R. Deckert et al. “A quasi chemistry-transport model mode for EMAC”. In: *Geoscientific Model Development* 4.1 (2011), pp. 195–206. DOI: 10.5194/gmd-4-195-2011.

[36] A. E. Dessler et al. “Stratospheric water vapor feedback”. In: *Proceedings of the National Academy of Sciences* 110.45 (2013), pp. 18087–18091. ISSN: 0027-8424. DOI: 10.1073/pnas.1310344110. eprint: https://www.pnas.org/content/110/45/18087.full.pdf.

[37] M. Diallo, P. Konopka, et al. “Structural changes in the shallow and transition branch of the Brewer–Dobson circulation induced by El Niño”. In: *Atmospheric Chemistry and Physics* 19.1 (Jan. 11, 2019), pp. 425–446. ISSN: 1680-7316. DOI: https://doi.org/10.5194/acp-19-425-2019.

[38] M. Diallo, B. Legras, and A. Chédin. “Age of stratospheric air in the ERA-Interim”. In: *Atmos. Chem. Phys.* 12.24 (2012), pp. 12133–12154. DOI: 10.5194/acp-12-12133-2012.

[39] G. M. B. Dobson, D. N. Harrison, and F. A. Lindemann. “Measurements of the amount of ozone in the earth’s atmosphere and its relation to other geophysical conditions”. In: *Proceedings of the Royal Society of London. Series A, Containing Papers of a Mathematical and Physical Character* 110.756 (1926), pp. 660–693. DOI: 10.1098/rspa.1926.0040.

[40] G. M. B. Dobson and H. S. W. Massey. “Origin and distribution of the polyatomic molecules in the atmosphere”. In: *Proceedings of the Royal Society of London. Series A. Mathematical and Physical Sciences* 236.1205 (1956), pp. 187–193. DOI: 10.1098/rspa.1956.0127.

[41] K. Dubé et al. “Trends and Variability in Stratospheric NOx Derived From Merged SAGE II and OSIRIS Satellite Observations”. In: *Journal of Geophysical Research: Atmospheres* 125.7 (2020), e2019JD031798. DOI: https://doi.org/10.1029/2019JD031798.

[42] T. Dunkerton. “On the Mean Meridional Mass Motions of the Stratosphere and Mesosphere”. In: *Journal of Atmospheric Sciences* 35.12 (1978), pp. 2325–2333. DOI: 10.1175/1520-0469(1978)035<2325:OTMMMM>2.0.CO;2.

[43] J. Eluszkiewicz et al. “Sensitivity of Age-of-Air Calculations to the Choice of Advection Scheme”. In: *Journal of the Atmospheric Sciences* 57.19 (2000), pp. 3185–3201. DOI: 10.1175/1520-0469(2000)057<3185:SOAOAC>2.0.CO;2.

[44] A. Engel, H. Bönisch, et al. “Mean age of stratospheric air derived from AirCore observations”. In: *Atmospheric Chemistry and Physics* 17.11 (2017), pp. 6825–6838. DOI: 10.5194/acp-17-6825-2017.

[45] A. Engel, T. Möbius, et al. “Age of stratospheric air unchanged within uncertainties over the past 30 years”. In: *Nature Geoscience* 2 (2009), pp. 28–31. DOI: 10.1038/ngeo388.

[46] V. Eyring et al. “Assessment of temperature, trace species, and ozone in chemistry-climate model simulations of the recent past”. In: *Journal of Geophysical Research: Atmospheres* 111.D22 (2006). DOI: https://doi.org/10.1029/2006JD007327.

[47] P. M. Forster et al. “Latest climate models confirm need for urgent mitigation”. In: *Nat. Clim. Change* 10 (2020). DOI: 10.1038/s41558-019-0660-0.

[48] F. Fritsch et al. “Sensitivity of Age of Air Trends on the derivation method for non-linear increasing tracers”. In: *Atmospheric Chemistry and Physics Discussions* 2019 (2019), pp. 1–23. DOI: 10.5194/acp-2019-974.

[49] F. Fritsch et al. “Sensitivity of age of air trends to the derivation method for non-linear increasing inert SF_6”. In: *Atmospheric Chemistry and Physics* 20.14 (July 23, 2020), pp. 8709–8725. ISSN: 1680-7316. DOI: https://doi.org/10.5194/acp-20-8709-2020.

[50] Q. Fu, Y. Hu, and Q. Yang. “Identifying the top of the tropical tropopause layer from vertical mass flux analysis and CALIPSO lidar cloud observations”. In: *Geophysical Research Letters* 34.14 (2007). DOI: 10.1029/2007GL030099.

[51] S. Fueglistaler et al. “Tropical tropopause layer”. In: *Rev. Geophys.* 47, RG1004 (2009). DOI: 10.1029/2008RG000267.

[52] R. R. Garcia and S. Solomon. “The effect of breaking gravity waves on the dynamics and chemical composition of the mesosphere and lower thermosphere”. In: *Journal of Geophysical Research: Atmospheres* 90.D2 (1985), pp. 3850–3868. DOI: https://doi.org/10.1029/JD090iD02p03850.

[53] A. A. Glanville and T. Birner. “Role of vertical and horizontal mixing in the tape recorder signal near the tropical tropopause”. In: *Atmospheric Chemistry and Physics* 17.6 (2017), pp. 4337–4353. DOI: 10.5194/acp-17-4337-2017.

[54] A. R. Gregory and V. West. “The sensitivity of a model’s stratospheric tape recorder to the choice of advection scheme”. In: *Q. J. R. Meteorol. Soc.* 1 (2002), pp. 64–75. DOI: 10.1038/s43017-019-0004-7.

[55] A. Gupta, E. P. Gerber, and P. H. Lauritzen. “Numerical impacts on tracer transport: A proposed intercomparison test of Atmospheric General Circulation Models”. In: *Quarterly Journal of the Royal Meteorological Society* 146.733 (2020). DOI: 10.1002/qj.3881.

[56] T. M. Hall and R. A. Plumb. “Age as a diagnostic of stratospheric transport”. In: *Journal of Geophysical Research: Atmospheres* 99.D1 (1994), pp. 1059–1070.

[57] T. M. Hall, D. W. Waugh, et al. “Evaluation of transport in stratospheric models”. In: *Journal of Geophysical Research: Atmospheres* 104.D15 (1999), pp. 18815–18839. DOI: 10.1029/1999JD900226.

[58] S. C. Hardiman, N. Butchart, and N. Calvo. "The morphology of the Brewer–Dobson circulation and its response to climate change in CMIP5 simulations". In: *Quarterly Journal of the Royal Meteorological Society* 140.683 (2013), pp. 1958–1965. DOI: https://doi.org/10.1002/qj.2258.

[59] S. C. Hardiman, P. Lin, et al. "The influence of dynamical variability on the observed Brewer-Dobson circulation trend". In: *Geophysical Research Letters* 44.6 (2017), pp. 2885–2892. DOI: https://doi.org/10.1002/2017GL072706.

[60] M. Hauck, H. Bönisch, et al. "A convolution of observational and model data to estimate age of air spectra in the northern hemispheric lower stratosphere". In: *Atmospheric Chemistry and Physics* 20.14 (2020), pp. 8763–8785. DOI: 10.5194/acp-20-8763-2020.

[61] M. Hauck, F. Fritsch, et al. "Deriving stratospheric age of air spectra using an idealized set of chemically active trace gases". In: *Atmospheric Chemistry and Physics* 19.7 (2019), pp. 5269–5291. DOI: 10.5194/acp-19-5269-2019.

[62] P. Haynes and E. Shuckburgh. "Effective diffusivity as a diagnostic of atmospheric transport: 1. Stratosphere". In: *Journal of Geophysical Research: Atmospheres* 105.D18 (2000), pp. 22777–22794. DOI: 10.1029/2000JD900093.

[63] M. I. Hegglin et al. "Vertical structure of stratospheric water vapour trends derived from merged satellite data". In: *Nature Geoscience* 7.10 (Oct. 2014), pp. 768–776. ISSN: 1752-0908. DOI: 10.1038/ngeo2236.

[64] P. Hitchcock, T. G. Shepherd, and S. Yoden. "On the Approximation of Local and Linear Radiative Damping in the Middle Atmosphere". In: *Journal of the Atmospheric Sciences* 67.6 (2010), pp. 2070–2085. DOI: 10.1175/2009JAS3286.1.

[65] J. R. Holton et al. "Stratosphere-troposphere exchange". In: *Rev. Geophys.* 33 (1995), pp. 403–439.

[66] C. M. Hoppe, L. Hoffmann, et al. "The implementation of the CLaMS Lagrangian transport core into the chemistry climate model EMAC 2.40.1: application on age of air and transport of long-lived trace species". In: *Geoscientific Model Development* 7.6 (2014), pp. 2639–2651. DOI: 10.5194/gmd-7-2639-2014.

[67] C. M. Hoppe, F. Ploeger, et al. "Kinematic and diabatic vertical velocity climatologies from a chemistry climate model". In: *Atmospheric Chemistry and Physics* 16.10 (2016), pp. 6223–6239. DOI: 10.5194/acp-16-6223-2016.

[68] Y. Huang Y. Wang and H. Huang. "Stratospheric Water Vapor Feedback Disclosed by a Locking Experiment". In: *Geophysical Research Letters* 47 (May 2020). DOI: 10.1029/2020GL087987.

[69] IPCC. *Climate Change 2013: The Physical Science Basis. Contribution of Working Group I to the Fifth Assessment Report of the Intergovernmental Panel on Climate Change*. Cambridge, United Kingdom and New York, NY, USA: Cambridge University Press, 2013, p. 1535. ISBN: ISBN 978-1-107-66182-0. DOI: 10.1017/CBO9781107415324.

[70] P. Jöckel, A. Kerkweg, et al. "Development cycle 2 of the Modular Earth Submodel System (MESSy2)". In: *Geoscientific Model Development* 3.2 (2010), pp. 717–752. DOI: 10.5194/gmd-3-717-2010.

[71] P. Jöckel, R. Sander, et al. "Technical Note: The Modular Earth Submodel System (MESSy) - a new approach towards Earth System Modeling". In: *Atmospheric Chemistry and Physics* 5.2 (2005), pp. 433–444. DOI: 10.5194/acp-5-433-2005.

[72] P. Jöckel, H. Tost, et al. "Earth System Chemistry integrated Modelling (ESCiMo) with the Modular Earth Submodel System (MESSy) version 2.51". In: *Geoscientific Model Development* 9.3 (2016), pp. 1153–1200. DOI: 10.5194/gmd-9-1153-2016.

[73] J. Keeble et al. "Evaluating stratospheric ozone and water vapor changes in CMIP6 models from 1850–2100". In: *Atmospheric Chemistry and Physics Discussions* 2020 (2020), pp. 1–68. DOI: 10.5194/acp-2019-1202.

[74] J. Kent, P. A. Ullrich, and C. Jablonowski. "Dynamical core model intercomparison project: Tracer transport test cases". In: *Quarterly Journal of the Royal Meteorological Society* 140.681 (2014), pp. 1279–1293. DOI: 10.1002/qj.2208.

[75] P. Konopka, J.-U. Grooß, et al. "Annual cycle of ozone at and above the tropical tropopause: observations versus simulations with the Chemical Lagrangian Model of the Stratosphere (CLaMS)". In: *Atmospheric Chemistry and Physics* 10.1 (2010), pp. 121–132. DOI: 10.5194/acp-10-121-2010.

[76] P. Konopka, G. Günther, et al. "Contribution of mixing to upward transport across the tropical tropopause layer (TTL)". In: *Atmospheric Chemistry and Physics* 7.12 (2007), pp. 3285–3308. DOI: 10.5194/acp-7-3285-2007.

[77] P. Konopka, H. Steinhorst, et al. "Mixing and ozone loss in the 1999–2000 Arctic vortex: Simulations with the three-dimensional Chemical Lagrangian Model of the Stratosphere (CLaMS)". In: *Journal of Geophysical Research: Atmospheres* 109.D2 (2004). DOI: 10.1029/2003JD003792.

[78] J. Krause et al. "Mixing and ageing in the polar lower stratosphere in winter 2015–2016". In: *Atmos. Chem. Phys.* 18 (2018), pp. 6057–6073.

[79] B. Kravitz and G. Douglas. "Uncertainty and the basis for confidence in solar geoengineering research". In: *Nat. Rev. Earth Environ.* 128 (2020), pp. 1827–1846. DOI: https://doi.org/10.1256/003590002320603430.

[80] J. C. Laube et al. “Investigating stratospheric changes between 2009 and 2018 with halogenated trace gas data from aircraft, AirCores, and a global model focusing on CFC–11”. In: *Atmospheric Chemistry and Physics* 20.16 (Aug. 20, 2020), pp. 9771–9782. ISSN: 1680-7316. DOI: https://doi.org/10.5194/acp-20-9771-2020.

[81] F. Li and P. Newman. “Stratospheric water vapor feedback and its climate impacts in the coupled atmosphere–ocean Goddard Earth Observing System Chemistry-Climate Model”. In: *Climate Dynamics* 55 (Sept. 2020). DOI: 10.1007/s00382-020-05348-6.

[82] F. Li, D. W. Waugh, et al. “Seasonal variations in stratospheric age spectra in GEOSCCM”. In: *J. Geophys. Res.* 117, D5 (2012). DOI: 10.1029/2011JD016877.

[83] S. Lin. “A “vertically Lagrangian” finite-volume dynamical core for global models”. In: *Monthly Weather Review* 132.10 (2004), 2293–2307.

[84] S. Lin and R. B. Rood. “Multidimensional Flux-Form Semi-Lagrangian Transport Schemes”. In: *Monthly Weather Review* 124.9 (1996), pp. 2046–2070. DOI: 10.1175/1520-0493(1996)124<2046:MFFSLT>2.0.CO;2.

[85] M. Linz et al. “The strength of the meridional overturning circulation of the stratosphere”. In: *Nature Geoscience* 10 (Aug. 2017). DOI: 10.1038/ngeo3013.

[86] S. Manabe and R.T. Wetherald. “Thermal Equilibrium of the Atmosphere with a Given Distribution of Relative Humidity”. In: *Journal of Atmospheric Sciences* 24.3 (1967), pp. 241–259. DOI: 10.1175/1520-0469(1967)024<0241:TEOTAW>2.0.CO;2.

[87] A. C. Maycock, M. M. Joshi, Shine K. P., et al. “The Circulation Response to Idealized Changes in Stratospheric Water Vapor”. In: *Journal of Climate* 26.2 (2013), pp. 545–561. DOI: 10.1175/JCLI-D-12-00155.1.

[88] A. C. Maycock, M. M. Joshi, K. P. Shine, et al. “The potential impact of changes in lower stratospheric water vapour on stratospheric temperatures over the past 30 years”. In: *Quarterly Journal of the Royal Meteorological Society* 140.684 (2014), pp. 2176–2185. DOI: https://doi.org/10.1002/qj.2287.

[89] A. C. Maycock, K. P. Shine, and M. M. Joshi. “The temperature response to stratospheric water vapour changes”. In: *Quarterly Journal of the Royal Meteorological Society* 137.657 (2011), pp. 1070–1082. DOI: https://doi.org/10.1002/qj.822.

[90] M. E. McIntyre and T. N. Palmer. “The ‘surf zone’ in the stratosphere”. In: *Journal of Atmospheric and Terrestrial Physics* 46.9 (1984), pp. 825–849. ISSN: 0021-9169. DOI: https://doi.org/10.1016/0021-9169(84)90063-1.

[91] M. Mcintyre and T. Palmer. “Breaking waves in the stratosphere”. In: *Nature* 305 (Oct. 1983), pp. 593–600. DOI: 10.1038/305593a0.

[92] D. S. McKenna et al. “A new Chemical Lagrangian Model of the Stratosphere (CLaMS): 1. Formulation of advection and mixing”. In: *J. Geophys. Res.* 107.D16, 4309 (2002), p. 4309. DOI: 10.1029/2000JD000114.

[93] K. Minschwaner et al. “Polynomial coefficients for calculating O2 Schumann-Runge cross sections at 0.5 cm–1 resolution”. In: *Journal of Geophysical Research: Atmospheres* 97 (D9 1992), pp. 10103–10108. DOI: https://doi.org/10.1029/92JD00661.

[94] S. Montzka et al. “An unexpected and persistent increase in global emissions of ozone-depleting CFC-11”. In: *Nature* 557 (May 2018), pp. 413–417. DOI: 10.1038/s41586-018-0106-2.

[95] O. Morgenstern et al. “Review of the formulation of present-generation stratospheric chemistry-climate models and associated external forcings”. In: *J. Geophys. Res.* 115, D00M02 (2010). DOI: 10.1029/2009JD013728.

[96] P. W. Mote et al. “An atmospheric tape recorder: The imprint of tropical tropopause temperatures on stratospheric water vapor”. In: *Journal of Geophysical Research: Atmospheres* 101.D2 (1996), pp. 3989–4006. DOI: https://doi.org/10.1029/95JD03422.

[97] R. J. Murgatroyd and F. Singleton. “Possible meridional circulations in the stratosphere and mesosphere”. In: *Quarterly Journal of the Royal Meteorological Society* 87.372 (1961), pp. 125–135. DOI: https://doi.org/10.1002/qj.49708737202.

[98] S. Oberländer-Hayn et al. “Is the Brewer-Dobson circulation increasing or moving upward?” In: *Geophysical Research Letters* 43.4 (2016), pp. 1772–1779. DOI: 10.1002/2015GL067545.

[99] I. Pisso et al. “The Lagrangian particle dispersion model FLEXPART version 10.4”. In: *Geoscientific Model Development* 12.12 (2019), pp. 4955–4997. DOI: 10.5194/gmd-12-4955-2019.

[100] F. Ploeger and T. Birner. “Seasonal and inter-annual variability of lower stratospheric age of air spectra”. In: *Atmos. Chem. Phys.* 2016 (2016), pp. 10195–10213. DOI: 10.5194/acp-16-10195-2016.

[101] F. Ploeger, P. Konopka, et al. “Horizontal transport affecting trace gas seasonality in the Tropical Tropopause Layer (TTL)”. In: *Journal of Geophysical Research: Atmospheres* 117.D9 (2012). DOI: https://doi.org/10.1029/2011JD017267.

[102] F. Ploeger, B. Legras, et al. “How robust are stratospheric age of air trends from different reanalyses?” In: *Atmospheric Chemistry and Physics* 19.9 (2019), pp. 6085–6105. DOI: 10.5194/acp-19-6085-2019.

[103] R. A. Plumb. “A “tropical pipe” model of stratospheric transport”. In: *J. Geophys. Res.* 101 (1996), pp. 3957–3972.

[104] R. A. Plumb. "Stratospheric transport". In: *J. Meteorol. Soc. Jpn.* 80.4B (2002), pp. 793–809.

[105] R. A. Plumb. "Tracer interrelationships in the stratosphere". In: *Reviews of Geophysics* 45.4 (2007). DOI: https://doi.org/10.1029/2005RG000179.

[106] M. J. Prather et al. "An atmospheric chemist in search of the tropopause". In: *Journal of Geophysical Research: Atmospheres* 116.D4 (2011). DOI: 10.1029/2010JD014939.

[107] W. J. Randel, M. Park, et al. "A Large Annual Cycle in Ozone above the Tropical Tropopause Linked to the Brewer–Dobson Circulation". In: *Journal of the Atmospheric Sciences* 64.12 (2007), pp. 4479–4488. DOI: 10.1175/2007JAS2409.1.

[108] W. J. Randel, A. K. Smith, et al. "Stratospheric Temperature Trends over 1979–2015 Derived from Combined SSU, MLS, and SABER Satellite Observations". In: *Journal of Climate* 29.13 (2016), pp. 4843–4859. DOI: 10.1175/JCLI-D-15-0629.1.

[109] W. J. Randel, F. Wu, S. J. Oltmans, et al. "Interannual Changes of Stratospheric Water Vapor and Correlations with Tropical Tropopause Temperatures". In: *Journal of the Atmospheric Sciences* 61.17 (2004), pp. 2133–2148. DOI: 10.1175/1520-0469(2004)061<2133:ICOSWV>2.0.CO;2.

[110] W. J. Randel, F. Wu, H. Vömel, et al. "Decreases in stratospheric water vapor after 2001: Links to changes in the tropical tropopause and the Brewer-Dobson circulation". In: *Journal of Geophysical Research: Atmospheres* 111.D12 (2006). DOI: https://doi.org/10.1029/2005JD006744.

[111] E. A. Ray et al. "Quantification of the SF6 lifetime based on mesospheric loss measured in the stratospheric polar vortex". In: *Journal of Geophysical Research: Atmospheres* 122.8 (2017), pp. 4626–4638. DOI: https://doi.org/10.1002/2016JD026198.

[112] N. A. Rayner et al. "Global analyses of sea surface temperature, sea ice, and night marine air temperature since the late nineteenth century". In: *Journal of Geophysical Research: Atmospheres* 108.D14 (2003). DOI: 10.1029/2002JD002670.

[113] C. Reithmeier and R. Sausen. "Investigating lower stratospheric model transport: Lagrangian calculations of mean age and age spectra in the GCM ECHAM4". In: *Clim. Dynamics* 30 (2-3 2008), pp. 225–238.

[114] L. E. Revell et al. "The role of methane in projections of 21st century stratospheric water vapor". In: *Atmos. Chem. Phys.* 16 (2016), pp. 13067–13080. DOI: 10.5194/acp-16-13067-2016.

[115] M. Riese et al. "Impact of uncertainties in atmospheric mixing on simulated UTLS composition and related radiative effects". In: *J. Geophys. Res.* 117, D16305 (2012). DOI: 10.1029/2012JD017751.

[116] M. Rigby et al. “Increase in CFC-11 emissions from eastern China based on atmospheric observations”. In: *Nature* 569.7757 (May 2019), pp. 546–550. ISSN: 1476-4687. DOI: 10.1038/s41586-019-1193-4.

[117] E. Roeckner et al. “Sensitivity of Simulated Climate to Horizontal and Vertical Resolution in the ECHAM5 Atmosphere Model”. In: *Journal of Climate* 19.16 (2006), pp. 3771–3791. DOI: 10.1175/JCLI3824.1.

[118] R. B. Rood. “Numerical advection algorithms and their role in atmospheric transport and chemistry models”. In: *Reviews of Geophysics* 25.1 (1987), pp. 71–100. DOI: 10.1029/RG025i001p00071.

[119] K. H. Rosenlof et al. “Hemispheric asymmetries in the water vapor and inferences about transport in the lower stratosphere”. In: *J. Geophys. Res.* 102 (1997), pp. 13213–13234. DOI: {10.1029/97JD00873}.

[120] R. Sander et al. “The photolysis module JVAL-14, compatible with the MESSy standard, and the JVal PreProcessor (JVPP)”. In: *Geoscientific Model Development* 7.6 (2014), pp. 2653–2662. DOI: 10.5194/gmd-7-2653-2014.

[121] M. Saunois et al. “The Global Methane Budget 2000–2017”. In: *Earth System Science Data* 12.3 (2020), pp. 1561–1623. DOI: 10.5194/essd-12-1561-2020.

[122] T. G. Shepherd. “Transport in the middle atmosphere”. In: *J. Med. Soc. Japan* 85B (2007), pp. 165–191.

[123] B. Sinnhuber and S. Meul. “Simulating the impact of emissions of brominated very short lived substances on past stratospheric ozone trends”. In: *Geophysical Research Letters* 42.7 (2015), pp. 2449–2456. DOI: 10.1002/2014GL062975.

[124] S. Solomon, R. R. Garcia, and F. Stordal. “Transport processes and ozone perturbations”. In: *Journal of Geophysical Research: Atmospheres* 90.D7 (1985), pp. 12981–12989. DOI: 10.1029/JD090iD07p12981.

[125] S. Solomon, J. Haskins, et al. “Fundamental differences between Arctic and Antarctic ozone depletion”. In: *Proceedings of the National Academy of Sciences* 111.17 (2014), pp. 6220–6225. ISSN: 0027-8424. DOI: 10.1073/pnas.1319307111. eprint: https://www.pnas.org/content/111/17/6220.full.pdf.

[126] S. Solomon, D. Ivy, et al. “Mirrored changes in Antarctic ozone and stratospheric temperature in the late 20th versus early 21st centuries”. In: *Journal of Geophysical Research: Atmospheres* 122.16 (2017), pp. 8940–8950. DOI: https://doi.org/10.1002/2017JD026719.

[127] S. Solomon, K. Rosenlof, et al. “Contributions of stratospheric water vapor to decadal changes in the rate of global warming”. In: *Science* 327 (2010), pp. 1219–1223. DOI: 10.1126/science.1182488.

[128] A. Stenke et al. “Implications of Lagrangian transport for coupled chemistry-climate simulations”. In: *Atmos. Chem. Phys. Discuss.* 8 (2008), pp. 18727–18764.

[129] A. Stenke et al. “Implications of Lagrangian transport for simulations with a coupled chemistry-climate model”. In: *Atmos. Chem. Phys.* 9.15 (2009), pp. 5489–5504. URL: http://www.atmos-chem-phys.net/9/5489/2009/.

[130] G. P. Stiller, T. von Clarmann, et al. “Observed temporal evolution of global mean age of stratospheric air for the 2002 to 2010 period”. In: *Atmospheric Chemistry and Physics* 12.7 (2012), pp. 3311–3331. DOI: 10.5194/acp-12-3311-2012.

[131] G. P. Stiller, F. Fierli, et al. “Shift of subtropical transport barriers explains observed hemispheric asymmetry of decadal trends of age of air”. In: *Atmospheric Chemistry and Physics* 17.18 (2017), pp. 11177–11192. DOI: 10.5194/acp-17-11177-2017.

[132] R. S. Stolarski et al. “Seasonal variation of ozone in the tropical lower stratosphere: Southern tropics are different from northern tropics”. In: *Journal of Geophysical Research: Atmospheres* 119.10 (2014), pp. 6196–6206. DOI: https://doi.org/10.1002/2013JD021294.

[133] S. E. Thorsett. “Terrestrial implications of cosmological gamma-ray burst models”. In: *The Astrophysical Journal* 444 (1995), pp. L53–L55.

[134] S. Tilmes et al. “CESM1(WACCM) Stratospheric Aerosol Geoengineering Large Ensemble Project”. In: *Bulletin of the American Meteorological Society* 99.11 (2018), pp. 2361–2371. DOI: 10.1175/BAMS-D-17-0267.1.

[135] D. G. Vincent. “Mean meridional circulations in the Northern Hemisphere lower stratosphere during 1964 and 1965”. In: *Quarterly Journal of the Royal Meteorological Society* 94.401 (1968), pp. 333–349. DOI: https://doi.org/10.1002/qj.49709440109.

[136] C. M. Volk et al. “On the evaluation of source gas lifetimes from stratospheric observations”. In: *J. Geophys. Res.* 102 (1997), pp. 25543–25564.

[137] X. Wang and A. E. Dessler. “The response of stratospheric water vapor to climate change driven by different forcing agents”. In: *Atmospheric Chemistry and Physics* 20.21 (2020), pp. 13267–13282. DOI: 10.5194/acp-20-13267-2020.

[138] X. Wang, Y. Wu, et al. “The Simulation of Stratospheric Water Vapor Over the Asian Summer Monsoon in CESM1(WACCM) Models”. In: *Journal of Geophysical Research: Atmospheres* 123.20 (2018), pp. 11, 377–11, 391. DOI: https://doi.org/10.1029/2018JD028971.

[139] Y. Wang and Y. Huang. “Stratospheric radiative feedback limited by the tropospheric influence in global warming”. In: *Climate Dynamics* 55 (Nov. 2020). DOI: 10.1007/s00382-020-05390-4.

[140] D. Waugh and T. Hall. “AGE OF STRATOSPHERIC AIR: THEORY, OBSERVATIONS, AND MODELS”. In: *Reviews of Geophysics* 40.4 (2002), pp. 1–27. DOI: https://doi.org/10.1029/2000RG000101.

[141] J. C. Witte et al. “First reprocessing of Southern Hemisphere ADditional OZonesondes (SHADOZ) profile records (1998–2015): 1. Methodology and evaluation”. In: *Journal of Geophysical Research: Atmospheres* 122.12 (2017), pp. 6611–6636. DOI: 10.1002/2016JD026403.

[142] J. S. Wright and S. Fueglistaler. “Large differences in reanalyses of diabatic heating in the tropical upper troposphere and lower stratosphere”. In: *Atmospheric Chemistry and Physics* 13.18 (2013), pp. 9565–9576. DOI: 10.5194/acp-13-9565-2013.

[143] Y. Xia, Y. Huang, and Y. Hu. “Robust Acceleration of Stratospheric Moistening and Its Radiative Feedback Under Greenhouse Warming”. In: *Journal of Geophysical Research: Atmospheres* 125.19 (2020), e2020JD033090. DOI: https://doi.org/10.1029/2020JD033090.

[144] K. Yoshino et al. “Improved absorption cross-sections of oxygen in the wavelength region 205–240 nm of the Herzberg continuum”. In: *Planetary and Space Science* 36.12 (1988), pp. 1469–1475. ISSN: 0032-0633. DOI: 10.1016/0032-0633(88)90012-8.

A. Photolysis of Diatomic Oxygen

The calculation of the photolysis rate J_2 (from Reaction 2.9) is given by

$$J_2(p) = \int \phi(\lambda) F_0(\lambda) \sigma(p, \lambda) T(p, \lambda) \, \mathrm{d}\lambda, \tag{A.1}$$

where λ is wavelength on the electromagnetic spectrum, p is pressure (used here as the vertical coordinate), F_0 is the top-of-atmosphere incoming actinic flux, σ is the pressure- and wavelength-dependent diatomic oxygen cross-section, and T is the pressure- and wavelength-dependent transmission function. The above calculation shows an indefinite integral, but in practice the wavelength range used in the calculation of J_2 is 175 to 242 nm. The reason for this is that the quantum yield $\phi(\lambda)$ is unity over this range, and zero outside of this range. At lower wavelengths, the photolysis of diatomic oxygen produces excited monoatomic oxygen, as in Reaction 2.10.

The definition of the "top-of-atmosphere" – used to set the values of F_0 – may vary depending on the application, but in any case F_0 is most often prescribed from some dataset of observations. The U.S. Navy's observational dataset (Coddington et al., 2019) provides an excellent source of this data. This dataset is also time-varying, accounting for changes in sun-to-earth distance and in solar activity variability.

Likewise, σ must be prescribed by some dataset, and again JPL document 15-11 provides an excellent collection of this data (Burkholder et al., 1993). The structure of σ motivates the division of the electromagnetic spectrum into the Schumann-Runge bands from 175 to 205 nm and the Herzberg continuum from 205 to 242 nm. Within the Schumann-Runge bands, σ varies greatly with wavelength and with temperature. This creates a substantial challenge for line-by-line calculations of photolysis related to this electromagnetic region because the high variability of σ with wavelength reguires a small $\mathrm{d}\lambda$, making the calculation computationally expensive. To reduce this challenge, a variety of parameterizations for oxygen photolysis in the Schumann-Runge bands have been developed, accounting for the strong variability in both wavelength and temperature. That of Minschwaner et al. (1992) is used in a wide variety of applications and is also well-documented and straightforward to apply. In the Herzberg continuum, σ is not as strongly variable with wavelength as in the Schumann-Runge bands. However, σ was found to be dependent on pressure in this electromagnetic region, but the work of Yoshino et al. (1988) provides a simple and effective parameterization of this. Both the parameterizations of Minschwaner et al. (1992) and Yoshino et al. (1988) are recommended by Burkholder et al. (1993).

The transmission function T is calculated by

$$T(z,\lambda) = \exp\left[-\theta \int_{p}^{0} \sigma(p',\lambda) n(p') \cos(\theta)\, \mathrm{d}p'\right], \tag{A.2}$$

where n is the number density of diatomic oxygen and θ is the solar zenith angle.